Surface Behaviour for Materials Processing

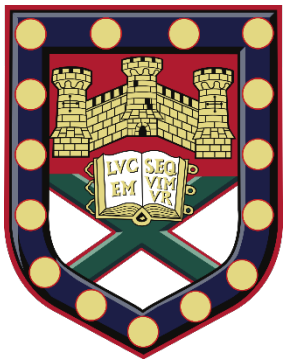

Submitted by Camilla Owens to the University of Exeter

as a thesis for the degree of

Doctor of Philosophy in Engineering

in July, 2019.

I certify that all material in this thesis which is not my own work has been identified and that any material that has previously been submitted and approved for the award of a degree by this or any other University has been acknowledged.

(Signature) ……

Abstract

The surface behaviour of minerals containing rare earth elements was investigated using zeta potential measurements. The rare earth fluorcarbonate mineral, parisite and a rare earth enriched phosphate mineral, apatite were measured under water and collector aqueous conditions, which are similar to those found under froth flotation. Firstly, the iso electric point of parisite was measured at pH 5.6 in water, this is within the range of reported IEP values of another rare earth fluorcarbonate mineral, bastnäsite. Bastnäsite currently sources over half of the world's rare earth elements and has well studied surface behaviour. The surface behaviour of parisite under collector and supernatant conditions was similar to bastnäsite, indicating that parisite could be processed using the same froth flotation regimes as bastnäsite. Secondly, the iso electric point of rare earth enriched apatite was measured at pH 3.8, which is consistent with the values of apatite non-rare earth enriched apatite in the literature. The surface behaviour of non-rare earth enriched apatite from the literature and the enriched apatite measured here is similar under common reagent conditions. This suggests apatite processing could be applied to rare earth enriched apatite deposits.

The first evidence of nanobubbles at the surface of the carbonate mineral, dolomite and rare earth fluorcarbonate mineral, synchysite were also reported. The nanobubbles were measured using non-contact atomic force microscopy, and produced using the gas oversaturation method of heating the liquid. Nanobubble density on dolomite was increased by collector conditions with 0.656 bubbles per μm^2, compared to 0.342 nanobubbles per μm^2 under water conditions. Investigating the contact angle of the nanobubbles on dolomite indicated that the reagents effected the pinning of the nanobubbles and not their surface tension. Nanobubbles on the synchysite sample in collector conditions had an average contact angle of 24 degrees, in line with previous studies. The presence of nanobubbles on synchysite under collector conditions demonstrates that the surface is hydrophobic.

Finally, nanobubbles at the surface of patterned and unpatterned chemical vapour deposition monolayer graphene were investigated. High-speed atomic force microscopy was used to image nanobubbles produced using solvent exchange. Nanobubbles were found on patterned graphene, not on the underlying SiO_2 substrate. This links to the increased hydrophobicity of graphene compared to SiO_2. The patterning of the graphene reduced the nanobubbles' lateral size and increased the contact angle, consistent with previous results of nanobubbles on patterning. These are the first reported results of nanobubbles constrained by chemically patterned graphene.

Acknowledgements

Firstly I would like to thank my supervisor Professor Geoffrey Nash, who has been an incredible support during the course of the PhD. His guidance, leadership and positivity is never-ending and I deeply appreciate the time and effort he has gone to in supervising me. I could not have hoped for a better mentor.

I would also like to thank Professor Gino Hrkac for introducing me to Geoff and for guiding me during a challenging period of my PhD. Thanks to Dr Matthew Watson, who since my time as Bristol has been an incredible support and guide. I would also like to thank the other members of my research group Caroline Pouya, Ben Ash, Tim Poole, Cheng Shi, Prarthana Vadegadde Dakapppa, Jessica Brown, Hannah Barnard and Vicky Kyrimi.

I appreciate the research visit I was able to conduct in Colorado School of Mines and for Professor Corby Anderson for hosting me. I would also like to thank in Colorado; Professor Erik Spiller, Victoria Vaccarezza, Dr Hao Cui and Dylan Everly. I also appreciate the time I had at Helmholtz Institute of Resource Technology Freiberg and for Dr Martin Rudolph for hosting me. Thanks go to Edgar Schach, Nathalie Kupka, Bent Babel and Hoang Huu Duong for making my time in Freiberg enjoyable. Thanks also go to Dr Kathryn Hadler at Imperial College London for her support and mineral processing expertise. Thanks also go to staff who helped me at Camborne School of Mines, University of Exeter. More recently I would like to thank Professor Mike Allen and Chris Evans at Plymouth Marine Laboratory who have made my last research collaboration of my PhD so much fun.

Away from research, I would like to thank my parents for being so supportive of me during this time. I don’t think I would be where I am today without them and I certainly would not have finished the PhD without their words of reason and

encouragement. I would also like to thank my friends, Eleanor Grugeon, Clara Montgomery and Catherine Danielsen for their never ending support and their easy ability to get me away from research. I would also like to thank Jelly and Kingston Owens for always being there to enable me to have some much needed explorations in the countryside. I am also grateful to my friends, Marta Skrzypinska and Bryony McGarry for their support and the ability to escape to riding in Poland. Thanks to Sarah Bunney for being my constant breakfast companion at Exeter and for going through our PhD journey together. Thanks should also go to the University of Exeter Polo who have been so welcoming to me and enabled me to have a superb outlet for my energy.

I also would like to thank people who are not listed here but have helped me along the way.

Table of Contents

List of Figures

List of Tables

Abbreviations

AFM – Atomic force microscopy

CP-AFM- Colloidal probe atomic force microscopy

EDL- Electrical double layer

HREE – Heavy rare earth elements

HS- AFM- High-speed atomic force microscopy

IEP- Iso electric point

LREE- Light rare earth elements

NC-AFM – Non-contact atomic force microscopy

PZC- Point of zero charge

REE- Rare earth elements

Chapter 1
Introduction

1.1 Motivation

Rare earth elements (REE) are composed of the lanthanide series of elements, with the addition of scandium and yttrium [1, 2]. They are vital to modern life and are present in a number of green technologies key for a clean future, from solar panels to wind turbines [3, 4]. However, the sourcing of REE is challenging as many deposits contain highly complex mineralogy making extraction difficult [5, 6]. Froth flotation is the most common method of processing rare earth deposits with the surface behaviour linked to optimal extraction [7]. The rare earth fluorcarbonate mineral bastnäsite, is the source of over half the world's REE [8]. New sources of rare earth elements have been identified, such as the rare earth fluorcarbonates and the phosphate mineral, apatite [1, 5]. However, there is little published research on the surface behaviour of rare earth fluorcarbonates, apart from bastnäsite [9, 10]. The surface behaviour of apatite is well documented, however the effect of rare earth enrichment on the surface charge under common reagents in flotation, is still poorly understood [11, 12, 13, 14]. This lack of knowledge makes commercial exploitation of these deposits challenging as the number and expense of the processing steps are unknown.

The first motivation of this work is enhance the understanding of surface behaviour of rare earth minerals to facilitate future development of deposits. One of the main aims of this research is to determine the surface behaviour of rare earth fluorcarbonates and apatite enriched with rare earth elements, under common reagent conditions used in flotation.

One aspect of froth flotation that is little studied is the role nanobubbles play at the surface of minerals during flotation. A secondary motivation of this research is to build on the understanding of nanobubbles at the surface of minerals. The aim being to image nanobubbles at the surface of the rare earth fluorcarbonate

mineral synchysite and the carbonate mineral dolomite. Dolomite is a common carbonate mineral found in rare earth deposits with well described surface behaviour, enabling the comparison of macroscopic flotation studies and nanobubble populations. Synchysite is a rare earth fluorcarbonate mineral; understanding the surface would build on surface behaviour of rare earth fluorcarbonates.

Nanobubbles are tiny gaseous domains at the surface of materials in aqueous solutions. Nanobubbles have previously been used to determine a minerals hydrophobicity in relation to flotation [15, 16]. Nanobubbles were first imaged in 2000 using atomic force microscopy and are between 10 and 50nm in height and 50 and 800nm in lateral length, smaller than the diffraction limit of visual light for imaging [17, 18]. Nanobubbles are known to appear preferentially at the surface of hydrophobic materials, with a greater population density under more hydrophobic conditions [19]. Although of interest to flotation generally, few studies have investigated nanobubbles at the surface of minerals and none have linked population density with hydrophobicity related to chemical reagents [15, 16, 20]. The limited number of studies of nanobubbles on minerals make the application of nanobubbles to flotation research challenging.

Nanobubbles are known to have long lifetimes sometimes surviving for days at a time [18, 21]. This is counter to their expected lifetime of micro seconds according to the Laplace pressure equations [22]. Another unusual property of nanobubbles is that their gas side contact angle is much smaller than macroscopic studies of bubbles on the same surfaces [18, 23]. Recent work has shown that the long lifetime and small contact angle of nanobubbles is due to a combination of surface hydrophobicity, gas oversaturation within the liquid and pinning along the nanobubbles three phase contact line [24, 25]. Pinning of the nanobubbles is due to chemical and physical heterogeneities. Physically patterning the surface is known to constrain the nanobubbles size and contact angle [26, 27]. Although previous studies have focused on the geometries of dots, ribbons and nanopores, the pinning on nanobubbles, due to patterning, is still poorly understood. The progress of implementation of nanobubbles, in

industrial processes, is also limited due to lack of control of nanobubbles formation.

The third motivation of this research is to investigate the field of nanobubbles on patterned surfaces. With the final aim of determining the effect of patterning on nanobubble location and size and the links between patterning and pinning.

1.2 Overview

The results presented in this thesis are the first measurements of the surface behaviour of the rare earth fluorcarbonate mineral parisite. Zeta potential measurements suggest the surface behaviour of parisite under flotation reagents is similar to bastnäsite. The first measurement of the surface charge of the rare earth enriched mineral apatite, under collector reagents, was also shown. The enrichment of apatite by rare earth elements was shown to not significantly affect the surface behaviour under reagents. Nanobubbles were imaged for the first time at the surface of the minerals, dolomite and synchysite, using non-contact atomic force microscopy. The nanobubbles showed that the surface of the minerals was hydrophobic under reagent conditions. The nanobubble population density was linked to the presence of chemical reagents. The first experimental evidence of nanobubbles at the surface of patterned and unpatterned monolayer graphene was presented, using high-speed atomic force microscopy.

Chapter 2 introduces the background of the seventeen elements known as the rare earth metals (rare earth elements) and the minerals that are mined to extract them. The rare earth fluorcarbonates minerals, including bastnäsite, parisite and synchysite are described. Bastnäsite, is the most common commercially mined rare earth mineral, however there is limited research on the other rare earth fluorcarbonates which are possible sources for future sourcing of rare earth elements. The background of apatite, a phosphate mineral currently mined for fertilizer, which is also a possible source of rare earth elements is also described. The most common extraction method for rare earth

minerals is froth flotation and this is discussed in detail. Next, the links between zeta potential measurements and froth flotation are described. Finally, previous research into the surface behaviour of the rare earth fluorcarbonate minerals and rare earth enriched mineral apatite are reviewed.

Nanobubbles are introduced in chapter 3. The background of nanobubbles and theory of their long lifetimes is reviewed. In particular, the new theory of nanobubbles lifetime being a combination of their pinning, gas oversaturation within the liquid and surface hydrophobicity is explored. The methods of detecting nanobubbles is then described, with a focus on atomic force microscopy and high-speed atomic force microscopy. The use of the phase image is detailed as this enables the identification of nanobubbles at a material's surface. Different production methods for nanobubbles are then summarized, including gas oversaturation and solvent exchange. A description of applications for nanobubbles, including their applicability in understanding complex ore hydrophobicity for froth flotation, completes the chapter.

Chapter 4 contains a comprehensive list of the samples and experimental methodologies used. Sample acquisition, manufacturing and analysis is then overviewed. Analysis methods for the mineral samples include X-ray diffraction, X-ray fluorescence and mineral liberation analysis. The methods for zeta potential measurements for minerals, to understand froth flotation optimisation, are then discussed. The use of streaming potential on ground samples of minerals, under different aqueous conditions, and its limitations is described. The imaging technique of atomic force microscopy to detect nanobubbles is then reviewed. The many imaging modes of atomic force microscopy and the advantages of tapping mode atomic force microscopy for imaging nanobubbles are detailed. The invention and use of high-speed atomic force microscopy is then described. A summary of the samples used in this thesis, and the measurement techniques applied to them, concludes this chapter.

The results of the zeta potential measurements on rare earth minerals are explored in chapter 5. The zeta potential measurements of the rare earth fluorcarbonate mineral parisite under water, collector and supernatant conditions are shown. These parameters simulate common flotation reagents and flotation conditions. The iso electric point of parisite in water was measured at pH 5.6, the first measurement of its kind. The surface charge of parisite under these collector and supernatant conditions is similar to the fluorcarbonate mineral bastnäsite, indicating that rare earth fluorcarbonate minerals could be processed using similar reagent regimes. The zeta potential measurements of rare earth enriched apatite under water and collector reagent conditions are then shown. The surface behaviour of rare earth enriched apatite is similar to non-enriched apatite indicating rare earth enrichment does not significantly affect processing. Thereby showing that apatite research of flow sheets for flotation processing can be applied to rare earth enriched apatite deposits.

Chapter 6 describes the results of a study of nanobubbles at the surfaces of the rare earth fluorcarbonate mineral synchysite and the carbonate mineral dolomite. This continues the work of chapter 5 into the surface behaviour of rare earth fluorcarbonates under flotation. Nanobubbles have previously been linked to the hydrophobicity of a mineral under flotation conditions. Non-contact atomic force microscopy (NC-AFM) was used to image the topography of dolomite which showed the presence of nanobubbles under collector, depressant and water conditions. The nanobubbles were produced using gas oversaturation by heating the water to between 20^{o}C and 30^{o} C. Experimental measurements showed that the nanobubble density on dolomite was increased by collector conditions compared to water conditions. Analysis of the contact angle of the nanobubbles on dolomite indicates that the collector does not affect the surface tension but does affect the pinning. This was the first time nanobubbles have been imaged on dolomite, a common waste mineral in rare earth mineral flotation, and only the fifth study of nanobubbles at the surface of minerals. NC-AFM was additionally used to image nanobubbles of the rare earth fluorcarbonate mineral synchysite under collector reagent conditions. The contact angle of the nanobubbles agreed with previous studies of nanobubbles at the surface of minerals. The presence of nanobubbles at the surface of

synchysite demonstrated the hydrophobicity under the collector conditions. Relatively little research has been conducted on synchysite and few studies have investigated its surface behaviour.

Chapter 7 shows the results of an investigation of nanobubbles at the surface of patterned and unpatterned monolayer chemical vapour deposited graphene. This work continues the investigation of chapter 6 into the pinning of nanobubbles at the surface of materials. As monolayer graphene is only 0.34nm thick any physical patterning would be limited and the chemical differences at the surface should dominate the behaviour. The patterned sample was of graphene rings with an underlying layer SiO_2. The solvent exchange process was used to induce a high population of nanobubbles at the surface under water conditions. Nanobubbles were imaged using high-speed atomic force microscopy (HS-AFM) and identified using spherical cap fitting. The results showed that nanobubbles were only found at the surface of the graphene rings on the patterned sample, no nanobubbles were found on the underlying layer of SiO_2. The lateral size of the nanobubbles was constrained by the rings, with a maximum lateral length of 400nm on the patterned graphene surface. This is only the second experimental demonstration of nanobubbles being imaged by high-speed atomic force microscopy and the first demonstration of nanobubbles constrained on a patterned 2D material. Future work is needed to further investigate the containment of nanobubbles at the surface of patterned graphene.

A summary of the results of this thesis are discussed in chapter 8, along with a number of suggestions for future work.

1.3 Contributions to publications

The results pertaining to the mineral parisite in chapter 2 and chapter 5 of this thesis have been published as Owens C L, Nash G R, Hadler K, Fitzpatrick R S, Anderson C and Wall F, “Zeta potentials of the rare earth element fluorcarbonate minerals focusing on bastnäsite and parisite” in Advances in Colloid and Interface Science. C Owens was responsible for zeta potential measurements, XRF measurements, data analysis and interpretation, and manuscript composition. G R Nash was the supervisory author and involved in manuscript formation, composition and edits. R S Fitzpatrick and C Anderson contributed to the manuscript edits. K Hadler and F Wall were involved in concept formation and manuscript edits.

The apatite results in chapter 2 and chapter 5 of this thesis have been published as Owens C L, Nash G R, Hadler K, Fitzpatrick R S, Anderson C and Wall F, “Apatite enrichment by rare earth elements: A review of the effects of surface properties “in Advances in Colloid and Interface Science. C Owens was responsible for zeta potential measurements, XRF measurements, data analysis and manuscript composition. G R Nash was the supervisory author and involved in manuscript composition and edits. C Anderson, K Hadler, R Fitzpatrick and F Wall contributed to the manuscript edits.

Chapter 6 of this thesis has been published as Owens C L, Schach E, Rudolph M and Nash G R, “Surface nanobubbles on the carbonate mineral dolomite” in RSC Advances (see appendix for full article). C Owens was responsible for non-contact atomic force microscopy (NC-AFM) measurements, data analysis and manuscript writing and composition. E Schach was responsible for NC-AFM measurements and manuscript edits. M Rudolph was involved in concept formation and manuscript edits. G R Nash was the supervisory author and involved in manuscript composition and concept formation.

Chapter 6 of this thesis has been published as Owens C L, Schach E, Heinig T, Rudolph M and Nash G R, “Surface nanobubbles on the rare earth fluorcarbonate mineral synchysite” in the Journal of Colloid and Interface Science. C Owens was responsible for non-contact atomic force microscopy (NC-AFM) measurements, data analysis and manuscript writing and composition. E Schach was responsible for NC AFM measurement. T Heinig conducted the MLA analysis of the rare earth ore sample and M Rudolph was involved in concept formation and manuscript edits. G R Nash was the supervisory author and involved in manuscript composition and edits.

Chapter 7 of this thesis has been written up as Owens C L, Evans C T, Shi C, Allen M J, and Nash G R, “Surface nanobubbles on patterned graphene” and submitted to Langmuir on the 25/6/19. C Owens was responsible for high-speed atomic force microscopy (HS-AFM) measurements, data analysis and manuscript composition. C T Evans was responsible for HS-AFM measurements. M Allen was involved in overseeing HS-AFM measurements and concept formation. C Shi conducted sample preparation and patterning. G R Nash was supervisory author and involved in concept creation and implementation, as well as manuscript edits.

Chapters 1, 3, 4 and 8 have been written by C Owens and have not been submitted previously as published articles.

Chapter 2
Role of zeta potential measurements in flotation

2.1 Overview

Rare earth elements (REE), such as lanthanum and neodymium, are critical to a wide range of technologies vital for modern day life such as mobile phones to wind turbines. The sourcing of rare earth elements however is problematic with supply currently dominated by China. New deposits are needed for the future of green technology. The main barrier to making new deposits economically viable is understanding the minerals' surface behaviour from which the REE are extracted. The zeta potential measurements of minerals enable flotation to be optimised. Identifying if the reagents have bonded chemically or physically to the surface of the mineral.

Bastnäsite, the most common rare earth element fluorcarbonate, supplies over 50% of the world's REE. Other rare earth fluorcarbonates such as parisite and synchysite are also becoming economically viable due to the growth in the market for rare earth elements. However, unlike bastnäsite, the surface behaviour of parisite and synchysite have previously not been reported.

Apatite, the mineral that sources the world's phosphate fertilizer, can become enriched with REE, and it is quickly becoming an attractive option for mining due to the ability to extract both phosphate and REE simultaneously. Although the surface behaviour of apatite is well understood, REE enrichment of apatite has not been explored in mineral processing.

This chapter will discuss: the background of flotation of rare earth elements (section 2.2); the surface behaviour of minerals (section 2.3); and the surface properties of two particular types of REE minerals, REE fluorcarbonates and REE enriched apatite. A summary of the chapter is given in section 2.5.

2.2 Froth flotation of rare earth minerals

2.2.1 REE minerals overview

Rare earth elements (REE), which consist of the lanthanide (=lanthanoid) series of elements plus scandium and yttrium as designated by the International Union of Pure and Applied Chemistry (IUPAC), are used in a wide range of products in the engineering, space and energy sectors [2, 28]. They are often subdivided into either light REE (LREE) or heavy REE (HREE) depending on their atomic number, with HREE often more valuable than LREE. Promethium (Pm) has no long-lived isotopes and does not exist to any appreciable extent in nature making the REE elements consist of 16 elements. REE are often utilized in magnets due to their high remanence and coercivity, which is a result of the relatively large number of unpaired electrons in their atomic structure [29]

REE are unusual due to their atomic radius decreasing with increasing atomic number. This is called the lanthanide contraction (figure 2.1), and due to the similar charge and atomic size, REE are often found together in minerals. Minerals are usually enriched with either LREE or HREE, with minerals such as monazite (LREE)PO_4 mainly enriched with LREE and xenotime (HREE)PO_4 enriched with HREE. The parenthesis element after a minerals' name indicates the dominant rare earth that the mineral is enriched in [1].

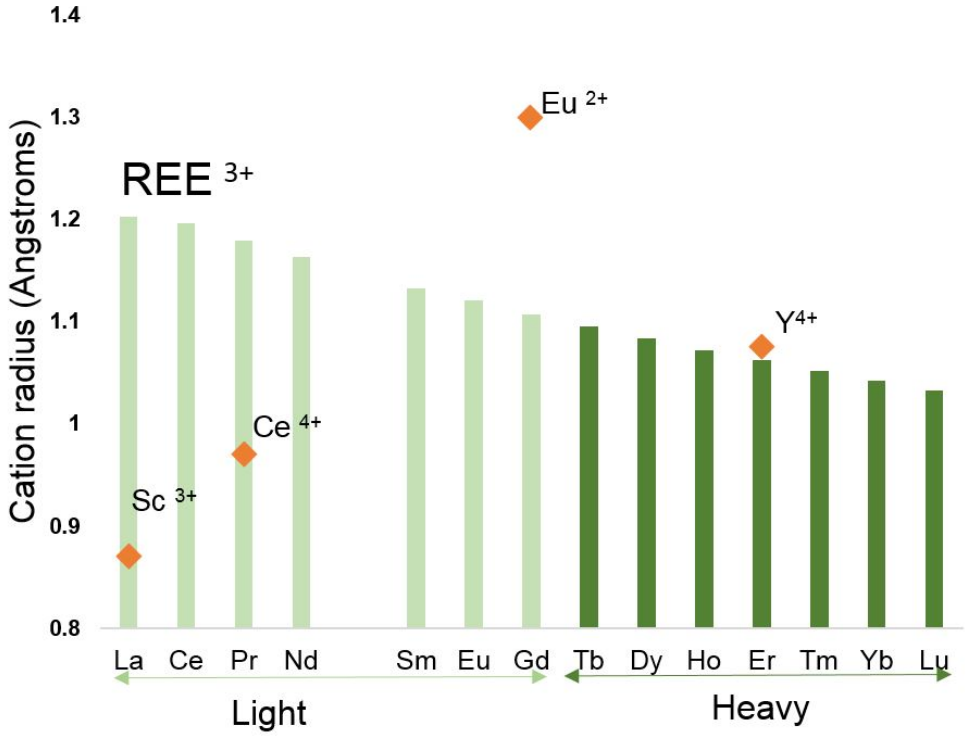

Figure 2.1 Cation radius of rare earth elements as a function of each element (adapted from Owens and Wall [30]).

Minerals can become enriched by rare earth elements by a wide range of processes, in some cases either by magmatic processes or later hydrothermal alteration [1]. Igneous deposits containing REE, such as the carbonate deposits of Songwe Hill, Malawi and Bayan Obo, China, are commonly polygenic in origin. Polygenic denotes a deposit having been altered many times by different processes causing the enrichment [31].

Rare earth elements are primarily sourced from minerals which host REE within their crystal lattice, unlike historically when monazite mineral sands sourced the world's REE. Rare earth elements bearing minerals are often contained within mineral (ore) deposits in small percentages (1-10%), requiring extensive extraction processes [28]. Extraction of REE bearing minerals is usually conducted by flotation, which submerges the mineral in water and uses the physiochemical properties of the different minerals to separate them. Flotation is optimized by adding chemical reagents, called collectors and depressants, to either increase or decrease the minerals' hydrophobicity respectively [5]. The

surface behaviour of minerals in aqueous solution is further explored in section 2.3.

Rare earth elements are contained within over 200 minerals and ore deposits located over seven continents, however concentrations are often too low to be economic [3]. Common commercially exploited rare earth minerals include the phosphate minerals, xenotime and monazite, and the rare earth fluorcarbonate mineral bastnäsite.

2.2.2 REE fluorcarbonates

REE fluorcarbonates are minerals which, consist of, but are not limited to, REE, F and CO_3 ions, most commonly in the general form REE (CO_3) F. There are over 34 REE fluorcarbonate minerals currently identified. Substitutions of elements such as thorium, sodium, barium and calcium into the lattice are rare, but in geological settings like Mont Saint Hilaire, exceptional minerals are formed such as horváthite ($NaY(CO_3)F_2$) and lukechangite ($Na_3Ce_2(CO_3)$ F) [32, 33]. REE are primarily sourced through the fluorcarbonate mineral bastnäsite-(Ce), sometimes spelled bastnaesite, which is the main ore mineral at the REE mine, Bayan Obo, China. Historically it was also mined in the Mountain Pass deposit, California, USA. Bastnäsite-(Ce) is also the most common mineral within the REE fluorcarbonate set of minerals and a member of the bastnäsite group which contains seven minerals (bastnäsite–(Ce), bastnäsite–(La), bastnäsite–(Nd), bastnäsite-(Y), hydroxylbastnäsite-(Nd), hydroxylbastnäsite-(Ce) and thorbastnäsite). Others minerals that are often linked to bastnäsite are parisite, synchysite and röntgenite (Table 2.1). First discovered in the Bastnäs mine in Sweden, after which it was named, bastnäsite has since been found in localities ranging from Pikes Peak Colorado to the moon [34, 35, 36]. In comparison, röntgenite was discovered in 1953 by Donnay and is very rare [37].

The nomenclature of rare earth fluorcarbonates requires that the dominant REE when specific to denoting a species is within parenthesis [38]. Table 2.1 shows the bastnäsite group of minerals plus parisite, röntgenite and synchysite.

Mineral	Example of locations	Chemical Formula	Theoretical or measured chemical composition in oxides	Crystal System
Bastnäsite-(Ce)	Bayan Obo, China Mountain Pass, USA Fen, Norway	$Ce(CO_3)F$	Ce =63%, C=5%, O=21.9%, F=8.67%	Hexagonal
Bastnäsite-(La)	Pike Peaks, Colorado, USA	$La(CO_3)F$	La= 63%, C=5%, O=22%, F=8.72%	-
Bastnäsite-(Nd)	Clara Mine, Germany Stetind pegmatite, Norway	$Nd(CO_3)F$	Nd =26%, La =18%, Ce=18%, F=9%, (CO_2 was not measured due to paucity of mineral).	Hexagonal
Bastnäsite-(Y)	Bayan Obo, China Nissi Bauxite Laterite Deposit, Greece	$Y(CO_3)F$	Y=52%, C=7.15%, O=28%, F=11%	-
Thorbastnäsite	Yaja granite, China Eastern Siberia, Russia	$ThCa(CO_3)_2F_2$ $3H_2O$	Ce=6.88%, C=4.72%, Ca=5.9%, Th=45.57%, H=1.19%, F=7.46%	Hexagonal
Hydroxylbastnäsite-(Ce)	Kami-houri, Miyazaki Prefecture, Japan Trimouns, France	$Ce\ (CO_3)(\ OH)$	Ce=64%, O=29%, C=5.53%, H=0.46%	Hexagonal

Hydroxylbastnäsite-(Nd)	Montenegro	Nd (CO_3) (OH)	Nd=65%, O=28%, C=5.43%, H=0.46%	Hexagonal
Parisite-(Ce)	Muzo, Bayaca, Columbia	$CaCe_2(CO_3)_3F_2$	Ce=28%, La=23%, C=6%, O=26% F=7%, Ca=7%	Monoclinic
Parisite-(La)	Mula Mine, Bahia, Brazil	$CaLa_2(CO_3)_3F_2$		Monoclinic
***Parisite-(Nd)**	Bayan Obo,China found in 1986	$CaNd_2(CO_3)_3F_2$	Nd=23%, La=20%, Ce=10%, C=6%, O=25%.,F=6%, C=6%	-
Röntgenite-(Ce)	Narssârssuk, Greenland (Denmark) Muso, Columbia	Ca_2Ce_3 $(CO_3)_5F_3$	Ce=37%. La=12%. C=7%.O=28%. F=6%. Ca=9%.	Hexagonal
Synchysite-(Ce)	Songwe Hill, Malawi Springer Lavergne, Canada	$CaCe(CO_3)_2F$	Ce=43%. C=8%. O=30%. F=6%. Ca=13%	Monoclinic
Synchysite-(Y)	Kutessay, Kyrgyzstan	$CaY(CO_3)_2F$	Y=33%. C=9%. O=36%. F=7%. Ca=14%.	Monoclinic
Synchysite-(Nd)	Triolet Glacier, Italy Grebnik deposit, Kosovo	$CaNd(CO_3)_2F$	Nd=44%. C=7%. O=30%. F=6%. Ca=12%.	No XRD data

*Table 2.1 Table of selected REE fluorcarbonates, chemical composition and examples of localities. Location lists the deposit name, country as stated by the literature, which may not cover modern borders. Chemical formulae are taken from International Mineral Association (IMA) Commission on New Minerals, Nomenclature and Classification (CNMNC). *Parisite-(Nd) not officially recognised by IMA CNMNC list as of July 2017. This table and full set of references can be found in the appendix, table A.3.*

REE fluorcarbonates can be differentiated by X-ray diffraction (XRD) which highlights differences in the crystal lattice and calcium content. Bastnäsite is calcium depleted, whereas synchysite contains over 16% calcium. Parisite and röntgenite form middle members of the series with 11% and 13% Ca content respectively.

Röntgenite and parisite are formed of layers along the c crystalline axis, the composition of which can be subdivided into bastnäsite (B) and synchysite (S) layers [37, 39, 40]. For a detailed insight into the structural and atomic arrangement of these minerals, see Ni *et al*. [41]. A summary of the composition is shown in figure 2.2.

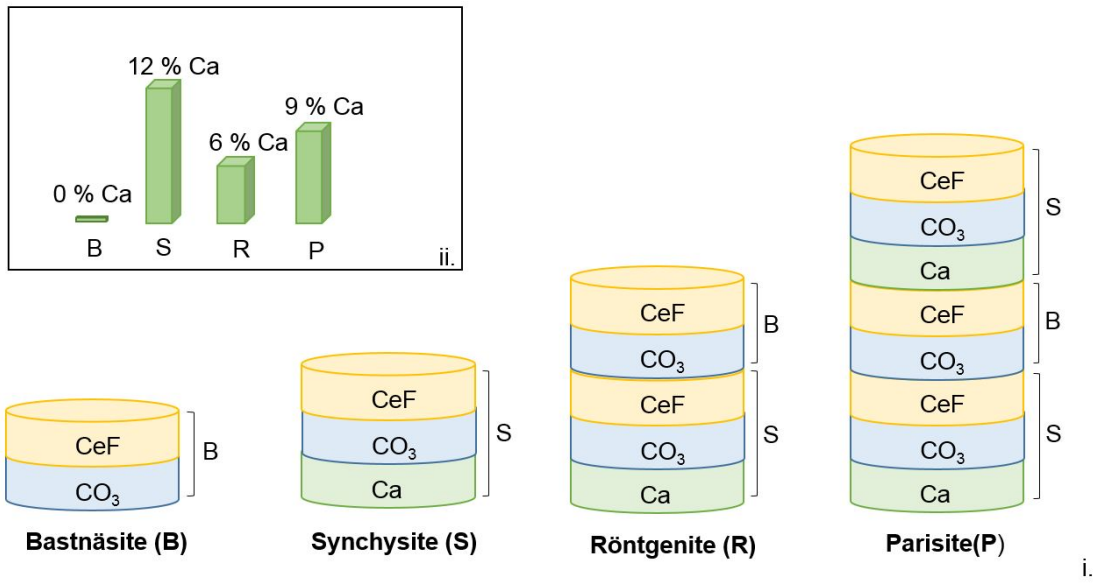

Figure 2.2. i. Schematic of REE fluorcarbonate minerals showing the stacking along the c-axis of the crystal. Röntgenite and parisite are made up of stacked layers of bastnäsite and synchysite (after Donnnay and Donnay [37] Van Landuyt and Amelincx [39] ;Manfredi et al. [40]).ii. Calcium content of bastnäsite, synchysite, röntgenite and parisite minerals adapted from Al Ali [9].

REE fluorcarbonate minerals often exhibit irregularities in crystal structure such as syntaxial intergrowth and stacking faults [36, 42]. This leads to irregularities

in their chemical structure, which can cause challenges in isolating individual species using techniques such as XRF (X-ray fluorescence) and XRD. Al Ali [9] described a mineral altering from parisite to synchysite along its length using an electron microprobe. Syntaxial intergrowth can be seen in synchysite at sites such as Songwe Hill, Malawi. Although syntaxial intergrowth is seen at Songwe Hill, the samples used in chapter 6 do not indicate syntaxial intergrowth.

2.2.3 Apatite

Phosphate is important to all life on earth, and the mineral apatite is the most abundant form of phosphate in the natural world [11]. Apatite is used as a source of phosphate fertilizer but natural forms of apatite make up human bones and synthetic apatite can be used as a bone replacement. Apatite is also known to host REE and is a possible source for future expansion in the REE market [1]. According to the International Mineralogical Association Commission on New Minerals, Nomenclature and Classification (IMA- CNMNC), there are three minerals of the apatite group, chlorapatite, fluorapatite and hydroxylapatite, named after the substitution of chlorine, fluorine and hydrogen/oxygen into the crystal lattice respectively (table 2.2)

Apatite	Chemical Formula	Theoretical Chemical composition	Deposits	Reference
Hydroxylapatite	$Ca_5(PO_4)_3OH$	Ca 39%, P 18%, O 41%, H 0.02%.	Jocao pegmatite, Minas Gerais, Brazil	Baijot *et al.,* [43]
Chlorapatite	$Ca_5(PO_4)_3Cl$	Ca 38%, P 17%, O 37%, Cl 6.8%	Breves deposit, Carajas, Brazil	Tallaricao *et al.,* [44]
Fluorapatite	$Ca_{10}(PO_4)_6F_2$	Ca 39%, P 18.4%, O 38%, F 3.7%	Adirondack Mountains, NY, USA	Lupulescu *et al.,* [45]

Table 2.2 Fluorapatite, chlorapatite and hydroxylapatite information and localities, taken from IMA-CNMNC Master List July 2017.

Apatite can substitute up to half the elements within the periodic table into its structure, and as such can become enriched with a number of different elements during either formation or a later hydrothermal alteration [11, 46]. Enrichment and alterations reflect early environments, from geological processes to early sea temperatures and paleo environments [47]. Sometimes the enrichment of a particular element makes the apatite of interest for that enrichment alone, for example in Songwe Hill, Malawi, apatite enriched with REE is under development as a REE mine [9].

The ability to mine for both phosphate and REE enables a more cost efficient mining practice. There are two processes of REE enrichment within apatite, the first is the substitution of REE^{3+} and Na^{+} for Ca^{2+} within the apatite, the second is P^{5+} substituted with REE^{3+} and Si^{4+} [48].The end member of the second substitution is britholite, a mineral heavily enriched in REE [49]. Table 2.3 lists a selection of deposits of REE bearing apatite currently identified in literature (as of 2018).

Deposit Name	Geological Setting	Country	Type of apatite	REE (% or ppm)
Phalaborwa	Carbonatite	South Africa		La 1245ppm
Songwe Hill	Carbonatite	Malawi	Fluorapatite	6200ppm Ce, 3400ppm Nd
Juquia		Brazil	-	1035ppm
Kovdor	Carbonatite	Kola,-Russia	-	1740ppm Nd, 3770 ppm Ce
Ermakorka (Transbaikalia)	Carbonatite	Russia	-	6610ppm Ce, 5130ppm La
Hillside deposit	Iron-oxide-copper-gold	Australia	Fluorapatite	1100ppm- >2%
Oka, Quebec	Carbonatite	Canada	Fluorapatite- hydroxyl-fluorapatite	6000-34000ppm REE
Hoidas Lake, Saskatchewan	Monzogranitic and tonalitic gneiss.	Canada	Fluorapatite	1.5-5% REE enrichment
Minami-Torishima Area, Japan	Deep sea mud	Japan	-	9300–32,000 ppm REE
Esfordi		Yazd Province, Iran	Fluorapatite, Britholite	

*Table 2.3 Full table in the appendix, table A4. A sample of REE enriched apatite deposits. This list includes a selection of REE enriched apatite deposits and is not representative of the entire list of deposits. *%REE denotes investigations into the mineralogy of deposits and does not represent the enrichment of all apatite within the deposit or its economic viability.*

Although Kola, Russia is one of the largest igneous apatite deposits, with apatite enriched with REE, there is very little published research relating to flotation of Kola ore [13]. Houot [13] showed Kola was floated with tall oil collectors and sodium silicate as a depressant. Processing of REE enriched apatite deposits has previously been explored by Soltani *et al.,* [50] and Harbi *et al*., [51] although there are no studies on the effect of REE enrichment on the surface behaviour of apatite compared to non-enriched apatite.

2.2.4 Froth flotation

REE minerals, in particular bastnäsite, are typically separated from the associated gangue minerals via froth flotation. REE deposits are sometimes processed additionally via other methods such as magnetic separation or gravity separation [5, 52]. As REE deposits can contain a number of REE minerals, such as monazite, xenotime, and bastnäsite, multiple extraction methods are often combined to enable optimum separation [5, 53]. However, ion adsorption clays, which are another source of REE, are instead directly processed via hydrometallurgy techniques such as leaching [5].

Leaching is often conducted using sulfuric acid, which breaks down the crystal structure of the mineral [54]. As leaching, using acids, produces large amounts of toxic by-product new methods such a bioleaching of minerals with fungal and bacterial species such as *Aspergillus niger* and *Penicillium sp.* have recently been proposed [55, 56]. Although bioleaching is an exciting area for further development current processing of REE minerals is still primarily conducted by froth flotation in China [5, 8].

Froth flotation makes use of the differences in the surface properties between desired minerals and gangue (waste minerals); these differences can be optimised by altering the surface chemistry through the addition of chemical reagents. A schematic diagram of flotation is shown in figure 2.3.

At the start of flotation an ore sample will be ground to a small size between 2 and 200 µm. The ore will then be deposited into flotation cells which contain a mixture of water and flotation reagents as well as an mechanical agitator, which produces bubbles and mixes the solution. Flotation reagents for REE processing include collectors such as potassium lauryl phosphate, hydroxamic acids and fatty acids, which render the REE mineral particles hydrophobic, and depressants such as sodium carbonate, sodium silicate and lignin sulfonate, which act to increase the hydrophilicity and/or dispersion of the gangue minerals [57, 58]. In conventional flotation, the collectors will cause the mineral of economic interest to attach to the bubble and rise to the top of the froth. In reverse flotation the waste (gangue) mineral will attach to the bubble and rise to the top. There is a clear link between surface behaviour in the presence of flotation regents and mineral recovery, first demonstrated by Fuerstenau in 1957 [59]. Since then a large volume of flotation research has been dedicated to surface and colloidal science [60, 61, 62].

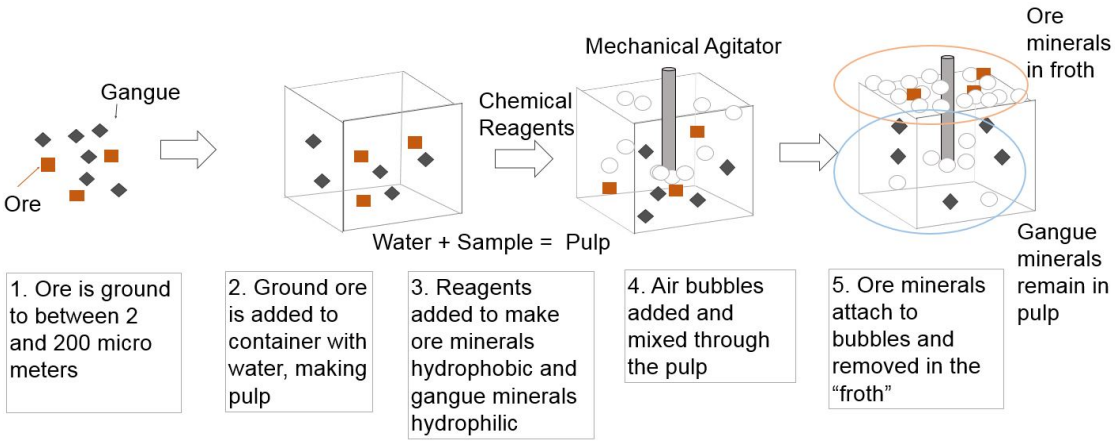

Figure 2.3 Schematic of froth flotation.

2.3 Surface behaviour

Surface behaviour describes a wide range of phenomena ranging from kinetic to electrochemistry, however as zeta potential measurements are the most applicable to flotation, the electrical double layer is described in detail. When a mineral is submerged in water the surface will acquire a charge due to a number of processes liberating ions including but not limited to preferential dissolution, hydration and surface group dissociation within the water. These free ions will form a counter layer or diffuse layer [63]. This charged area, the electrical double layer, can control the adsorption of collectors and reagents at the surface depending on the method of adsorption or attachment [64]. The mineral's surface properties determines which ions can bond with the electrical double layer [EDL], however all charged particles can form in the diffuse layer. The "potential determining ions" are the ions which affect the EDL and will either bond chemically with the surface, physisorb with the surface or link via Van der Waals force [65]. Physisorbed collectors are only effective when the mineral surface is oppositely charged to the collectors. Chemisorption, in comparison, can occur when the surface and the collector both carry the same charge, although if the Coulomb repulsion force is too large the collector will not be able to approach the surface to bond [66].

2.3.1 Electrical double layer

The electrical double layer (EDL) describes the charged area between the mineral surface and the charged and counter charged ions attracted to that surface [64]. Although more recently this has been described as the electrical interfacial layer, due to its complex nature, the most common description has been the EDL and this nomenclature is used in this section. The EDL is subdivided into the Inner Helmholtz layer, which marks the confines of closest approach of an ion to the mineral surface, the Outer Helmholtz layer which contains the attached ions, with the Stern plane subdividing the diffuse ions and the attached ions [63]. This is shown schematically in Figure 2.4. The most common method of characterising the electrical double layer is by measuring the zeta potential along the shear plane [64].

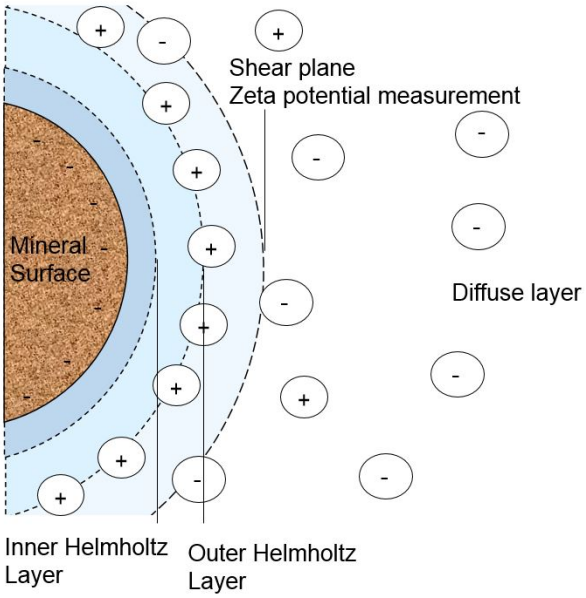

Figure 2.4 Electrical double layer at a mineral's surface.

2.3.2 Zeta potential measurement

Zeta potential is a measurement of the surface charge along the slip plane of the electrical double layer, and it can be probed using techniques such as electrophoresis, electro osmosis and streaming potential. In the majority of previous test work on rare earth minerals the zeta potential was determined using either electrophoresis or streaming potential, which are shown schematically in figure 2.5.

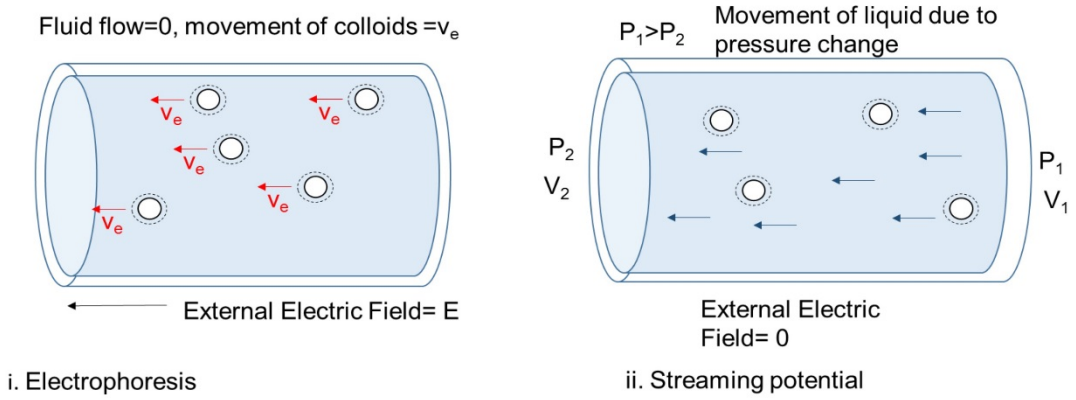

Figure 2.5 Schematic of electrophoresis and streaming potential.

In electrophoresis the velocity of the particle, the electrophoretic velocity, is converted into zeta potential by the Helmholtz-Smoluchowski equation (equation 2.1).

$$v_e = \frac{\varepsilon_{rs}\varepsilon_0\zeta}{\eta}E \qquad [2.1]$$

Where v_e is the electrophoretic velocity, ε_{rs} is the permittivity of the electrolyte solution, ε_o is the permittivity of a vacuum, η is the dynamic velocity of the liquid, E is the electric field and ζ is the zeta potential.

For a full review of techniques for measuring zeta potential see Delgado *et al.,* [64], Hunter [65], or Greenwood [67].

The most often quoted value for zeta potentials is the iso electric point (IEP), when the zeta potential equals zero as a function of pH. This is of particular value in waste water treatment, but is also utilised in many other fields such as mineral processing [68]. Zeta potentials are analysed over a wide range of pH's from alkaline to acidic to determine the IEP. Most mineral surfaces have a positive charge at a low pH with a negative charge at a high pH [69]. Although the IEP and a second measure of zeta potential, point of zero charge (PZC), are often quoted as being the same thing, the PZC refers to the surface of the mineral having zero charge, whereas the IEP occurs when the zeta potential is zero [60]. For certain mineral surfaces under specific conditions IEP may equal PZC. Zero zeta potential is when there is no net charge at the shear plane, when measured vie electrophoresis, this is when the particle remains stationary in an electric field (equation 2.4). In comparison, PZC is often acquired through potentiometric titration. When reagents such as anionic or cationic collectors are adsorbed onto the mineral surface, a change in the IEP under constant reagent dosage is a measure of adsorption free energy [70].

2.4 Surface properties

2.4.1 Fluorcarbonates

Bastnäsite is the only REE fluorcarbonate with published data for zeta potential measurements, with Smith *and* Steiner [1980] reporting the first values of zeta potential over thirty years ago. The main studies of the zeta potential of bastnäsite, which number twenty one at the time of writing, are presented in table 2.4, with a full list of studies given in the appendix. Many of these investigations link zeta potentials to micro-flotation experiments and the adsorption of various reagents at the surface [57].

In most studies multiple samples of bastnäsite are not investigated. However, Jordens *et al.,* [57] showed that sample origin had a lesser effect on the measured IEP than methodology, with electroacoustic methodology giving a much higher pH value for the same sample of bastnäsite at pH 8.1 than electrophoresis at pH 6.3. Although this work does not investigate this further, it may be of future interest. Both samples, from Jordens *et al*., [57] were of bastnäsite (Ce) so a hypothesis on the effect of the type of rare earths within the sample is not possible at this time.

.

Mineral	Deposit	Country	Purity	Size µm	PZC	IEP	Background Electrolyte	IEP in collector	Method	Year	Study
Bastnäsite	Mountain Pass	USA	some barite	<5	-	7	10^{-1} M KNO_3	na	-	2017	Azizi *et al.,* [71]
Bastnäsite (Ce)	Mountain Pass	USA	some barite	<5	-	7	10^{-1} M KNO_3	5.8		2016	Sarvaramini *et al.,* [72]
Bastnäsite	Zagi Mountain	Pakistan		-45		9	-		-	2016	Liu *et al.,* [73]
Bastnäsite	Mountain Pass	USA	some barite	<5	-	7	10^{-1} M KNO_3	4	-	2016	Azizi *et al.,* [74]
Bastnäsite (Ce)	-	-	Handpicked	<32	-	8.2	-	6.6, 5.2		2015	Anderson [75]
Bastnäsite	-	-	72.05REO %	-25	-	5.3	10^{-2} M KCl	-	-	2014	Fang *et al.,* [76]
Bastnäsite (Ce)	Mountain Pass	USA		d50=1.9	-	6.4	10^{-3}M KCl	8.9	Electro-phoresis	2014	Jordens *et al.*, [57]
Bastnäsite (Ce)	-	Madagascar		d50=2	-	8.1	10^{-3}M KCl	10.2	Electro-acoustic	2014	Jordens *et al.*, [57]
Bastnäsite (Ce)	-	Madagascar		d50=2	-	6.2	10^{-3}M KCl	7.6	Electro-phoresis	2014	Jordens *et al.,* [57]
Bastnasite	Haoniuping Mine	China	96.50% pure	37	-	7.8	-	-	Electro-phoresis	2000	Ren *et al.,* [77]

Bastnäsite (Ce)	Maoniuping Mine, Sichuan Province	China	98.10% pure	37	-	8	water	5.9	Electro-phoresis	1997	Ren *et al.,* [78]
Bastnäsite (Ce)	Pocos de Caldas, MG.	Brazil	-	37	-	4.9	10^{-3} KCl	4.2	Micro Electro-phoresis	1996	Pavez *et al.,* [79]
Bastnäsite	Mountain Pass	USA	Handpicked	1-10	-	5.3 (>30 minutes)	water		Electro-phoresis	1980	Smith *and* Steiner [80]
Bastnäsite	Mountain Pass	USA	Handpicked	1-10		6.8 (2 hours)	water		Electro-phoresis	1980	Smith *and* Steiner [80]
Bastnäsite	Mountain Pass	USA	Handpicked	1-10		7.2 (24 hours)	water		Electro-phoresis	1980	Smith *and* Steiner [80]

Table 2.4 Selection of published studies on the surface behaviour investigations into bastnäsite. Purity column uses the description of purity stated within the reference. Blanks within the column are due to the information not being stated within the referenced material. Gaps in the table correspond to where literature does not specify details. For results from Pradip (2015) the 'also' between values of electrolytes denotes that the study conducted two experiments with different electrolytes. For the full review of Bastnäsite zeta potentials please see the appendix, table A5.

The majority of studies have been conducted on bastnäsite originating from Mountain Pass, California. This is not entirely unexpected due to the long standing extraction of the deposit located there, which has previously been the prime source of REE from the 1980s [75]. The second most common locality for bastnäsite was Bayan Obo in China [81]. Bayan Obo currently supplies over 45% of the world REEs and it is likely that more research has been conducted on bastnäsite from Bayan Obo which has either not been published due to non-disclosure agreements, or not been translated into English. Although in some studies the type of bastnäsite used in zeta potential measurements is not stated, the majority state the species used was bastnäsite- (Ce).

The IEP of bastnäsite has been measured between pH 4.6 (Smith *and* Shonnard [82]) and pH 9.3 (Herrera- Urbina *et al*., [83]). There is no discernible effect from geological location, with samples of bastnäsite from Mountain Pass with IEP values ranging from pH 4.7 to pH 9.3. The Mountain Pass ore body has shown large variation between bastnäsite compositions, with areas showing different enrichment or REE within the bastnäsite, this variation may explain the large range in values of IEP from minerals from the same body. Synthetic bastnäsite has been found to have an IEP at pH 7.8 [84].

2.4.2 Apatite

The methodology of measuring zeta potentials of apatite varies between disciplines. For studies on calcium phosphate ceramics used in bone, the zeta potential is a measure of the bone structure formation and so this is conducted over a period of 400 hours. In comparison research into mineral processing is less time dependent and studies do not often reference over how long the value has been taken [85].Table 2.5 shows a selection of zeta potentials of natural apatite.

Mineral	Deposit/Type of Deposit/Country	Purity	IEP	Electrolyte	Reference
Fluorapatite	Van Waters and Rogers	-	8.7	water	Nduwa-Mushidi *et al.,* [85]
Fluorine-carbonate apatite.	Qingping Phosphate company, China	>95% pure	4.3	DI water	Cheng *et al.,* [86]
Collophane	Shanxi Province, China	92.5% pure	6.4	10^{-3} M KCl	Yu *et al.,* [87]
Collophane	Guizhou Province, China	94.51% pure	3	10^{-3} M/L KNO_3	Li *et al.,* [88]
Collophane	Dayukou phosphate mine, China	92.05% pure	6.5	10^{-3} M KCl	Yu *et al.,* [89]
Collophane	Zhongxiang, Hubei Province, China	handpicked (P_2O_5 38.66wt %)	<2	10^{-3} M/dm^3 NaCl	Yu *et al.,* [90]
Apatite	Wards natural science establishment	P_2O_5 46.06 wt %	4.2	10^{-3} M KCl	Zhou *et al.,* [91]
Fluorapatite	Bahia State, Brazil	-	4	Water	Nunes *et al.,* [92]
Francolite	Tulear Province, Fort Dauphin, Madagascar	CaO 49.1 wt% (Ce ,La 2402 1102ppm)	<3	10^{-1} M KCl	Filippova *et al*., [93]
Apatite	From Geological Museum of China	0.99	3	10^{-3} M NaCl	Yang *et al.,* [94]
Apatite	Tulear Province, Fort Dauphin,Madagascar	P_2O_5 33.68wt %, CaO 49.08%	1.5	10^{-1} M $NaNO_3$	Fillippov *et al*., [14]

Hydroxylapatitie	Acquired through Ward Natural Sciences	no impurities	4	1 M KCl	Kou *et al*., [95]
Fluorapatite	Paraibab,Brazil	very pure- analyzed via microprobe	1	0.01-0.05M NaCl	Chairat *et al*., [96]
Hydroxylapatite	Wangji Mine,China	handpicked	3.2	10^{-3} M KNO_3	Hu *et al*., [97]
Apatite	Chinese Mine,China	handpicked	3	10^{-3} M KNO_3	Hu *and* Xu [98]
Fluorapatite	synthetic		6.3		Perrone *et al.,* [99]
Francolite	Oulad Abdoun, trace REE 363.3ppm, Morocco	P_2O_5, 31.78wt %	4.8		Perrone *et al*., [99]
Chlorapatite and Hydro-fluro-apatite	Chilembwe deposit, Zambia	handpicked	6	DS water	Simukanga *and* Lombe [100]
Fluor-hydroxyl-apatite	Kaluwe deposit, Zambia	handpicked	3.8	DS water	Simukanga *and* Lombe [100]
Fluorapatite	Gregory, Bottley and Lloyd London/Canada	97% pure	4	KNO_3 (I=0.002)	Rao, Antti, *and* Forssberg [101]
Chlorapatite	Broken Hill, Lead-zinc/Australia		6.7	2x 10^{-3} M $NaClO_4$	Mishra [102]
Fluorapatite	Christmas Island, Indian Ocean.		3.5		Mishra [102]

Fluorapatite	Durango, Mexico	5.5	2x 10^{-3} M $NaClO_4$	Mishra [102]

Table 2.5 Fundamental Studies of zeta potential of natural apatite. Mineral name taken from paper description, may be out of date for IMA-CNMNC. Deposit type denotes the most information the source material provides, if no location is provided the acquisition company is listed. DI water is Deionized water DS water is distilled water. Micro-e denotes micro-electrophoresis, titr denotes titration.*

The IEP of natural apatite from table 2.5 varies from pH_{iep} of 1 to 8.7. This variation has previously been attributed to a number of factors, ranging from sample purity to methodology. Recent work has have found that the type of apatite is a main cause of differences and therefore this chapter will focus on this area.

Effect of type of apatite (Cl, F, H/O)

From the literature, the fluorapatite values ranged from 1 [86] to 8.7 [85]. This shows fluorapatite has a wide range of IEP values which may be due to variation within methodologies or purity. Mishra [103] and Simukanga *and* Lombe [100] investigated the surface behaviour of chlorapatite from Broken Hill, Australia and Chilembwe, Zambia respectively. The IEP values they obtained were pH 6 and pH 6.7 showing close similarity between the IEP of chlorapatite samples. Hydroxylapatite surface behaviour was analyzed in three papers Kou *et al.,* [95], and Hu *et al.* [97], specifying an IEP at pH 3.2 and pH 4 respectively. This showed a similar range of IEP to chlorapatite compared to fluorapatite which has a range of over 7.7 pH values. The location of the sample from Kou *et al.,* [95] is not specified however the sample from Hu *et al.,* [98] was from Wangji Mine, China. From this analysis the IEP value of chlorapatite (6, 6.7) was greater than the IEP of hydroxyapatite (3, 4). The zeta potentials of chlorapatite, hydroxylapatite, and fluorapatite are shown in figure 2.6

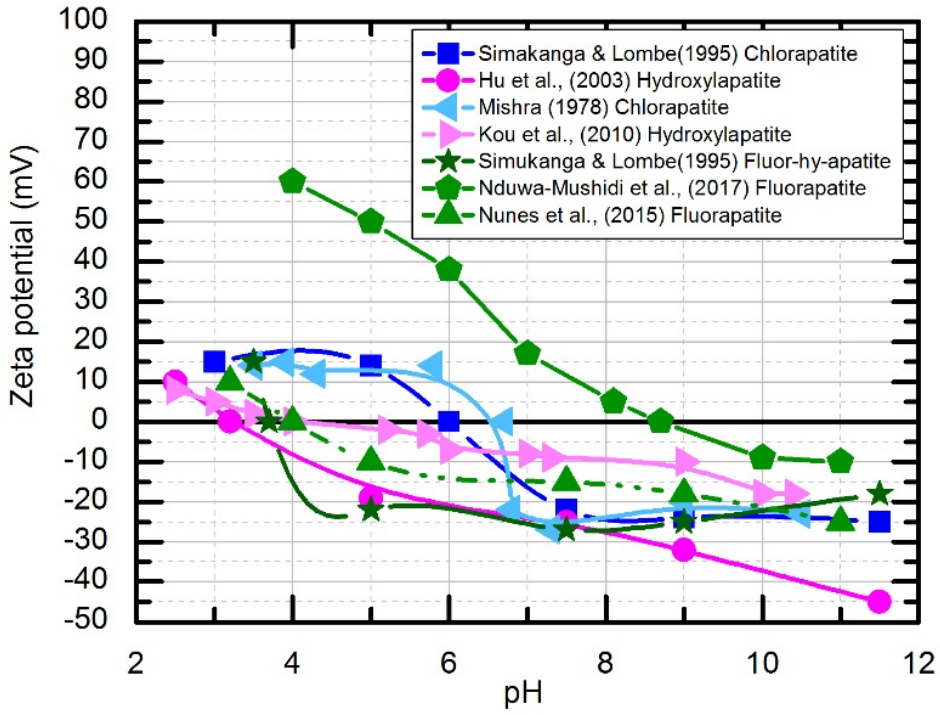

Figure 2.6 Zeta potentials of chlorapatite, fluorapatite, hydroxylapatite as a function of pH, from literature. Lines are plotted to guide the eye only.

From figure 2.6 chlorapatite has a more positive zeta potential than hydroxylapatite from the two studies plotted [100, 103]. The three studies of fluorapatite plotted showed a large variation within zeta potentials [85, 100], which could be due to contaminants within the sample.

REE enrichment of apatite

Although apatite can be enriched with REE [1], currently few deposits are mining for REE from apatite as a primary goal. Although table 2.3 identified a number of deposits with REE enriched apatite only Songwe Hill is currently being explored with REE as the main economic commodity.

From table 2.5 there are three zeta potential studies of natural apatite enriched with REE [14, 91, 93]. The apatite studied in Zhou *et al.,* [91] was enriched with 0.77% cerium. Filippova *et al*., [93] and Fillipov *et al.,* [14] both investigated

apatite with enrichment of 2402ppm of cerium and 1102ppm of lanthanum. All studies were enriched with LREE, this is not unexpected due to the higher percentage of LREE in the environment than HREE. Although these studies investigated apatite enriched with REE they did not draw any conclusions to the effect REE enrichment would have on processing of the apatite.

The effect of REE enrichment on the surface behaviour and processing of apatite is covered further in chapter 5.

2.5 Summary

This chapter discussed the flotation of rare earth minerals. Section 2.2 explains the background of rare earth minerals and the extraction of rare earth minerals from ore deposits using froth flotation. The surface behaviour of minerals is detailed in section 2.3, where the measurement of surface charge of minerals using zeta potentials is examined. Section 2.4 details the surface behaviour of REE fluorcarbonate minerals and REE enriched apatite previously investigated in the literature.

Chapter 3
Nanobubbles

3.1 Overview

Nanobubbles are tiny gaseous domains usually found at the surface of hydrophobic materials in water. Since nanobubbles were first imaged in 2000, they have been of growing interest due to their unusual properties. These properties include small contact angles at the liquid/gas/solid interface and extremely long lifetimes. In some cases nanobubbles have been shown to survive for days at a time. As well as being of interest to the fundamental science of colloids and surfaces, nanobubbles are thought to be applicable for a wide range of processes ranging from cancer treatment to decompression sickness [104, 105]. They have also been identified as a tool in improving understanding of hydrophobicity in mineral processing such as froth flotation [15]. Nanobubbles which form at the surface of graphene are also significant, as graphene is used in new biological sensing devices in aqueous environments, for example for detecting proteins [106, 107]. Although of interest to a wide range of industries the factors controlling nanobubbles formation, size and location is still poorly understood.

In this chapter, the discovery and background theory of nanobubbles is discussed in section 3.2. Section 3.3 describes the many methods of detecting nanobubbles, with emphasis on atomic force- and optical-microscopy. Section 3.4 covers the types of nanobubbles that have been investigated in previous studies, with details on the many methods of nanobubble production. Solvent exchange and gas oversaturation are the two methods used in chapter 7 and chapter 8, so they are discussed in more detail. The applications of nanobubbles are covered in section 3.5. Finally, section 3.6 summarizes the content of chapter 3.

3.2 Background and Theory

Nanobubbles are tiny gaseous domains within an aqueous solution which are between 10nm and 100nm high, and 50nm and 500nm in radius [18, 22]. Their existence was hypothesised in the 1950's, but were first imaged using atomic force microscopy (AFM) in 2000 [17, 108, 109]. For more detail on the history of nanobubbles in the intervening years see Alheshibri *et al.,* [110]. Nanobubbles are now widely accepted to be the cause of the attraction between two hydrophobic surfaces. They are unusual due to their long lifetimes and small contact angle between the gas/liquid/solid interface. This contact angle does not appear to be linked to macroscopic studies on the same surface, with the contact angle being much smaller in nanobubbles compared to macroscopic bubbles [19]. Figure 3.1 shows a schematic of a nanobubble at the surface of a material, with the contact angle, lateral length and height labelled.

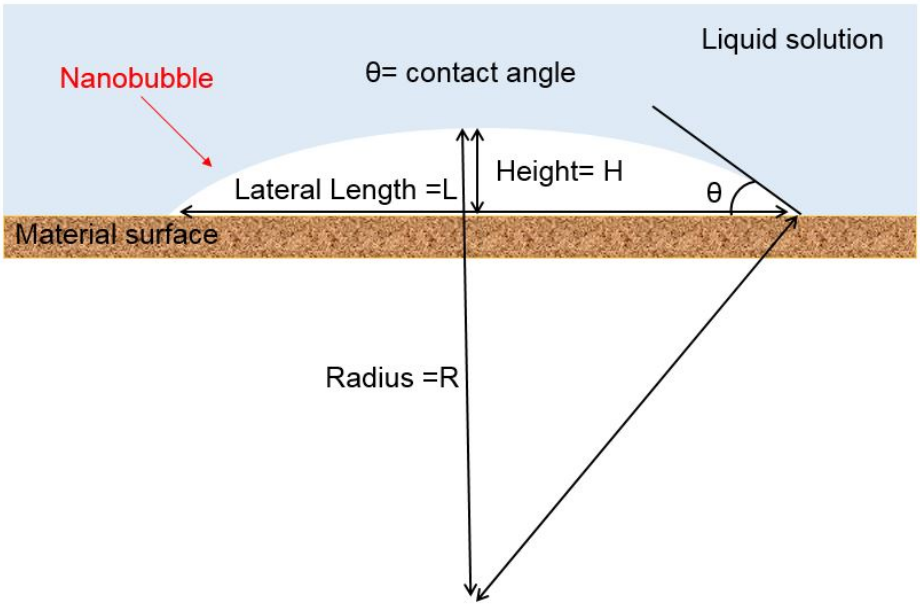

Figure 3.1 Schematic of nanobubble at the surface of a material.

It has been shown that nanobubbles exhibit a spherical cap shape, which can alter depending on background conditions [26, 111]. The contact angle in nanobubble research is almost always quoted as the gas side contact angle, shown in figure 3.1., however macroscopic sometimes quotes contact angle as both gas side or liquid side.

From the theory of Epstein *and* Plesset [109], nanobubbles should exist for a couple of micro seconds, where [21, 110]:

$$\tau_{lifetime} \sim \frac{R^2}{D} \qquad [3.1]$$

Where R is the radius of bubble, $\tau_{lifetime}$ is the bubble lifetime and D is the diffusion constant of the gas in the liquid.

However nanobubbles have been experimentally shown to exist for several days at a time [18]. Recent work has suggested the long lived nature of nanobubbles is due to pinning at the surface, gas oversaturation in the surrounding liquid, and the hydrophobicity of the material [24, 25, 112]. The equations which have been derived to govern nanobubble lifetime build from the seminal work of Epstein *and* Plesset [109], who investigated gas bubbles at the liquid gas interface under both oversaturated and under saturated gas solutions. They used a combination of the diffusion equation, the Laplace equation and Henry's law to give Equation 3.1, which can be written more fully as:

$$\tau_{lifetime} = \frac{{R_o}^2 \rho_g}{2D\ c_s \xi} \quad for\ large\ R_o\ and\ \xi < 0 \qquad [3.2]$$

$$\tau_{lifetime} = \frac{{R_o}^2 \rho_g}{3D c_s}\ for\ small\ R_o\ and\ any\ \xi \qquad [3.3]$$

Where $\tau_{lifetime}$ is the bubble lifetime, R_o is the bubble initial radius, ρ_g is the gas density, D is the diffusion constant, c_s is gas solubility, ξ is gas oversaturation. Gas oversaturation can be stated as:

$$\xi = \frac{c_\infty}{c_s} - 1 \qquad [3.4]$$

Where c_s is gas solubility and c_∞ is gas concentration far away from the bubble.

Lohse *and* Zhang [112] built on these equations with the calculation of the bubbles radius of curvature:

$$R = \frac{L}{2\sin(\theta)} \qquad [3.5]$$

Where *L* is the lateral length of the nanobubble, *R* is the radius of the bubble, and *θ* is the contact angle.

Substitution of equation 3.5 into 3.6 gives, the gas concentration *c(R,t)* at the bubble water interface:

$$c(R,t) = \frac{c_s}{P_o}\, p_g(t) = \frac{c_s}{P_o}\left(P_o + \frac{4\sigma \sin\theta}{L}\right) \qquad [3.6]$$

Lohse *and* Zhang [112], then combined in addition the Popov's "coffee stain evaporation problem", which describes the change in mass of the bubble over time:

$$\frac{dM}{dt} = -\frac{\pi}{2} LD \left[\left(P_o + \frac{4\sigma \sin(\theta)}{L}\right)\frac{c_s}{P_o} - c_\infty\right] f(\theta) \qquad [3.7]$$

Where *dM/dt* is the mass change of the bubble over time and where *f(θ)* can be stated as:

$$f(\theta) = \frac{\sin(\theta)}{1+\cos(\theta)} + 4\int_0^\infty \frac{1+\cosh(2\theta\xi)}{\sinh(2\pi\xi)} \tanh[(\pi-\theta)\xi]\, d\xi \qquad [3.8]$$

The mass of the bubble can be described as

$$M = \rho_g \frac{\pi}{8} L^3 \frac{cos^3\theta - 3cos\theta + 2}{3sin^3\theta} \qquad [3.9]$$

Equations 3.7 and 3.9 can be combined to produce

$$\frac{d\theta}{dt} = -\frac{4D}{L^2}\frac{c_s}{\rho_g}(1+cos(\theta))^2 f(\theta)\left[\frac{L_c}{L} sin\theta - \xi\right] \qquad [3.10]$$

Where L_c is the critical lateral extension, calculated as 2.84μm for air bubbles in water at room temperature. The physical meaning of critical lateral extension is the upper lateral extension threshold for stable surface nanobubbles to exist. Above 2.84 μm the nanobubble is expected to be unstable and diffusion of gas out of the nanobubble will not be compensated by gas oversaturation.

The solution of equation 3.10, of *dθ/dt=0,* then leads to an expression for the contact angle:

$$\sin\theta_e = \xi \frac{L}{L_c} \qquad [3.11]$$

Where gas oversaturation is *(ξ),* contact angle is *(θ*) and lateral length of the nanobubble is (*L*).

However, recent work by Tan *et al.,* [24], has shown that although the model developed by Lohse *and* Zhang [112], and the outcome equations 3.10 and 3.11 are good estimates for many states, it does not take into account why experimentally surface nanobubbles can survive in under saturated conditions [25]. To account for this Tan *et al.,* [24, 25], proposed that the oversaturation is not homogeneous within the system. Instead the saturated gas is primarily surrounding the surface of the material, making the oversaturation at the base of the bubble greater than at the top.

The spherical cap of the nanobubble was divided into an infinite number of slices, which is described as

$$S = 2\pi R \int_0^h dz = 2\pi R h \qquad [3.12]$$

Where *h* is the height of the bubble and *R* is the nanobubble radius. dM/dt (3.7) was then integrated over the rings and the result was normalized over 3.11. This then produced:

$$\frac{d\theta}{dt} = -\frac{D\, c_{sat}}{2\rho_g L^2 h}(1+cos\theta)^2 f(\theta) \int_o^h (\frac{2\gamma}{L\, P_o}\sin(\theta) - \xi(z))dz \qquad [3.13]$$

Where γ is surface tension, L is lateral length and c_{sat} is the gas saturation.

When oversaturation is constant equation 3.13 equates to equation 3.11, making the work by Lohse *and* Zhang [112] still applicable in specific conditions of set oversaturation. However in an experimental system oversaturation is known to be greater at the surface of the liquid, thus equating for nanobubbles which survive in under saturated conditions, as even if the bulk solution is under saturation, saturation may exist at the surface. As this is still a new solution without many experimental studies to confirm its validity, nanobubbles in this thesis were described using the model developed by Lohse *and* Zhang [112].

Three phase pinning on the contact line between the water, gas and solid interface has been shown to cause the long lived nature of nanobubbles [18, 22], and is known to be due to chemical and physical heterogeneities at the surface [18]. For physical pinning this is usually due to surface roughness or physical patterning at the surface. Previous research into patterning at the surface has shown nanobubbles are constrained by patterning such as dots, nanopores and ribbons [26, 27]. The effect of other geometries is not known and this area is explored further in chapter 8. Chemical heterogeneities can include changes to the structure of the surface from either chemical reagents such as collectors in mineral processing or changes in materials such as in patterning [113]. The effect of chemical heterogeneities is explored in more detail in chapter 7 and chapter 8. The value of pinning has recently been investigated by Tan *et al.,* [114] who calculated pinning between the values of 5mN/m and 15mN/m by dragging an AFM tip along the surface of the nanobubble on a glass slip.

3.3 Detecting nanobubbles

There are a number of methods for detecting nanobubbles including but not limited to; scanning transmission electron microscopy; rapid cryofixation; quartz crystal microbalances and atomic force microscopy [18, 115]. Atomic force microscopy (AFM) is the most common method of imaging nanobubbles, as it enables direct high resolution visualisation of the nanobubbles. Although optical

microscopy and total internal reflection fluorescence technique can also produce images of nanobubbles they are less common due to the prevalence of AFM [22, 116, 117]. As atomic force microscopy (and high-speed AFM) are the methods used to image nanobubbles in chapter 6 and chapter 7 these techniques are discussed in greater detail. For greater background on AFM and HS-AFM see chapter 4, sections 4.5 and 4.6.

3.3.1 Atomic Force Microscopy

Atomic force microscopy (AFM) was created in the 1980's as a method of imaging the surface of an object [118]. Since its inception AFM has rapidly expanded as a technique for measuring surfaces in a wide range of fields from DNA research to mineral processing [119, 120]. AFM uses a micromechanical tip (cantilever) interacts with the surface of an object, on the top of the tip is reflected a laser which is relayed to a detector. When the cantilever moves along the surface it will also move up and down or laterally as the surface topography changes, the reflected laser on top of the tip will move reflecting the topography allowing the development of an image of the surface [120, 121]. For a schematic diagram of an AFM measuring nanobubbles see figure 3.2

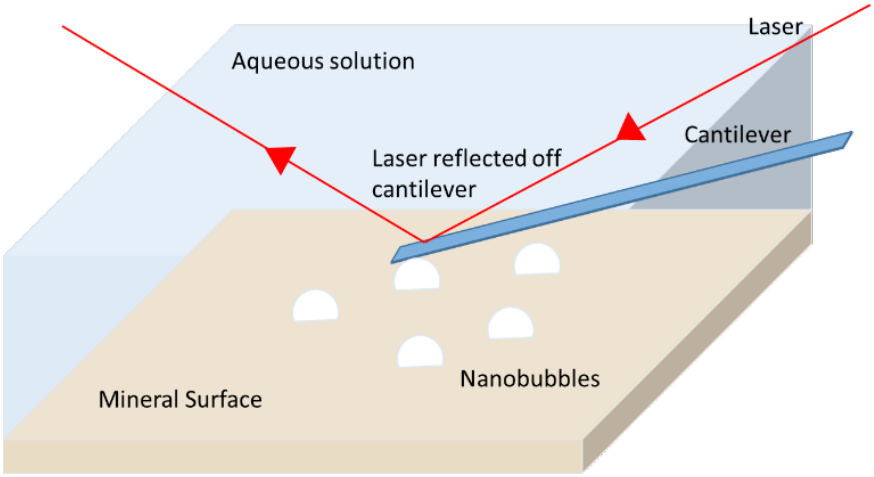

Figure 3.2 Schematic diagram of AFM measuring nanobubbles in aqueous solution. After Rudolph and Peuker [16].

AFM can be used in three main 'modes' depending on the force the cantilever exerts on the surface, the type of cantilever and the speed at which the

cantilever moves up and down. The three modes are contact mode, tapping mode and non-contact mode [122], these are detailed in chapter 4, section 4.5, figure 4.7. Most images of nanobubbles are produced under tapping mode AFM as this enables the production of a phase image, which is an indication of the interaction between the tip and the surface. There will be a difference in the phase image between a hard or soft surface determining if the tip is in contact with gas or mineral. In contact mode AFM the force of the cantilever on the surface is often too strong to successfully image nanobubbles and the nanobubbles are often removed from that area [108, 123]. Recently, high-speed atomic force microscopy, which images surfaces at higher speeds than conventional AFM has been used for the first time to image nanobubbles [124]. High-speed atomic force microscopy is covered in more detail in chapter 4, section 4.6. A challenge of imaging nanobubbles using atomic force microscopy is that the surface cantilever can alter the nanobubbles' shape making AFM invasive on nanobubble populations [125].

3.3.2 Other methods

Apart from AFM there are many other methods of detecting nanobubbles at the surface of materials. Optical interference-enhanced reflection microscopy was first used to image nanobubbles in 2012, using changes to the reflectivity due to the additional interfaces of the nanobubbles [116]. This method is limited on the situations with a planar suitably flat surface with many layers for reflections, and would not be appropriate for use on imaging nanobubbles on mineral surfaces. Total- internal reflection fluorescence microscopy can also be used to image nanobubbles at the surface with the additional of rhodamine 5G, which dyes the nanobubbles enabling the imaging [126]. As optical microscopy is not invasive and can image in real time, tracer particles can be used to track tracer particles and the Brownian motion of the fluid around a nanobubble or capture two nanobubbles coalescing [126, 127]. Applying optical microscopy is not limited to surface nanobubbles with bulk nanobubbles also being imaged to determine their sizes and shrinkage over time [128].

Methods which do not have such high spatial resolution include attenuated total reflection fourier transform infrared (ATR-FTIR), which relies on detecting the gas within the nanobubble [129]. ATR-FTIR relies on the nanobubbles gas to be active under infrared. Recent work using ATR-FTIR has investigated the permittivity of the gas water interface of the nanobubble using CO_2 movement [130]. Another interesting method is that of cyrofreezing, used by Switkes *and* Ruberti [131], who rapidly froze the water to image the nanobubbles contained at the surface of the material. A further low resolution method for imaging nanobubbles is quartz crystal microbalance, in which a quartz crystal sensor oscillates at a resonate frequency. This frequency is both shifted and dissipated due to adsorption caused by nanobubbles at the surface [132]. An advantage of this method is that the nanobubbles can be investigated over their formation period. For a comprehensive list of the more methods to identify nanobubbles, please see Lohse *and* Zhang [18].

Selecting a method for detecting nanobubbles depends on the characteristics of the nanobubbles that are being investigated. Commonly the lateral size and contact angle of the nanobubble is of interest, and therefore atomic force microscopy is by far the most prevalent method to extract these values. As AFM is so widely used the challenges and possible drawbacks of this method are well known, enabling the identification of nanobubbles to be effective [133]. For imaging the formation or coalescing of nanobubbles, techniques such as optical microscopy have the advantage as they are non-invasive and allow real time images. However, advances in the development of atomic force microscopy such as the invention of high-speed atomic force microscopy, enable it to acquire images faster facilitating the image of nanobubble formation [124].

3.4 Types of nanobubbles

3.4.1 Nanobubble formation

Nanobubbles are known to be present in many solutions and surfaces, however to investigate nanobubbles, they are often created in greater numbers than

occur naturally by a number of distinct processes [22]. These methods include but are not limited to gas oversaturation, solvent exchange and electrolysis. Gas oversaturation (also called gas supersaturation), uses heating of the liquid or cooling then heating, to induce oversaturation within the liquid. As the solubility of gas in warm water is lower than in cold water, heating the water induces oversaturation. For the formation of nanobubbles using gas supersaturation, Seddon *et al.,* [134] showed that nanobubbles form in water, when it's heated to between 25-45^{o}C with a gas concentration of between 100 and 110%. Above 45^{o} C and at 110% gas concentration micropancakes are formed. Zhang *et al.,* [135], Xue-Hua *et al.,* [123],and Berkelaar *et al.,* [136], found similar correlations between nanobubbles and temperate. Berkelaar *et al.,* [136] also determined nanobubbles grew independently of each other but had the largest average volume at 33^{o} C. This validates the temperature dependent nature of nanobubbles and therefore their formation using gas oversaturation. Gas oversaturation is used in chapter 6 to induce nanobubbles at the surface of the minerals dolomite and synchysite.

The most common method for inducing nanobubbles at material surfaces is solvent exchange, also called ethanol exchange [137]. Solvent exchange is the washing of the surface with water, then a solvent, then water again. As the solvent has a higher solubility than water, washing the surface with ethanol and then water, induces an oversaturation at the surface of the material [138]. Nanobubbles produced by solvent exchange are more numerous that nanobubbles produced by gas oversaturation [139]. A challenge of solvent exchange is controlling the many factors affecting the protocol including but not limited to liquid shear, flow boundaries and the saturation within the gas. Modelling using molecular dynamics simulations has been proposed as a way forward in this area [140]. Common solvents used in solvent exchange include methanol, propanol and ethanol, with propanol inducing the largest numbers of nanobubbles at a material surface [138]. Solvent exchange is used in chapter 7 to induce nanobubbles at the surface of graphene.

Nanobubbles can also be induced at a surface by electrolysis [141, 142]. As gas is generated at the surface of an electrode during electrochemical reactions, this leads to bubble formation [143]. Nanobubbles have been created at both the surface of highly orientated pyrolytic graphite (HOPG) and at platinum electrodes. Oxygen nanobubbles can be produced at the anode with hydrogen nanobubbles produced at the cathode in HOPG [143]. Studies of nanobubbles created by electrolysis often contain H+ gas as the nanobubbles are of interest for hydrogen gas production [143, 144]. These bubbles can also block catalytic sites and therefore understanding the formation of them is key to eradicating them in specific systems [145]. Nanobubbles formed by electrolysis sometimes exhibit much shorter lifetimes than expected of conventional nanobubbles, which can survive for days, and therefore can be grouped differently than nanobubbles produced by either gas oversaturation or solvent exchange [146]. Nanobubbles induced by solvent exchange and gas oversaturation have also been shown to contain air whereas depending on the parameter for electrolysis the bubble could contain a wide range of gases [22].

3.4.2 Nanobubbles, nanodroplets and micropancakes

Nanobubbles, or surface nanobubbles as described earlier in section 3.2, are usually identifiable by their shape of a spherical cap and their dimensions of 10-100nm in height and a width of 50-500nm, however there are other types of surface phenomena that are usually associated within the literature with nanobubbles. These include but are not limited to bulk nanobubbles, micropancakes and nanodroplets.

Bulk nanobubbles are spherical domains of gas in liquid, they have similar dimensions to surface nanobubbles but unlike surface nanobubbles are not present at the surface of a material but generally within the solution. Bulk nanobubbles usually have a diameter between 50nm and 700nm, with the size varying due to production method [147, 148]. Although they can survive for hours, which is longer than expected with Laplace pressure, they usually have shorter lifetimes than surface nanobubbles as they are not pinned, although

recent work has shown that in some cases bulk nanobubbles produced using acoustic cavitation could survive for months [149]. Bulk nanobubbles can be used for cleaning surfaces and mineral processing applications, this is covered in more detail in section 3.5. Hence forth in the text nanobubbles denotes surface nanobubbles unless specified otherwise.

Micropancakes are domains of gas at the surface of hydrophobic materials, they are a couple of nano metres thick and micro meters wide [22]. Although micropancakes have been shown to exist separately from nanobubbles, they have also been shown to occur simultaneously with nanobubbles. Micropancakes were only discovered in 2007 by Zhang *et al.* [150], they were produced using the solvent exchange and gas oversaturation techniques which induces nanobubble formation, and therefore are a direct offshoot of nanobubble research. Recent work on micropancakes indicates that they are formed from plastic contamination from syringes, it is unclear if earlier work on micropancakes denotes measured phenomena [151]. Micropancakes are not investigated in this work and none of the production methods in chapter 6 and chapter 7 induced micropancake formation.

Nanodroplets can be created by solvent exchange, this process can also described as the “ouzo effect” after the greek alcohol. They are tiny domains of solvent liquid present at the surface of materials in liquids, which appear as spherical caps. Nanodroplets can be filled with a range of liquids depending on the production method of the solvent exchange. They have similar dimensions to nanobubbles, with heights ranging from 10nm to 70nm [18]. They also exhibit a range to contact angles within a single nanodroplet population, mimicking the behaviour of nanobubbles [18]. For this reason it has been hypothesised that some nanodroplets have been incorrectly identified as nanobubbles in research [133]. Nanodroplets can be differentiated from nanobubbles by either a force curve response or changes in their shape in high force imaging atomic force microscopy [152, 153].

Nanobubbles have been imaged on a wide range of hydrophobic surfaces, ranging from HOPG to mineral surfaces [16, 23, 154]. The more hydrophobic the surface is the greater number of bubbles [26, 155]. Increasing the roughness also increases the stability of nanobubbles and therefore their pinning to the surface [155]. Nanobubbles have also been measured on hydrophilic surfaces, such as glass slips, demonstrating that the surface does not have to be hydrophobic for nanobubbles to form [114, 126]. A prerequisite for nanobubble formation appears to be that the surface is hydrophobic or that there is significant oversaturation, however the exact value for wettability or oversaturation for nanobubbles formation has yet to be calculated [24].

3.5 Applications

Nanobubbles are thought to play a role in a wide range of fields, including mineral processing, cancer treatment and energy storage. As chapter 6 investigates nanobubbles for use in mineral processing, this area is covered in depth. Similarly as chapter 7, examines nanobubbles on 2D materials, this topic is also covered in more detail.

Mineral processing

Mineral processing is the mechanism of extracting valuable minerals from a host rock (ore) and concentrating them until they are of a purity which is usable [156]. There are many methods of mineral processing, the most common being, froth flotation, gravity separation and magnetic separation. Froth flotation utilises minerals' physio-chemical surface properties to separate gangue (waste) minerals from ore (valuable) mineral, by attaching the ore minerals to bubbles within an aqueous solution [157]. Froth flotation is covered in more detail in chapter 2, section 2.2.4.

The properties of bubbles within flotation has long been recognised as a key parameter which affects the efficiency [158]. Since the imagining of nanobubbles in 2000, a large volume of research has been designated to their applicability to froth flotation [20, 159]. Research into nanobubbles relating to flotation is divided into investigating surface nanobubbles, using atomic force microscopy or bulk nanobubbles using flotation recovery information.

Bulk nanobubbles, produced using cavitation generation, have been studied as a way to improve flotation in a number of minerals, ranging from coal to galena [20, 160]. Historically in flotation literature nanobubbles have also been called picobubbles, although these may sometimes described a bubble that classically would be referred to as a microbubble (1μm radius) not a nanobubble [161]. Bulk nanobubbles studies usually focus on flotation, plotting the effect of recovery with and without nanobubbles [20]. Recent work by Rosa *and* Rubio [162] has shown that preconditioning an ore with nanobubbles before flotation can significantly increase the recovery of the ore mineral.

Previous studies of surface nanobubbles in mineral processing

Surface nanobubbles have been identified as both a tool for identifying the hydrophobicity of a mineral but also as being present in flotation [15]. As of 2019, there have been five previous studies of surface nanobubbles and the effects of mineral processing reagents. The minerals studied were varied from galena, a common lead sulphide, to eudialyte, a highly complex rare earth bearing mineral [16, 120, 163]. Three of the studies focused on force curves of ores of complex mineralogy [15, 16, 120], whereas one study investigated the dimensions of the nanobubbles [163].

Rudolph *and* Peuker [16] used colloidal probe- atomic force microscopy (CP-AFM) to measure hydrophobicity over a cross section of ore allowing the optimisation of flotation of complex mineralogy. This work linked nanobubble domains identified through force curves to sodium oleate concentration on a

mixed syenite ore from Sweden. Domains were found consistently on the eudialyte mineral when conditioned with sodium oleate collector. Typical separation distances of 39.9-64.4nm were found between the probe and the surface of eudialyte. In comparison separation distances were not found consistently over the gangue minerals of albite and aegerine. Eudialyte is a rare earth bearing zircon silicate mineral with a highly complex crystallography ($Na_{15}Ca_6(Fe^{2+},Mn^{2+})_3Zr_3[Si_{25}O_{73}](O,OH,H_2O)_3(OH,Cl)_2$). Due to its complex mineralogy there has historically been difficulty in processing eudialyte, with few samples of pure eudialyte making zeta potential measurements challenging. However large economically viable deposits in Greenland (Ilímaussaq) and Sweden (Norra Kärr) have the possibility for future extraction, making improving processing using flotation or magnetic separation a priority [164, 165, 166]. Using nanobubbles to map the minerals' hydrophobicity is therefore a vital step in improving their viability to extraction.

Rudolph *and* Peuker [120] built on early work by Rudolph *and* Peuker [16] by linking the results from the complex mineralogy at Norra Karr of colloidal probe atomic force microscopy (CP-AFM) measured hydrophobicity to micro-flotation, a more conventional method to measure hydrophobicity in a mineral. Micro flotation of magnetite showed a recovery of over 80% at pH values between pH 4 and pH 8, with 50% recovery at pH 10. This compared favourably to CP-AFM measurements, which showed nanobubbles between pH 6 and pH 9, and no nanobubbles at pH 10. This work was continued in Babel *and* Rudolph [15], which combined CP-AFM with contact angle measurements to determine hydrophobicity of a mixed chalcopyrite ore. Although nanobubbles were not explicitly measured, they were inferred from the study. Mikhlin *et al.,* [163] in comparison focused on surface nanobubbles on galena under different concentrations of collector potassium xanthate, showing differences in typical cross sections under different collector concentrations.

Hampton *et al.,* [138], is the only study that investigated the effect of collectors on surface nanobubbles and this was not connected to the hydrophobicity of minerals [15]. No previous studies have linked bubble density with

hydrophobicity at the surface, and this topic will be explored in greater depth in chapter 7.

Graphene and nanobubbles

Graphene is a 2D material composed of a single layer of carbon atoms. First isolated in 2004, it has been of wide interest, due to its highly unusual electrical and mechanical properties [167, 168]. Graphene holds particular promise for the development of novel devices from lab on a chip applications, to beam steering for infrared light to surface acoustic wave devices for meteorology [169, 170].

When discussing nanobubbles and graphene, *graphene nanobubbles* must be mentioned. Graphene nanobubbles are bubbles between layers of graphene, rather than surface nanobubbles which are located above a surface in the solid/liquid/gas interface. Graphene nanobubbles show very unusual properties, such as very high pressure, and have wide ranging applications for energy and gas storage [171, 172, 173]. Although graphene nanobubbles are usually studied independently of surface nanobubbles, some studies have looked at both, as electrolysis can produce both surface nanobubbles and graphene nanobubbles on highly ordered pyrolytic graphite (HOPG) [171].

Graphene is often required to be in contact with a water interface when it is being used for bioanalytical techniques [174]. The behaviour of graphene in water under different conditions is therefore important to enable these techniques to be effective [107]. The formation of nanobubbles can occur when using graphene as a biosensor, such as in a recent study of RNA at the surface of graphene [106]. Therefore this makes understanding of nanobubbles at the surface of graphene important to improving such techniques.

Other uses

Apart from mineral processing and microfluidics, a wide range of industries have also been identified as possible contenders for nanobubble use. These include but are not limited to medicine, food manufacturing and waste water cleaning. The use of nanobubbles in medical devices can be divided into a number of topic, from those focusing on imaging techniques to those focusing on drug deliveries [175, 176].

Nanobubbles due to their very small size and long lifetime, enable the transfer of small quantities of gas into the blood stream and around the body. The effective and efficient delivery of diagnostic and therapeutic agents is vital to the treatment of many diseases. Nanobubbles offer an exciting avenue to transport these drugs as many alternative delivery methods may results in the accidental release into healthy cells. Controlled release of drugs into a specific target zone can be conducted using plasmonic bubbles when exposed to a laser pulse [177]. Plasmonic nanobubbles are produced when plasmonic nanoparticules are excited using short laser pulses causing vapour to form around the nanoparticle, thus called a plasmonic nanobubble [175]. The use of nanobubbles has also been used with ultrasound, combined with nanobubbles and nanoparticles to both induce drug release and for imaging the area of interest [176, 178]. The use of plasmonic nanobubbles in cancer treatment is well explored, although the links between plasmonic nanobubbles and surface nanobubbles is removed, a greater understanding of surface nanobubbles is vital to widening the uses of nanobubbles in medicine [179].

Bubbles are used in a myriad of ways in food, from the rising of bread to the effective crystallization of ice cream [180]. Nanobubbles production for the use in food has recently been patented [181]. Nanobubbles of oxygen and air have previously been found to significantly improve the growth rate of both plants and mammals [182]. The use of bubbles for cleaning of contaminants is also of interest in studies into waste water treatment and algae processing [183].

This section does not cover the full uses of nanobubbles and focuses on areas linked to the work explored in the thesis, see Lohse *and* Zhang [18] for more comprehensive list.

3.6 Summary

In this chapter, the history and characteristics of nanobubbles are discussed and described in detail. Section 3.2 covers the background and theory of nanobubbles including the factors governing their long lifetime at the surface of materials. The formation of nanobubbles and their long lifetimes is controlled by chemical and physical heterogeneities at a materials' surface, localised gas oversaturation and surface hydrophobicity. Section 3.3 discusses the many methods of detecting nanobubbles including atomic force microscopy and optical microscopy. Atomic force microscopy is by far the most common method for detecting nanobubbles as it produces high resolution images. The different types of nanobubbles produced at the surface of materials are described in section 3.4. These include nanobubbles produced using solvent exchange, gas oversaturation and electrolysis. The uses and application of nanobubbles to various industries such as mineral processing and cancer treatment are overviewed in section 3.5.

Chapter 4
Methodology

4.1 Overview

In this thesis, the main areas investigated are surface behaviour measurements of rare earth minerals, and rare earth enriched minerals using zeta potentials (chapter 2 and 5) and nanobubbles on material surfaces using atomic force microscopy (chapter 3, 6 and 7). All these measurements were conducted in liquid conditions. This chapter outlines and explains the methodologies used to achieve these aims.

For surface behaviour to be interpreted the composition and purity of the mineral sample needs to be determined. Mineral sample purity is usually calculated using x-ray diffraction or x- ray fluorescence (section 4.3). For aqueous solutions containing dissolved species inductively coupled plasma mass spectrometry is used to determine the exact composition of the ions.

To measure nanobubbles on top of material surfaces, either mineral or two dimensional (2D) material, the surface must be accurately characterized. For mineral ore sections the exact mineral composition can be analysed using either mineral liberation analysis or QEMSCAN (section 4.3). This allows for the identification of the exact mineral on which the nanobubbles are located. For nanobubbles on patterned graphene, commercially available graphene was patterned at the University of Exeter, with optical microscopy used to check the effectiveness of the patterning.

One method of determining the surface behaviour of a mineral requires the use of a zeta potential instrument, which measures the surface charge of a mineral under different aqueous conditions. In this work, zeta potential measurements were conducted using a microtrac stabino streaming instrument from Colorado School of Mines (section 4.4).

Nanobubbles were imaged on the surface of materials using atomic force microscopy. Two types of atomic force microscopy were used, non-contact atomic force microscopy, covered in section 4.5, to measure nanobubbles on mineral samples and high-speed atomic force microscopy to measure nanobubbles on patterned graphene samples, covered in section 4.6.

4.2 Materials

The materials used can be divided into mineral samples (section 4.2.1), and patterned samples of two dimensional materials (section 4.2.2).

4.2.1 Mineral samples

The rare earth elements (REE) are important for modern technology and future economic development (chapter 2). The REE minerals which are investigated here are the rare earth fluorcarbonates and REE enriched apatite.

Minerals used in zeta potential measurements

Rare earth fluorcarbonates denote a wide range of minerals, the most common of which is bastnäsite [5]. However, to understand the behaviour of the rare earth fluorcarbonates under flotation using zeta potential measurements, less common rare earth fluorcarbonates were required. For zeta potential measurements a sample of at least 5g of pure mineral is usually required. Minerals such as röntgenite and synchysite often only appear in small sizes in the order of μm, within a complex matrix, making these measurements problematic [9]. However, parisite from Snow Bird Mine, Montana contains the large single crystals needed to conduct zeta potential measurements [184]. A parisite sample from Snow Bird Mine, Montana was acquired from Ikon Minerals for zeta potential measurements to compare to surface behaviour of bastnäsite.

REE enriched apatite is a possible source of REE for the future, however the surface behaviour of REE enriched apatite is not fully understood. There were

previously no studies comparing the processing using flotation of rare earth enriched apatite to non-REE enriched apatite. To discern the effect of REE enrichment on the surface behaviour, the zeta potentials of REE enriched apatite and non-enriched apatite would need to be compared. A sample of REE enriched apatite from Jacquiria, Brazil was acquired from Dr Sam Broom-Fendley to this end. This sample was from a deposit with well constrained mineralogy that has previously been shown to be heavily REE enriched. This sample was composed of pure mineral grains, which enabled effective zeta potential measurements. Mineral sample preparations are covered in more detail in chapter 5, sections 5.2.2 and 5.4.2.

Mineral samples used in AFM measurements

As REE fluorcarbonate minerals such as synchysite and röntgenite occur in too small a samples to be measured using zeta potential measurements, an ore sample containing synchysite was analysed using atomic force microscopy to determine the hydrophobicity using nanobubbles. The ore sample was from Songwe Hill, Malawi and was acquired from Mkango Resources Ltd. The ore minerals at Songwe Hill are synchysite and a heavy rare earth enriched apatite. For more details on the Songwe Hill, see Broom-Fendley *et al.,* [185] , and Al-Ali [9].

Dolomite is a carbonate mineral which is a common gangue (waste) mineral in many rare earth element deposits [5]. Understanding the surface behaviour of nanobubbles on its surface could greatly improve flotation as nanobubbles have previously been linked to a surface's hydrophobicity [15]. A sample of dolomite was acquired from Edgar Schach at Helmholtz Institute Freiberg for Resource Technology. The dolomite was set within an epoxy resin and then polished until smooth for NC-AFM measurements.

4.2.2 Patterned graphene

The 2D material, graphene, was patterned to image nanobubbles on a very flat patterned surface, thereby determining the effect of surface patterning and therefore chemical heterogeneities on nanobubbles.

Graphene

Graphene is a one atom thickness allotrope of carbon [186]. First produced in 2004, it is the strongest material known and has since become a highly prominent in materials engineering and physics due to both its electrical and physical properties [167, 168]. Graphene can be used in a wide range of industries from SAW devices in electrical applications using acoustic waves to its incorporation in polymer matrixes in composite materials [187, 188].

Graphene can be produced using a number of different methods, either from using scotch tape on graphite or more recently chemical vapour deposition, which is how most commercial graphene is produced [189]. Single layer graphene has a measured thickness of between 0.35 to 1.6 nm [190]. Commercially bought chemical vapour deposition monolayer graphene was purchased from Graphenea to be used in this work.

Sample patterning

The graphene from this study was transferred onto a Silicon/SiO_2 wafer. Both patterned and un-patterned graphene samples were produced to enable the comparison of nanobubble distribution and size. Patterned was produced on the graphene using e-beam lithography and reactive ion etching using oxygen and argon. The shape and size of the patterning of the sample was selected to determine the physical constraints on nanobubbles formation. Therefore four patterns were initially used; circles (dots) of graphene on silicon, holes of graphene on silicon, rings of graphene and silicon and ribbons of graphene and silicon. The dots and ribbons were selected as these shapes have previously been investigated showing some spatial control of nanobubbles [26, 27]. The

results from HS-AFM on the circles, holes and ribbons were less promising than the ribbons, so this thesis focuses on the rings. The ring patterned is shown in figure 4.1.

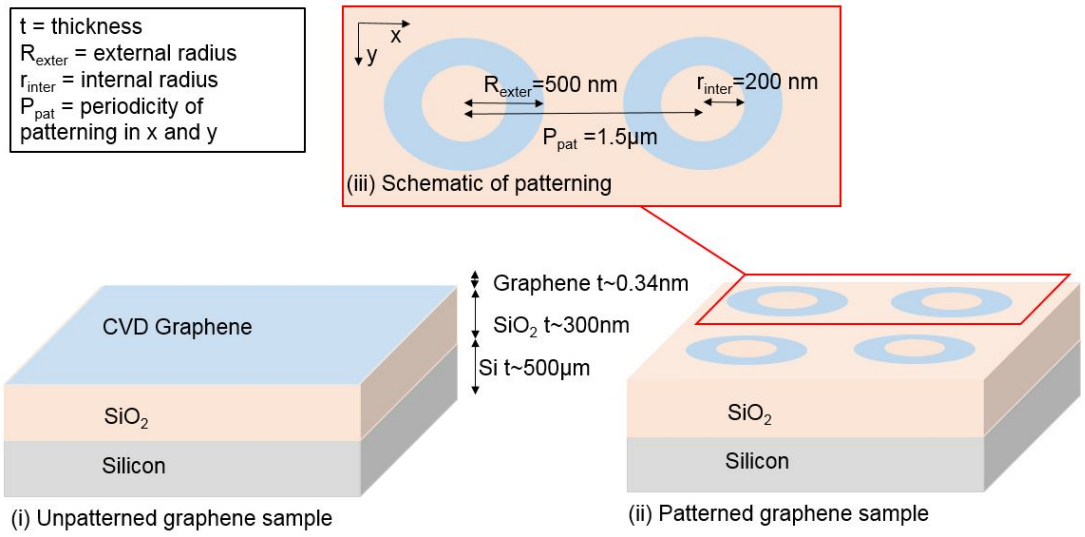

Figure 4.1 (i) unpatterned graphene sample (ii) patterned graphene sample, (iii) schematic of patterning.

Pattern checking

After the sample was prepared the pattern was checked using an optical microscope, see figure 4.2 for details. The optical microscope used was from the Imaging suite of the University of Exeter, Harrison Building.

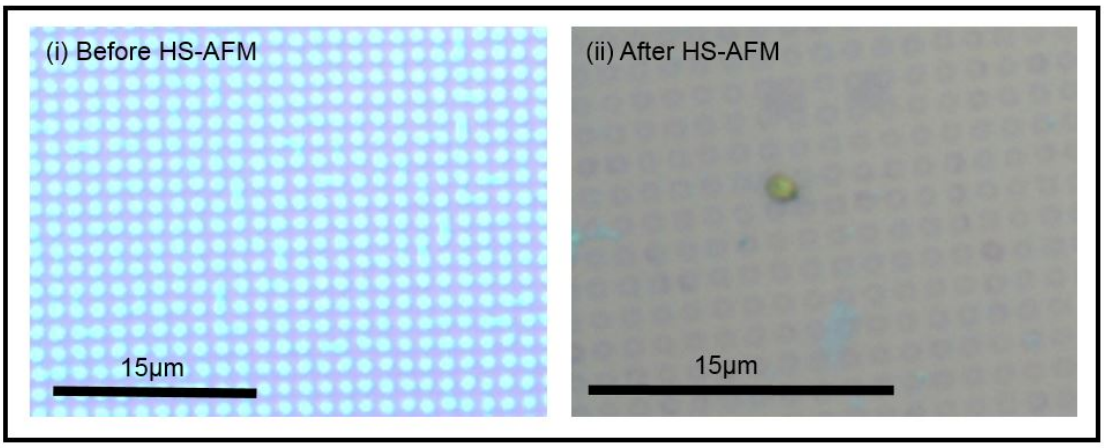

Figure 4.2 Optical imaging of patterning (i) before HS-AFM and (ii) after HS-AFM.

From figure 4.2 the patterning of graphene was effective with the pattern enduring after the high-speed atomic force microscopy measurements.

4.3 Characterization of mineral samples

Although many minerals can be identified visually, using characteristics such as luster, sheen or colour, rare earth minerals need to be characterized chemically to determine elemental enrichment and exact composition. This is particularly important for rare earth fluorcarbonates which are easily mistaken for each other due to their similar chemical composition and source locality [81]. A number of well-established techniques were used to identify exact mineral and elemental compositions of the minerals and aqueous solutions used in this work. These are; x-ray diffraction, x-ray fluorescence, inductively coupled plasma- mass spectrometry and mineral liberation analysis.

4.3.1 X-ray diffraction

The scattering of x-rays by crystals was first discovered by Max Von Laue in the early 20th century. Since its inception, X- ray diffraction (XRD) uses the diffraction of the x-rays on the crystal structure giving the lattice spacing with the use of the Bragg equation [191]. XRD data can be compared to the RRUFF database of established powdered diffraction patterns of mineral species from identified source localities [192]. The RRUFF database, was created as a resource of XRD data to compare mineralogy data. As well as XRD being of use to mineralogists, it can also be of interest to the pharmaceuticals industry to determine polycrystalline drugs [193, 194]. XRD is used regularly in mineral processing to determine the purity of mineral samples as it is more quantitative than either XRF or QEMSCAN [5, 195]. It is often used in combination with these methods. X-ray diffraction was conducted on the sample of dolomite used in the NC-AFM study of nanobubbles and the sample purity was determined to be 87.5%. The 12.5% of the sample that is not dolomite is predicted to be either calcite or ankerite, as these two carbonate minerals often occur alongside dolomite.

4.3.2 X-ray fluorescence

X-ray fluorescence (XRF) like XRD has been used to determine the mineral composition of samples since the 1960's, easily identifying the chemical composition of deposits [196]. XRF works by emitting X-rays towards a sample, and the secondary x-rays or fluorescent X-rays that return allow the identification of the chemical composition of the minerals, as different elements release electrons at different energy states. XRF is a quantitative measurement of the chemical abundance in samples, it is non-destructive and allows the identification of mineral species. Although commonly used in mineral processing, XRF is also applied in archaeology and art history to identify specific pigments related to specific time periods in antiquity [197].

XRF was used to identify the purity of the parisite samples from Snow Bird, Montana used in zeta potential measurements in Chapter 5. The XRF instrument was the ARL PERFORM'X Sequential X-Ray Fluorescence Spectrometer,10 Thermo Fisher at Colorado School of Mines, USA. The parisite- (Ce) mineral sample and XRF are shown in figure 4.3.

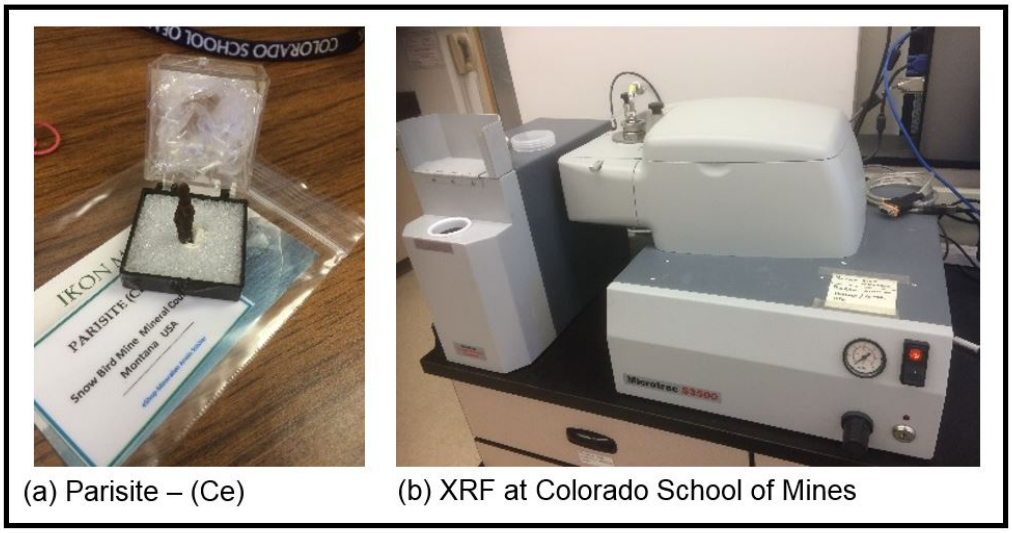

(a) Parisite – (Ce) (b) XRF at Colorado School of Mines

Figure 4.3 (a) Parisite- (Ce) sample used for zeta potential measurements (b) XRF instrument at Colorado School of Mines.

Before XRF the sample was ground via steel ring mill (Angstrom Model TE250 Ring Pulverizer) at Colorado School of Mines.

4.3.3 Inductively coupled plasma-optical emission spectrometry

Inductively coupled plasma- optical emission spectrometry (ICP-OES) is a highly sensitive technique which has been used widely since the 1990's to identify the elemental and isotropic composition of a sample [198]. Due to the ability to detect very small % of elements or ions, emission spectrometry has applications in a wide range of fields from forensic science to mineral processing [199, 200]. In mineral processing, emission spectometry can be used to analyse the chemical composition of supernatants [199, 201].

Supernatants are an aqueous solution composed of ions, which are released within the solution from the surface of the minerals in mineral processing. Supernatants are important in mineral processing as they can often interact with reagents altering the surface properties [202]. A supernatant is of significant interest for zeta potential measurements as it can alter or depress the surface of the mineral; it has previously been found to effect bastnäsite [7].

A supernatant from the Songwe Hill, Malawi ore was created by mixing the ore 20% solids 80% liquids (water) with the smallest size fraction and agitating with magnetic stirrer and heating to 60^{o}C for 30 minutes. The pulp was then filtered to separate the solids and the liquids. ICP-OES analysis was conducted to determine the major ions within the supernatant solution. The main ions to test were calcium, iron and magnesium. ICP-OES was conducted by Edgar Schach and Tom Leistner of Helmholtz Institute of Resource Technology, Freiberg. Measurements using ICP-OES showed 11.97 mg/L of Ca ions, 1.5 mg/L Mg ions and 0.05 mg/L of Fe ions in the supernatant.

4.3.4 Mineral liberation analysis

The aim of the invention of mineral liberation analysis (MLA) was to both identify and calculate the location of minerals within the sample. It was first produced in 2003 by the University of Queensland [203]. MLA combines Scanning electron microscopy with an energy dispersive spectra (EPS). Understanding the mineralogy of a deposit is key to enabling efficient processing and extraction of the ore minerals [204]. For selection of a processing method the key ore minerals and their exact percentage and association to other minerals is important. MLA is similar to other analytical techniques such as QEMSCAN. QEMSCAN shortened from Quantitative Evaluation of Minerals by Scanning Electron Microscopy is also like MLA an automated petrography instrument [204].

Since the invention of automated petrography such as MLA and QEMSCAN they have been used in a wide range of research from archaeology to minerals processing [205, 206]. As rare earth elements are often located within complex mineralogy, understanding the mineralogy is key to optimising and enabling processing [206]. For surface studies of the hydrophobicity of minerals, identifying and mapping the mineralogy of a complex ore is also key to make sure the location of the cantilever on the mineral is correct for the study.

4.4 Zeta potential measurements

The surface charge of particles in aqueous solution was first realised in 1807, when clay particles migrated under an applied electric field. Since then research into the surface charge of particles in aqueous solution has grown into a highly interdisciplinary field, important in industries ranging from mineral processing to DNA sequencing [60, 207]. There are many methods for determining the surface charge of particles; electrophoresis, electro-osmosis and streaming potential to name just a few [64]. These methods and the theory of measuring surface charge are covered in more detail in chapter 2. Less common methods such as atomic force microscopy can also be used to determine the zeta potential of surfaces, see section 4.5 for more details.

The zeta potential is the magnitude of the surface charge of a particle dispersion, and can be used to interpret the surface behaviour of minerals to improve processing using flotation [7, 60, 202]. In particular, the change in zeta potential under different chemical reagents can indicate the floatability of a mineral under that reagent, as changes in chemical bonding effects the surface charge [60]. Although zeta potential devices are now widespread in mineral processing labs, as they enable a quick measurement of a pure minerals surface charge, there are limitations to the measurements. As zeta potential measurements are usually conducted on pure minerals understanding a complex ore using only these measurements is challenging [7].

In this work, zeta potential measurements were conducted on a streaming potential instrument, seen in figure 4.4. Two different mineral samples were used for zeta potential measurements, parisite- (Ce) from Snow Bird, Montana and rare earth enriched apatite from Jacquira, Brazil. The mineral samples were suspended in water or collector solution at 0.02 g per 40 ml and then agitated on a shaking table for 20 minutes before each measurement. Surface behaviour measurements were conducted using the Microtrac Stabino Particle Charge Mapping surface chemistry device at the Colorado School of Mines, U.S.A.

The Microtrac Stabino Particle charge mapping is composed of a polytetrafluoroethylene (PTFE) cup in combination with an oscillating piston, for schematic see figure 4.4. The Stabino Particle charge mapping measures the temperature, pH, particle size, conductivity and particle potential. Titration is used to infer charge quantity, pH and conductivity. The titrates used in this study are NaOH or HCl. The Particle charge mapping immobilises a proportion of the particles at the wall of the cup, between the cup and piston. When the piston oscillates the electrical double layer of these particles is moved up and down. This oscillating electrical double layer produces an alternating voltage (streaming potential), which can be detected at the anode and cathode (See figure 4.4). This streaming potential can be used to calculate the zeta potential values of the mineral surface. A schematic of how streaming potential is measured is shown in

figure 2.5 (ii), within chapter 2. The relationship between streaming potential and zeta potential is shown below in equation 4.1.

$$\zeta = \frac{dU\ \eta\ K_B}{d\Delta P\ \ \varepsilon_o \varepsilon_{rs}} \qquad [4.1]$$

Where ζ is zeta potential, ε_o is permittivity of vacuum, ε_{rs} is permittivity of the electrolyte, K_B is electrolyte conductivity, η is dynamic viscosity of the fluid and $dU/d\Delta P$ is the slope of the streaming potential vs differential pressure. The permittivity of a vacuum is known to be 8.85 x 10^{-12} F/m. Pressure change can be calculated using the dimensions of the cup and piston and the oscillation of the piston.

Equation 4.1 is a derivation of the Helmholtz-Smoluchowski equation described in equation 2.1 in chapter 2. The background of the measurement of zeta potentials is further explored in chapter 2, section 2.3.2.

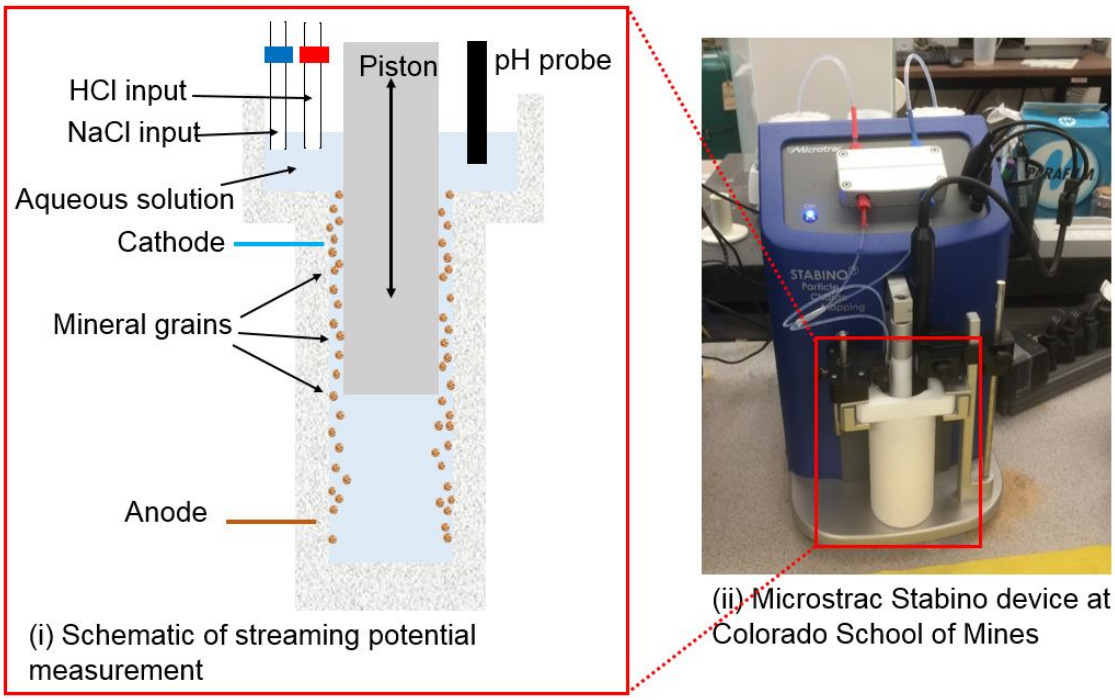

Figure 4.4 (i) Schematic of streaming potential measurement (ii) Microtrac stabino device at Colorado School of Mines.

The streaming potential device starts the measurement at high or low pH and then slowly adds either NaOH or HCl to lower or increase the pH. Chapter 5 further explores the surface behaviour of rare earth fluorcarbonate minerals and rare earth enriched apatite.

4.5 Atomic force microscopy

Atomic Force Microscopy (AFM) was originally invented in the 1980's to image the surface of materials [118], it was discovered as a result of earlier work on scanning electron microscopy [208]. The AFM uses a force instead of an electric current to produce a high resolution image of the surface in very small areas. AFM can produce images well below the optical diffraction limit with a resolution in an order of 1 nm [209]. An AFM consists of; a stand for the sample to be located; a small cantilever with a sharp tip which interacts with the surface of the material; a piezoelectric device to move the cantilever; a laser which reflects off the cantilever and a photodiode to detect the reflected laser and finally a computer to interpret the laser feedback, move the piezoelectric device and construct a topography image out of the data. A selection of these components are shown schematically in figure 4.5.

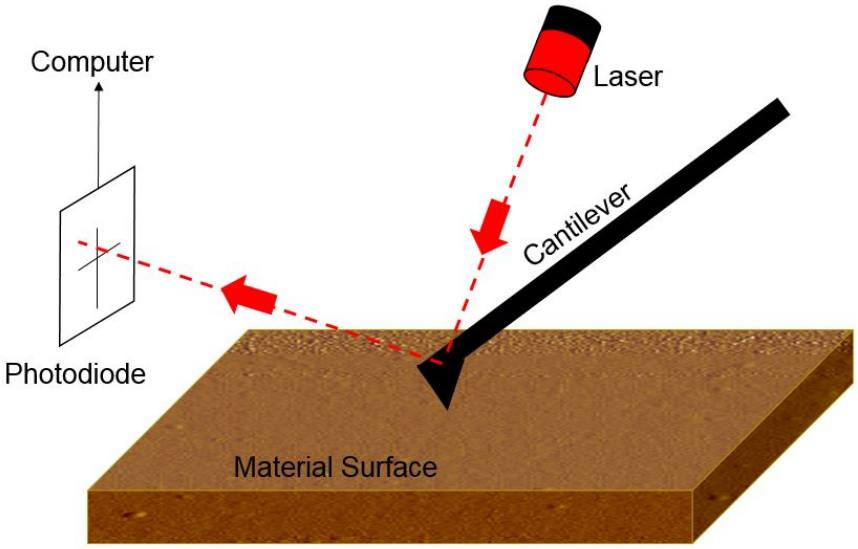

Figure 4.5 Schematic of atomic force microscopy.

Atomic force microscopy can be used in a number of different modes such as contact mode AFM, non-contact AFM and tapping mode AFM (sometimes called dynamic mode), see figure 4.6 [210]. In contact mode, the cantilever tip is always in contact with the surface via a constant force kept constant by feedback loop. This mode is most effective at imaging hard surfaces such as minerals [211]. Non- contact mode denotes where the tip is suspended above the surface by 50-150 angstroms, and attraction forces between the tip and surface are measured [212] .Non- contact mode can be used to image a wide number of more soft particles such as DNA, but surface contamination in NC-AFM can reduce resolution [213]. Tapping mode AFM (TM-AFM), where the cantilever oscillates in and out of contact with the surface, only tapping at the surface at the far arc of each oscillation, stops any surface friction encountered under contact mode [214]. TM-AFM enables the production of a phase image, which indicates the adhesiveness of the tip to the surface and the properties of the surface, such as its hardness. TM- AFM was used to image the first nanobubbles, and subsequently has been widely used to image nanobubbles, it is also often used to image biological samples and polymer molecules [17, 19, 27, 108]. Although there are additional modes that have been developed such as PeakForce Tapping of AFM they are not covered here due to limits of the scope of this thesis.

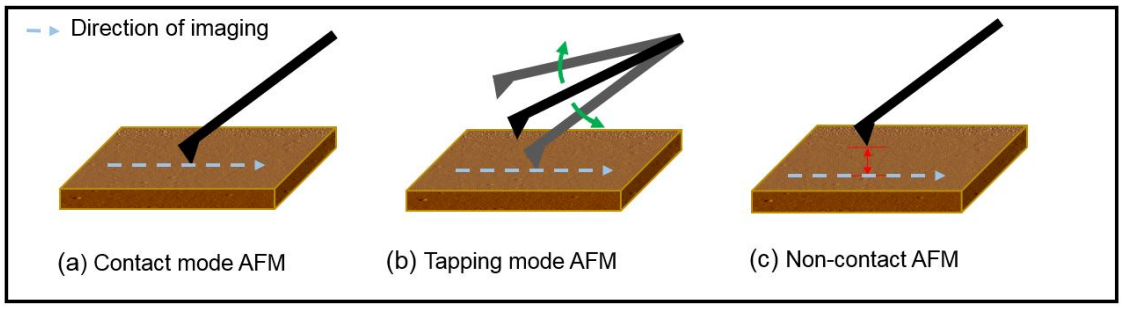

Figure 4.6 Schematic of modes of AFM (a) contact mode (b) tapping mode (c) non-contact mode.

As AFM depends on the interaction between the surface and the cantilever tip, the selection of cantilever is vital for the effective imaging of the surface. The cantilever spring is a measure of how strong the cantilever is; this can be

calculated using Hooke's Law. The equation used to calculate the force constant depends on the cantilever geometry and tip constraints [210]. Cantilevers are produced for specific modes of AFM, with force constants on the cantilever ranging from between 0.01 to 72 N/m (AFM Probes stocklist). The explosion of uses for AFM, ranging from biological to chemical, enabled significant growth in the types and properties of cantilevers available, with many types of cantilevers for each mode of AFM. As well as the force constant varying between cantilevers other factors can also be altered, these include material of cantilever, resonate frequency of cantilever oscillations, tip length and tip shape. Historically cantilevers have been made out of silicon or silicon nitride with coatings such as aluminium, chromium or gold [215]. The length of cantilever used can vary between micrometres and nanometres depending on the sample being imaged.

Atomic force microscopy can be conducted in a number of environments, from atmospheric air to in liquid and even in a vacuum [15, 216, 217]. The setup of the AFM and oscillation of the cantilever varies between environments, as the medium effects a number of parameters including, Van der Waals forces at the surface and the movement of the cantilever due to the different densities of mediums [217]. In chapter 6 and 7 both AFM and HS-AFM are setup in liquid cells although the type of liquid cell varies.

Atomic force microscopy can be used to calculate zeta potential measurements using force curve measurements, although the most common methods are still electrophoresis or streaming potential methods highlighted in section 4.4 [218]. Calculating zeta potentials can be done by using the Derjaguin, Landu, Vervey and Overbeek (DVLO) theory of surface charge to convert force curves to zeta potentials [219, 220, 221]. Comparing conventional electrophoresis zeta potential measurements with zeta potential measurements calculated using atomic force microscopy shows good agreement at specific ionic strengths although surface roughness effects the values calculated from AFM [222]. This method of measuring zeta potentials is not used in this thesis as it requires specific AFM setup.

For this work dynamic amplitude modulated non- contact atomic force microscopy was used to image nanobubbles at the surface of minerals. Nanobubbles are tiny gas bubbles at the surface of hydrophobic materials and are of interest in processes such as mineral processing and food manufacturing. Imaging them has previously been conducted using tapping mode atomic force microscopy, although the method of non- contact AFM used in this work enabled the production of a phase image, which is usually a hallmark of tapping AFM. For more details of nanobubbles see chapter 3.

Non-contact atomic force microscopy (NC-AFM) was conducted on a Park Systems (South Korea) atomic force microscope XE100 located in Helmholtz Institute Freiberg for Resource Technology, Germany, see figure 4.7. The atomic force microscopy was used in non-contact mode as contact mode was too strong to measure nanobubbles and removed them from the image. This movement of nanobubbles by contact mode AFM has previously been shown by Dietscherlein *et al.,* [155]. The NC- AFM was combined with Raman spectroscopy which allowed the classification of different minerals, identifying synchysite and carbonatite gangue minerals within the ore sample. Two types of cantilevers were used (Contact cantilever Park systems nanotechnology solutions partner PPPCONTSCR10M and ContAl-G Cantilever) both had a spring constant of 0.2 N/m. Images were produced in either 36 µm x 36 µm or 8 µm x 8µm sizes. For more details of the setup and experimental parameters used see chapter 6, section 6.3.

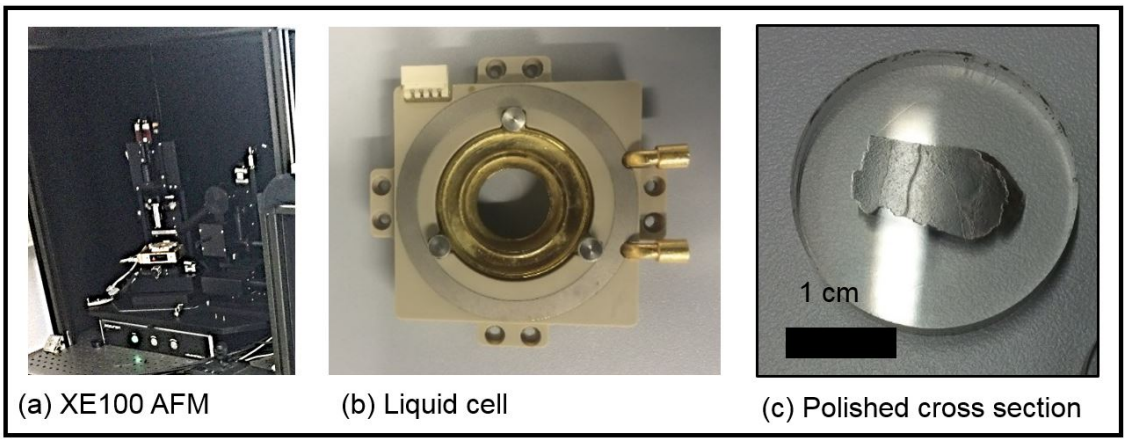

Figure 4.7 (a) XE100 atomic force microscopy (b) liquid cell (c) polished mineral cross section.

Chapter 6 describes the results of the NC-AFM experiments into nanobubbles on mineral surfaces.

4.6 High-speed atomic force microscopy

Although AFM has many uses in life and engineering sciences, the long times required to take measurements is an obvious limitation. Since the invention of the AFM, there have been drives for faster systems enabling the imaging of dynamic processes, with the first step in the direction of high- speed atomic force microscopy in 1991 [223, 224]. High-speed atomic force microscopy (HS-AFM) is conducted under much faster time scales, instead of taking 30 seconds to image a sample, high-speed atomic force microscopy takes images in the orders of milliseconds [225]. However due to the high speed, the base sample not the cantilever moves by piezoelectric movement of the stage. A schematic of HS-AFM is shown in figure 4.8.

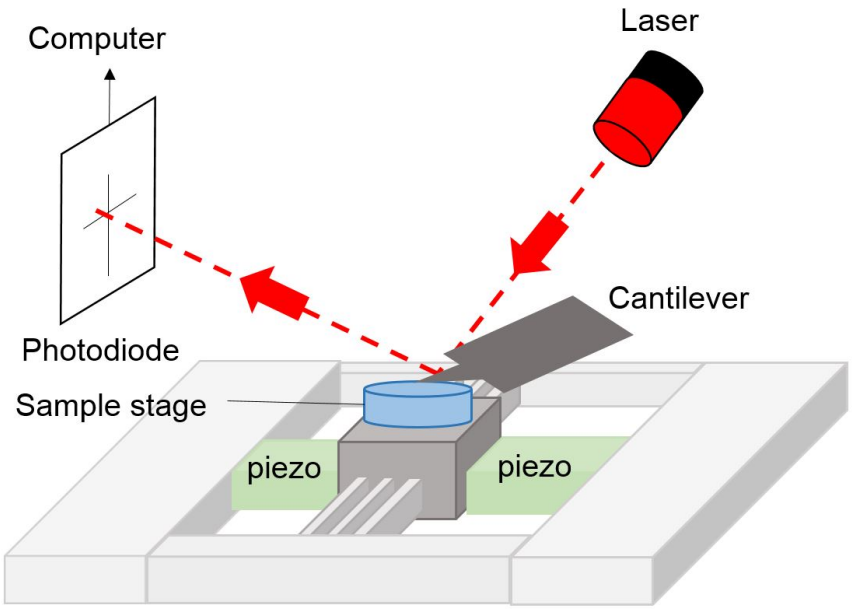

Figure 4.8 Schematic diagram of high-speed atomic force microscopy adapted from Picco et al., [226].

The first publication of the uses of high- speed atomic force microscopy was the imaging of the Brownian motion of the protein myosin V [224]. Since then, high-speed atomic force microscopy has been used in a wide range of fields from surface science to biology. In biology, HS-AFM is of particular interest in tracking movements on the cellular level and can be used to image a wide range of phenomena from algae virus's, opening of DNA cuboids to walking myosin along actin tracks [227, 228, 229]. In surface science, high-speed atomic force microscopy has been used to image nanobubbles at the graphite water interface [124], track the growth of crystal grains of calcite, and measure the diffusion of point defects in crystals [230, 231].

In this work, high-speed-atomic force microscopy, from Nano systems (Bristol University) located at the Single Cell Genomics Facility at Plymouth Marine Laboratory, was used to image nanobubbles on the surface of graphene. The HS-AFM was designed by Bristol Nano dynamics group. The HS-AFM has previously been shown to be an ideal tool for material science [232], and in this work was combined with a liquid cell [227]. The HS-AFM setup is shown below in in figure 4.9.

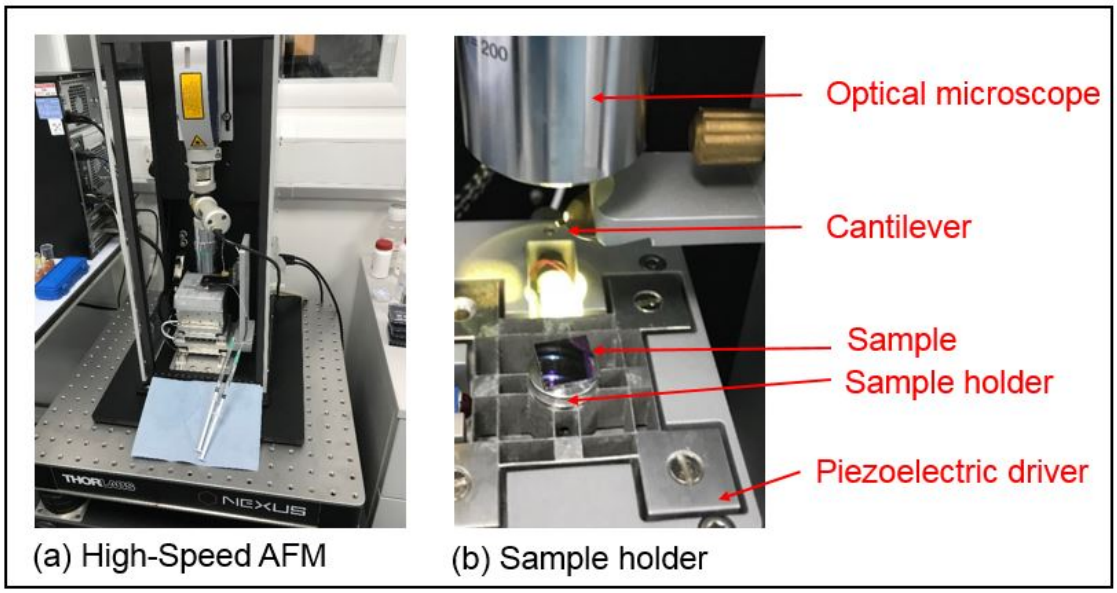

Figure 4.9 (a) High-speed atomic force microscopy at Plymouth Marine Laboratory (b) sample holder.

Before measurements sample surfaces were cleaned by washing with 3 mins with acetone then 3 minutes with IPA (100% purity) the graphene was then dried with nitrogen gas. The sample was set on top of the carbon sample holder using an adhesive. The optical microscope was used to locate the patterned areas of the sample. Once the cantilever was located in the patterned section nanobubbles were produced using solvent exchange. The results and full methodology of this work is discussed in chapter 7.

4.7 Summary of samples

Sample	Experiment	Chapter
Parisite- (Ce), rare earth fluorcarbonate mineral	Zeta potential measurements	5
Apatite, phosphate mineral enriched with rare earth elements	Zeta Potential measurements	5
Synchysite– (Ce), rare earth fluorcarbonate mineral (Songwe Hill ore sample)	Non -contact atomic force microscopy	6
Dolomite, carbonate mineral	Non-contact atomic force Microscopy	6
Monolayer graphene	High-speed atomic force Microscopy	7
Patterned monolayer graphene	High-speed atomic force microscopy	7

Table 4.1 List of samples used in this thesis and their chapter location

4.8 Summary

In this chapter, the various materials and methodologies used in the investigations of surface behaviour and nanobubbles are overviewed.

Mineral samples of rare earth fluorcarbonates, rare earth enriched apatite and dolomite were characterised using x- ray diffraction, x-ray fluorescence, and mineral liberation analysis. A supernatant produced from a rare earth ore sample was analysed using inductively coupled plasma- mass spectrometry. Commercially available graphene was patterned using e-beam lithography and refractive ion etching, the pattern was checked using an optical microscope.

The background of the experimental techniques of atomic force microscopy and zeta potential measurements were discussed. The history and uses of zeta potential measurements were highlighted with the specific experimental setup used to investigate the surface behaviour of minerals described. The framework and modes of atomic force microscopy were outlined with the uses of tapping, non-contact and contact reviewed. The requirements of imaging nanobubbles were also covered.

In conclusion, the experimental setup was covered; from zeta potential measurements of rare earth enriched minerals (chapter 5), to non-contact atomic force microscopy of nanobubbles on minerals (chapter 6) to high-speed atomic force microscopy on patterned and unpatterned graphene (chapter 7).

Chapter 5
Zeta potential measurements of parisite and rare earth element enriched apatite

5.1 Overview

Rare earth elements (REE) are important for modern technology and are used widely in renewable and hi technology. The sourcing of REE from mineral deposits is complex, with a convoluted extraction process often hindering developments of new deposits. Flotation is the most common method of extracting these minerals. The measurements of the surface charge of minerals, using zeta potentials, is a key method in determining flotation efficiency for specific chemical reagents.

The rare earth fluorcarbonate mineral parisite, and the phosphate mineral apatite, have been identified as possible sources of future REE. In this chapter, the zeta potential measurements of the rare earth fluorcarbonate mineral parisite (section 5.2 and section 5.3) and rare earth element enriched apatite are investigated (section 5.4 and section 5.5). These zeta potential results are then compared to previous investigations into other rare earth fluorcarbonates and non- rare earth enriched apatite.

5.2 Parisite sample

Parisite is a rare earth fluorcarbonate mineral containing up to 54% TREO (total rare earth oxide) [9]. Although less common than bastnäsite, parisite has been found at a number of locations with possibilities of economic extractions of REE [233, 234]. For more details of the rare earth fluorcarbonates and a comparison of their crystal structure see chapter 2, section 2.2.2. There has been little research into the surface behaviour of parisite making measurements of the zeta potential vital for future processing of new deposits.

5.2.1 Mineral sample

A mineral sample of parisite-(Ce) from Snow Bird Mine, Mineral Country, Montana, USA was acquired from Ikon Minerals. Parisite-(Ce) is the only REE fluorcarbonate mineral identified at the Snowbird Fluorite REE deposit. The sample used was large (approximately 10cm long), and yellowish brown/brown in colour, consistent with parisite samples from this locality [235, 236]. The sample purity was analysed using XRF (ARL PERFORM'X Sequential X-Ray Fluorescence Spectrometer, Thermo Fisher), at the Colorado School of Mines, and the elemental compositional analysis is shown in table 5.1 (full results are in appendix)

Compound	**Wt %**
Y_2O_3	2.73
La_2O_3	16.99
$Ce\ O_2$	33.62
Pr_6O_{11}	3.67
$Nd_2\ O_3$	13.09
Sm_2O_3	1.81
Gd_2O_3	1.57
CaO	13.46
ThO_2	2.75
BaO	2.67
$Si\ O_2$	2.23

Table 5.1 X-ray fluorescence results from parisite sample showing oxide composition. wt % is stated for all values >2%. For a full list of elemental composition see appendix, table A.1.

.

From XRF analysis, the parisite-(Ce) is fluorine depleted with high concentrations of the REEs, cerium, lanthanum and neodymium, and contains barium and silicon. These results are in agreement with previous analysis from Metz [184], who found significant concentrations of calcium, cerium, lanthanum, neodymium, praseodymium and yttrium in parisite–(Ce) from Snowbird.

5.2.2 Preparation

The parisite-(Ce) sample was a single mineral, virtually free from contamination and was first ground via steel ring mill (Angstrom Model TE250 Ring Pulverizer) to 100% passing 80 μm. Due to the paucity of the mineral sample, grinding curves to establish the time to reach the target particle size distribution were produced using proxy samples of calcite [237]. More details of calcite and REE fluorcarbonate properties can be found in Miyawaki *et al.,* [238] and Pavese *et al.,* [239].

5.2.3 Zeta potential measurements

Two types of collectors were acquired, a fatty acid supplied by Betachem (product name Betacol CKF 30B) and hydroxamic acid (product name AM810) supplied by Axis House, South Africa. These collectors were selected as hydroxamic and fatty acids are the most common collectors used in bastnäsite flotation, therefore zeta potential results from parisite can be compared to bastnäsite [5]. These are also the reagents used in the study of surface nanobubbles on dolomite in chapter 6.

The supernatant from a mixed calcite/ankerite/synchysite/apatite ore was created by diluting the ore to 20 % (wt) with DI water and heating to 60^{o} C for 30 minutes whilst agitating with a magnetic stirrer at 120 rpm. The solids were then separated via filtration. The supernatant was generated to approximate conditions in a flotation system of a mixed ore. Measurements using ICP-OES

on an identical sample showed 11.97 mg/L of Ca ions, 1.5 mg/L Mg ions and 0.05 mg/L of Fe ions in the supernatant.

The mineral samples were suspended in water or collector solution at 0.02 g per 40 ml and then agitated on a shaking table for 20 minutes before each measurement. Surface behaviour measurements were conducted using the Microtrac Stabino Particle Charge Mapping surface chemistry device at Colorado School of Mines, U.S.A. The measurement technique used for measuring the surface charge was streaming potential. Measurements were conducted from pH 3.5 to pH 11, with NaOH and HCl were used to adjust pH.

5.3 Parisite results

5.3.1 Water conditions

The surface charge of parisite was measured as a function of pH in water, between pH 3.5 and pH 11, the results are shown in figure 5.1. The iso electric point for parisite-(Ce) was measured at a pH of 5.6 in water. The charge of parisite decreases linearly as pH increases above 6, suggesting an uptake of negatively charged species at the surface (or the loss of positively charged species at the surface). Although most surfaces are positively charged at acidic pH and negatively charged at base pH [63], the magnitude and gradient of the zeta potential results agrees with those of bastnäsite [57, 75]. The sign and magnitude of the charge indicate the uptake of different species in the solution. In semi-soluble salts such as bastnäsite [238], the main species of potential determining ions that are at the surface have been found to be CeF, $CeFCO_3$, $Ce(OH)_3$, CeF_3 [83], as shown in table 5.2. As parisite and bastnäsite have largely the same composition, apart from a higher Ca content in the parisite, it is reasonable to assume that the surface ions are controlled by some of the same species. Further work could explore this area in more detail.

pH Range	Ions
<5.2	CeF
5.22–5.74	$CeFCO_3$, CeF_3
5.74–8.55	$CeFCO_3$
8.56–10.12	$CeFCO_3$, $Ce(OH)_3$
>10.2	$Ce(OH)_3$

Table 5.2 Ions affecting surface behaviour of bastnäsite zeta potentials over different pH ranges. Taken from Jordens et al., [57] adapted from Herrera-Urbina et al., [83].

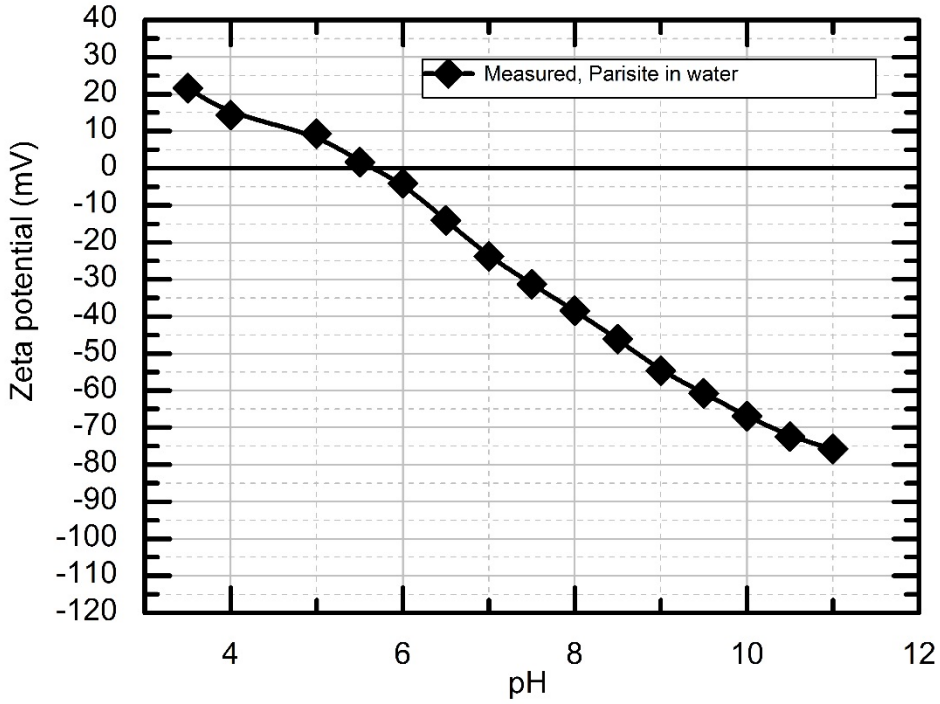

Figure 5.1 Measured surface charge (mV) of parisite under water as a function of pH.

The zeta potential measurements obtained for parisite can be compared to previous research conducted on bastnäsite (table 2.4). The IEP of the parisite sample recorded was 5.6; this lies towards the lower end of previous IEP values obtained for bastnäsite, which ranged from pH 4.7 to pH 9.3. The size of the mineral sample at 100% passing 80µm was also larger than the majority of other studies reviewed in table 2.4, however a direct comparison of grind size is difficult due to the differences in sample analysis. The background for

measurements was water, the same as for bastnäsite samples by Ren *et al.,* [78].

Of the twenty one previous studies of bastnäsite, fifteen were identified as having extractable zeta potential values. Of these fifteen, five were selected due to their specification of purity of the sample of bastnäsite used in the study [57, 76, 78, 77]. It must be noted that the samples had both different source localities and that they were measured under different electrolytes. The results of Anderson [75] were additionally selected due to the use of the same experimental equipment and methodology. These are compared to the results obtained for parisite in Figure 5.2, where, for each study, six values of zeta potential at pH values around 3, 5, 6, 7, 9, 11 were extracted.

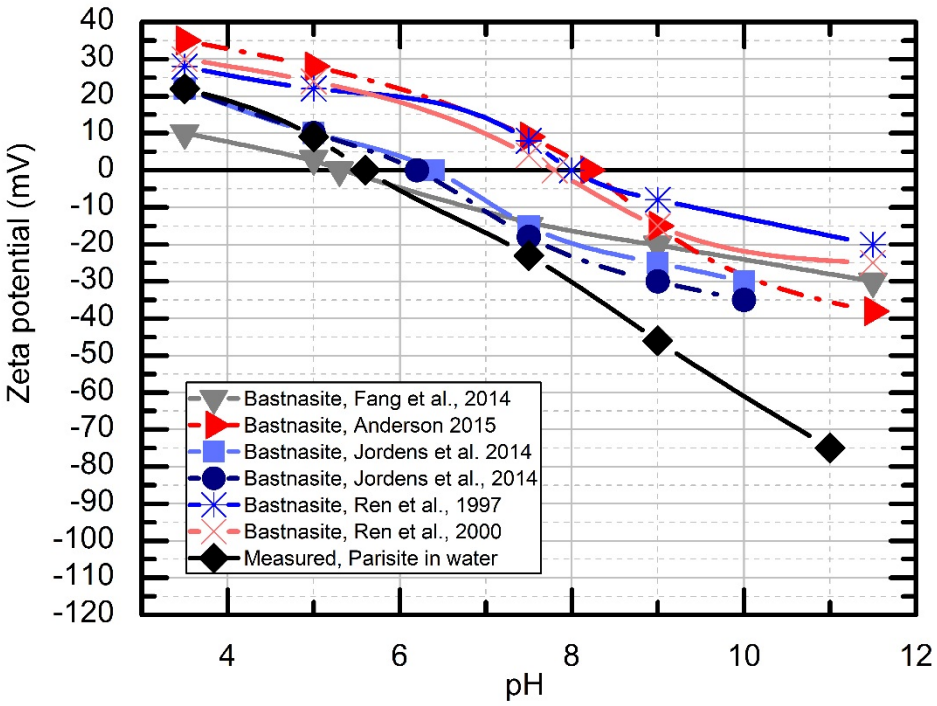

Figure 5.2 Comparison of literature values of bastnäsite surface charge in water and the measured surface charge of parisite in water.

As can be seen in Figure 5.2, the zeta potential measurements for bastnäsite and parisite share many similarities. The IEP of parisite obtained lies between the values of the selected studies of pH 5.3 (Fang *et al.,* [76]) and pH 8.2

(Anderson [75]). The value of zeta potential at pH 3.5 of four of the six studies was between 20 and 35 mV which is within the range of the parisite value of 21 mV. The results at more alkaline pH differ to a greater degree, with parisite having a zeta potential of -76 mV at pH 11.5; although this value is much greater than the nearest bastnäsite selected for this comparison, (-40 mV from Anderson [75]), Pavez *et al.,* [240] recorded a surface charge of -70 mV at pH 11.5 for the sample of bastnäsite from Brazil [240]. If directly compared to bastnäsite from the study by Anderson [75], the IEP for parisite is lower than bastnäsite.

5.3.2 Collector conditions

Both hydroxamic acid and betacol (fatty acid) are anionic collectors and as such it can be expected that they would reduce the surface charge of the mineral surface. In figure 5.3, the zeta potential (mV) of parisite measured under water, hydroxamate (5 x 10^{-4} mol/L) and fatty acid (5 x 10^{-4} mol/L) conditions as a function of pH is shown.

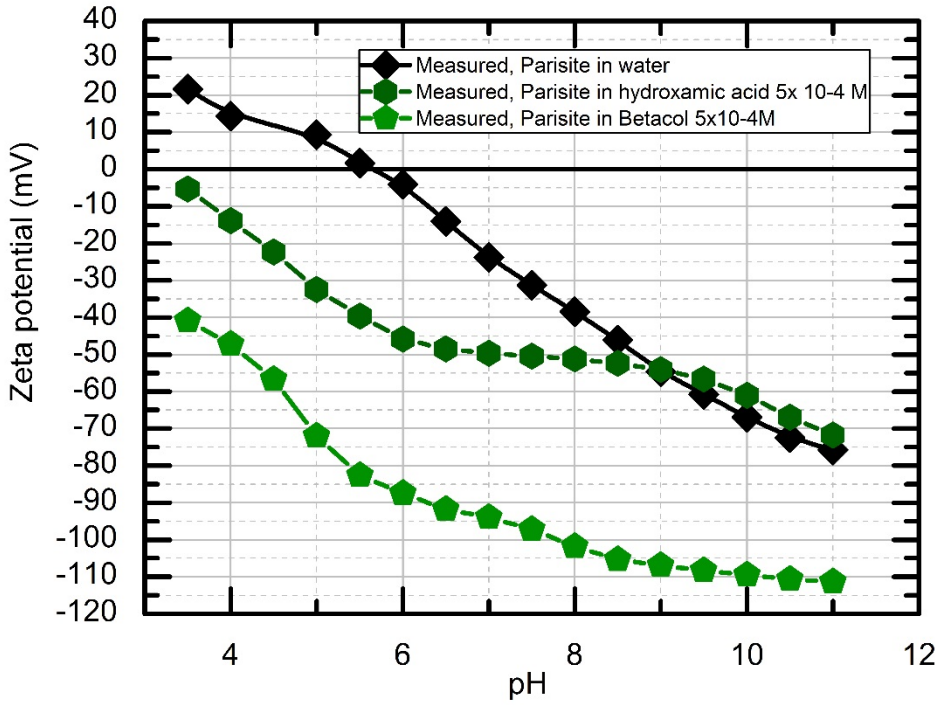

Figure 5.3 Measured surface charge (mV) of parisite under water, hydroxamate and fatty acid conditions as a function of pH.

Both hydroxamate and fatty acids reduce the surface charge so the IEP<3.5, with the surfaces negatively charged between pH 3.5 and pH 11. This is a shift of the IEP by a minimum of 2.1 from the IEP of parisite in water at pH 5.6. The hydroxamic acid affects the parisite surface to a lesser degree than the fatty acid, reducing the surface charge at pH 3.5 to -5.3 mV compared to -40.9 mV for betacol. Between pH 9 and pH 11 the zeta potential of parisite in hydroxamic acid is more positive than parisite in water. Zeta potential measurements by Sarvaramini *et al.,* [72], on bastnäsite treated by hydroxamic collector found a similar trend between pH 9 and pH 11 with investigations by fourier-transform infrared spectroscopy (FTIR) showing less negatively charged heptyl hydroxamic acid anions attached to the surface between these pH values.

As surface charge is an indication of the hydrophobicity of the surface, the more negative the surface charge the more hydrophilic the mineral surface. The results in figure 5.3 are counter to expectations as collectors, such as hydroxamic acid, are added to increase hydrophobicity. Hydroxamic acids are thought to form in multilayers at the surface of bastnasite, increasing the floatability of the mineral [57,60]. If there were nanobubbles formed at the surface of the mineral during zeta potential measurements, it would be expected that such a multilayer could form, due to the attachment of the hydroxamic acid to the gas interface of the nanobubble. These nanobubbles could increase the floatability of the mineral surface, producing the increased hydrophobicity that is expected under collector conditions.

Nanobubbles at the surface of minerals have never been detected during flotation due to limits of instrumentation, however they are thought to play a significant role in flotation [20]. Nanobubbles have been measured at the surface of minerals in cross section, and can be formed due to changes in temperature, which induces gas oversaturation [16, 24]. More details of nanobubbles in mineral processing can be found in chapter 3, section 3.5. Froth flotation involves steps which include the heating of both the mineral and liquid suspension. Heating is known to increase nanobubble populations and

therefore flotation can be seem as conducive to nanobubble formation. Nanobubbles could play a role in the results seen in figure 5.3 however due to limitations of experimentation this is not explored further in this thesis.

While absolute values of zeta potential are of interest, it is the response to different surfactants that is of particular importance for REE processing. Values from literature suggest that under collector (hydroxamate) conditions, parisite also behaves similarly to bastnäsite. The shift of the parisite IEP to a lower value under hydroxamate conditioning agrees with the majority of previous investigations, excluding Jordens *et al.,* [57]. Anderson [75] recorded a shift to an IEP of 6.6 (10^{-4} M of hydroxamic acid) and 5.2 (with 10^{-3} M of hydroxamic acid) under hydroxamate conditions. Saravaramini *et al.,* [72] and Azizi *et al.,* [74] both conducted zeta potential measurements with samples conditioned in Aero brand collector hydroxamates, this moved the IEP of bastnäsite from 7 to 5.8 and 7 to 4 respectively. This agreed with earlier work by Ren *et al.,* [77] and Pavez *et al.,* [79]. In comparison, Jordens *et al.,* [57] found a shift to a higher IEP value of 8.9 with the bastnäsite from Mountain Pass, and a pH of 7.6 with the bastnäsite from Madagascar. This was attributed to the use of a different type of hydroxamic acid, a benzohydroxamic acid instead of octyl hydroxamic acid. Jordens *et al.,* [57] suggesting that the increase in surface charge may have been due to the adsorption of REE metal hydroxamate complexes onto the mineral surface.

Two studies were selected to compare the effect of hydroxamic acid on bastnäsite and parisite (Ren *et al.,* [78] and Anderson [75]), shown in Figure 5.4. These two studies were selected as Ren *et al.,* [78] used a highly pure bastnäsite sample, whereas Anderson [75] used the same methodology and equipment used for parisite in our investigation. In both studies, the IEP of bastnäsite shifted to a lower value under hydroxamate reagent addition. As can be seen in figure 5.4, the hydroxamate lowers the zeta potential of the bastnäsite across the entire pH range investigated by all studies, as it does for

the parisite investigated in this study. In Ren *et al.,* [78] the hydroxamate (named MOHA) was proven to chemisorb onto the mineral surface with maximum adsorption occurring at pH 8-10, with the hydroxamate shown to chelate with the cerium ions at the surface of bastnäsite. Anderson [75] showed adsorption was also chemical in nature with greater adsorption at elevated temperatures. The similarities in the observed behaviour of bastnäsite and parisite, as seen in figures 5.2 and 5.4, suggest that hydroxamate also chemisorbs onto parisite.

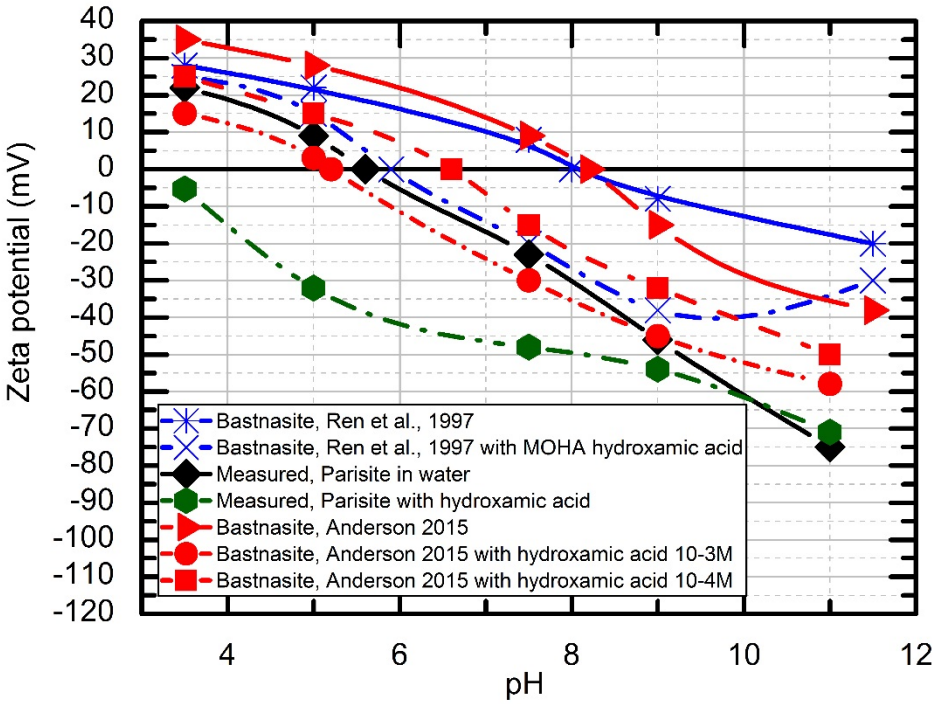

Figure 5.4 Zeta potentials of bastnäsite under DI water conditions [78, 75], under hydroxamic acid MOHA conditions [78], and under hydroxamic acid conditions [75]. Measured zeta potentials of parisite in water and in hydroxamate in 5 x 10^{-4} M/L.

5.3.3 Supernatant conditions

The surface charge (mV) of parisite in supernatant from Songwe Hill ore, Malawi was measured as a function of pH, shown in figure 5.5. Figure 5.5 shows that the zeta potential of parisite at pH 3.5 changed from 21.6 mV in water to -1.1 mV with supernatant background. In supernatant background, the zeta potential decreases by 10.2 mV, between pH 7 and pH 11, whilst between pH 7 and pH 3, the value changes by 38.9 mV, suggesting a greater effect at lower pH values. Between pH 7 and pH 11 the zeta potential of parisite in supernatant was higher than parisite in water. Espiritu *et al.,* [202], who conducted zeta potential measurements of bastnäsite in dolomite supernatant, between pH 8.2 and pH 10 the zeta potential of bastnäsite under supernatant was more positive than bastnäsite in water. Previous work by Espiritu *et al.,* [202] linked the lowered surface charge under supernatant conditions of a carbonatite to adsorption of carbonate ions at the surface of the mineral [202].

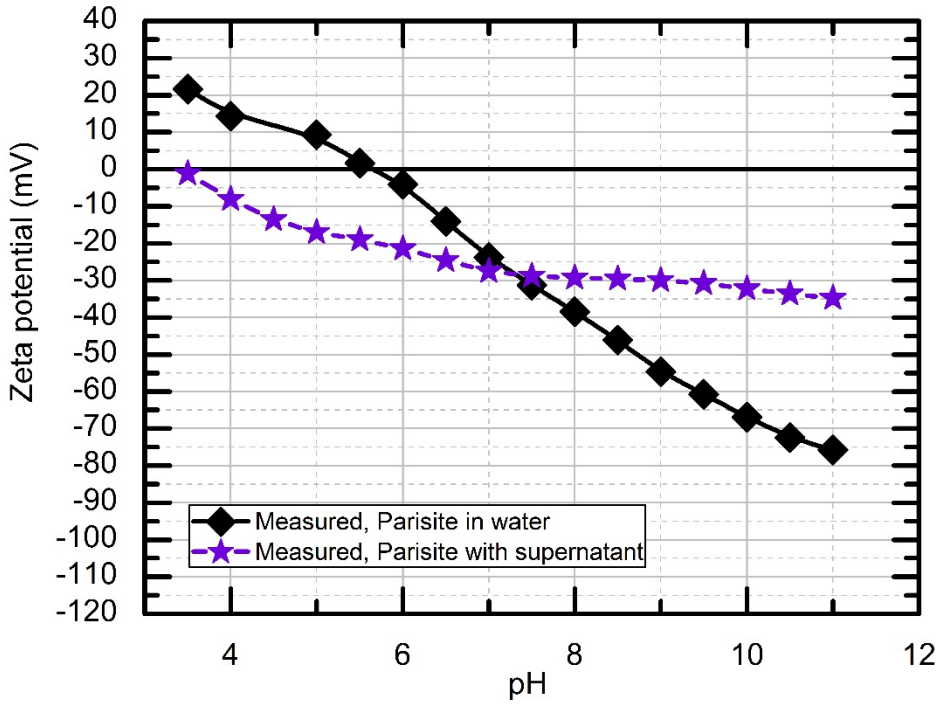

Figure 5.5 Measured surface charge (mV) of parisite under water and supernatant conditions as a function of pH.

To compare the effect of the supernatant on parisite to the effect on bastnäsite, results from this research were compared to values from Espiritu *et al*., [202], with values of zeta potential plotted as a function of pH in figure 5.6. Analysis (using ICP-OES) of the supernatant used in our investigation indicated the presence of calcium ions, magnesium ions and iron ions in small quantities. In contrast to the behaviour under water conditions, the measured zeta potential of both bastnäsite and parisite has a weak dependence on the pH under supernatant conditions. The depression of the zeta potential to a set charge is in line with previous research by Al Marouqi *et al.,* [241] which showed zeta potential does not change as a value of pH but as a function of pCa ions. Although work has been undertaken regarding the solubility of hydroxylbastnäsite by Voigt *et al.,* [242], there has been no specific studies on the solubility of parisite, therefore differences between the two cannot be determined [242]. The effect of the supernatant is important for future processing of parisite and the other REE fluorcarbonates, as effects on the surface charge could affect or be an indicator of collector adsorption [243].

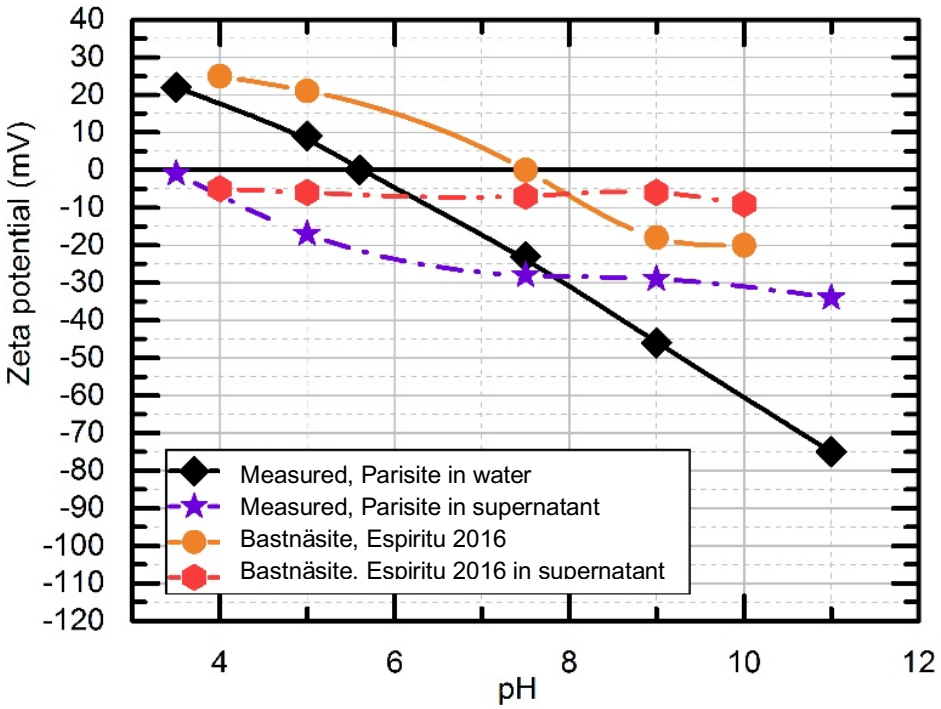

Figure 5.6 Zeta potentials extracted from published data from Espiritu et al.. [202] on the supernatant of dolomite and its effect on the zeta potential of bastnäsite. Measured zeta potentials of parisite in water, and under supernatant from Songwe Hill, Malawi.

As the main difference between parisite, bastnäsite, röntgenite and synchysite is small changes within the calcium content, and parisite and bastnäsite appear to have corresponding surface behaviour it is reasonable to expect this would extend to röntgenite and synchysite.

Although further work is required to investigate the application of these findings to mineral separations, if the surface behaviour of REE fluorcarbonates is the same across the series, then much of the research that has been conducted on bastnäsite deposits could be applied to synchysite, röntgenite and parisite deposits. Currently there are multiple deposits with REE fluorcarbonates under exploration such as Springer Lavergne, Quebec containing synchysite (Ce) and Mt. Prindle, AK, USA containing synchysite and parisite [81].

Applying bastnäsite surface behaviour, in particular the Mountain Pass and Bayan Obo deposit research, to other REE fluorcarbonate deposits already occurs, particularly when synchysite is not the principle ore mineral [244, 245]. It is challenging to quantify how widespread this practice may be as it is rare to publish details of the processing [246], however these results provide the first step towards scientific validation of this approach. In exploration and development of REE deposits, not only is the deposit size vital but, particularly in the case of REE, the ease of extraction is extremely important. If it is possible to predict that all REE fluorcarbonates behave in a similar way to bastnäsite during flotation, then much of the research that has already been conducted into surface behaviour with regards to reagent addition remains valid. The surface behaviour of rare earth fluorcarbonates will be further explored in chapter 6 using atomic force microscopy.

5.4 Apatite sample

Apatite, the world's main source of phosphate, can become enriched with rare earth elements during hydrothermal alterations [185]. See chapter 2, table 2.5, for a selection of rare earth enriched apatite deposits. Rare earth enriched apatite creates an attractive option for mining for the dual purpose of both phosphate and rare earth elements. However currently there is little understanding on the effect of REE enrichment on the processing via flotation of apatite.

5.4.1 Mineral sample

Apatite from Jacupiranga, Brazil was used for zeta potential measurements (Acquired from Dr Broom-Fendley, Camborne School of Mines, University of Exeter, UK). Samples from the same location have previously been used in Broom-Fendley *et al.,* [46]. Jacupiranga is a well-studied alkaline carbonatite complex in Sao Paulo State, Brazil first formed 131 Ma in the Cretaceous [247, 248, 249, 250]. Apatite samples from the Jacupiranga deposit have previously shown high enrichment with REE, with fluid inclusions within the minerals being of interest to research into the formation of carbonatite deposits [250]. The

apatite within Jacupiranga has previously been shown to be fluorapatite with F content between 2.21 and 0.62% and a REE enrichment of between 1000 and 3000 ppm [247, 250, 251]. Chemical and composition analysis of the sample was conducted using X-Ray fluorescence (ARL PERFORM'X Sequential X-Ray Fluorescence Spectrometer, Thermo Fisher) at Colorado School of Mines. Elemental compositional is given in table 5.3.

Compound	**Wt %**
P_2O_5	38
CaO	35.5

Table 5.3 Chemical analysis of apatite sample from Jacupiranga, Brazil. For chemical composition under 10% see appendix, table A.2.

5.4.2 Preparation

The apatite minerals were ground to 100% passing 80µm using steel ring mill (Angstrom Model TE250 Ring Pulverizer). This was the same methodology as used in section 5.2.2 on parisite.

5.4.3 Zeta potential measurements

The mineral samples were suspended in water or collector solution at 0.02 g per 40 ml and then agitated on a shaking table for 20 minutes before each measurement. Zeta potential measurements were conducted using the Microtrac Stabino Particle Charge Mapping surface chemistry device at Colorado School of Mines, U.S.A. Measurements were conducted from pH 3.5 to pH 11, with NaOH and HCl were used to adjust pH. This is the same zeta potential methodology described in section 5.2.3 on parisite. Previous studies have shown that Na ions reduce the value of zeta potential and IEP of apatite therefore the results may be lower than other studies [14].

5.5 Apatite results

5.5.1 Water conditions

Measurements were conducted from pH 3.5 to pH 11, and showed an IEP of apatite at pH 3.8 under water conditions, shown in figure 5.7.

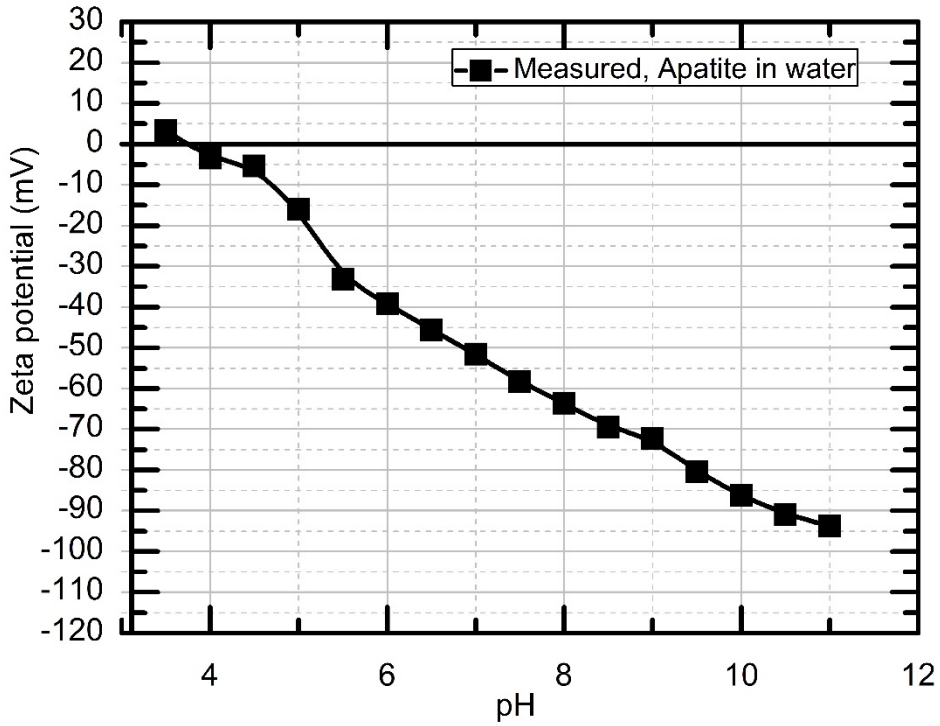

Figure 5.7 Measured surface charge (mV) of apatite in water as a function of pH.

The zeta potential results from figure 5.7 can be compared to results within the literature summarized in table 2.5 (chapter 2). The measured IEP of apatite agrees with the range of IEP values extracted from the literature with an IEP of 3.8, near the lower end of the range of pH 1 to pH 8.7. It must be noted that the majority of the studies had an IEP value of between pH 3 and pH 7 in which the IEP from this study fits well, particularly as the IEP is usually lowered under Na ions [93].

Five other studies from table 2.5 were selected to compare to the zeta potential measurements. Four were selected due to their high purity [97, 90, 89, 87] and Nduwa-Mushidi *et al.,* [85] was selected due to use of the same methodology

and equipment. These five studies are plotted in figure 5.8, which shows that there was a wide range of zeta potential values from apatite studies, although there are common characteristics of the zeta potential curves in which as higher pH values the zeta potential was negative and at lower pH values the zeta potential was positive. The IEP of studies plotted in figure 5.8 range from >2 to 8.7.

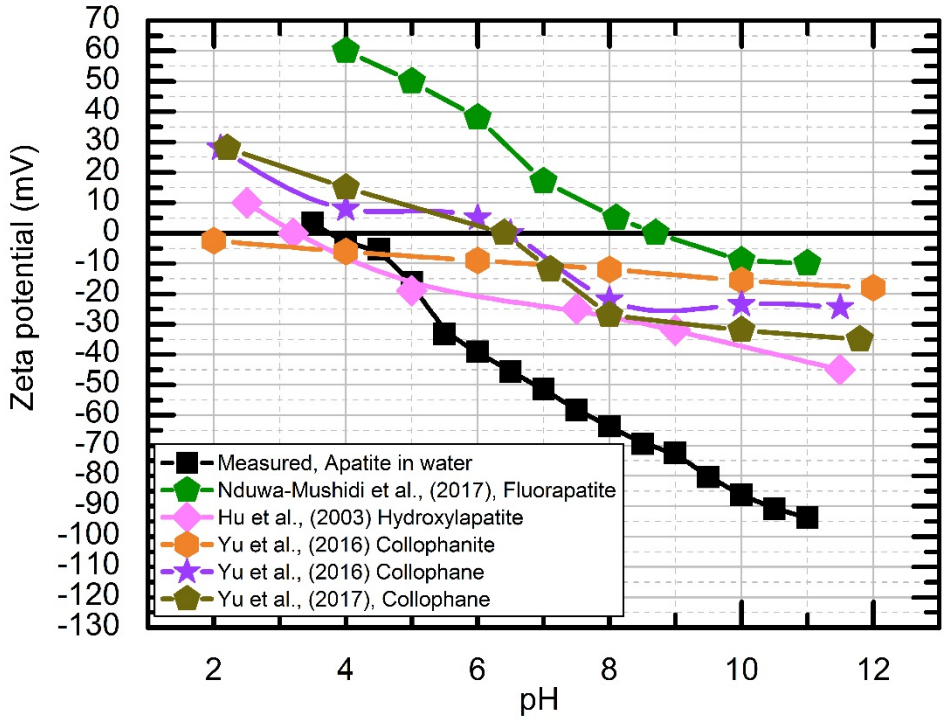

Figure 5.8 Comparison of zeta potential measurements of rare earth enriched apatite in water and literature values of zeta potentials of apatite. Curves are fitted for ease of eye and not to demonstrate data.

The surface behaviour of apatite enriched with REE has already been investigated, particularly into the effect of synthetically doping apatite with Eu [252]. However, there has been no comparison between the enrichment of natural REE apatite and synthetic REE enriched apatite. The four studies identified as investigating the zeta potential of apatite with REE enrichment are plotted in figure 5.9 [14, 93, 91, 252]. Of the four studies, one was synthetically produced hydroxyapatite [252] and the other three were natural apatite. The exact type of apatite (fluorapatite, chlorapatite, hydroxyapatite) is not identified within the papers. The enrichment within each apatite is slightly different with Chen *et al.,* [252] hydroxyapatite doped with 5% europium. Chen *et al.,* [252]

also investigated the doping of hydroxylapatite with between 1-10% of europium at pH 9, which showed little variation. This indicates that doping of between 1 and 10% of europium on apatite does not affect surface behaviour. The apatite studied in Zhou *et al.,* [91] was enriched with 0.77% cerium. Filippova *et al.,* [93] and Fillipov *et al.,* [14] both investigated apatite with enrichment of 2402ppm of cerium and 1102ppm of lanthanum. All the natural apatite in figure 5.9 were enriched with LREE. As LREE are the predominant REE in apatite deposits this is not unexpected.

Russia is unusual in containing apatite that is enriched with HREE [185]. In comparison to the zeta potential measurements of other apatite samples plotted in figure 5.8, apatite enriched by REE does not appear to have significantly different surface behaviour.

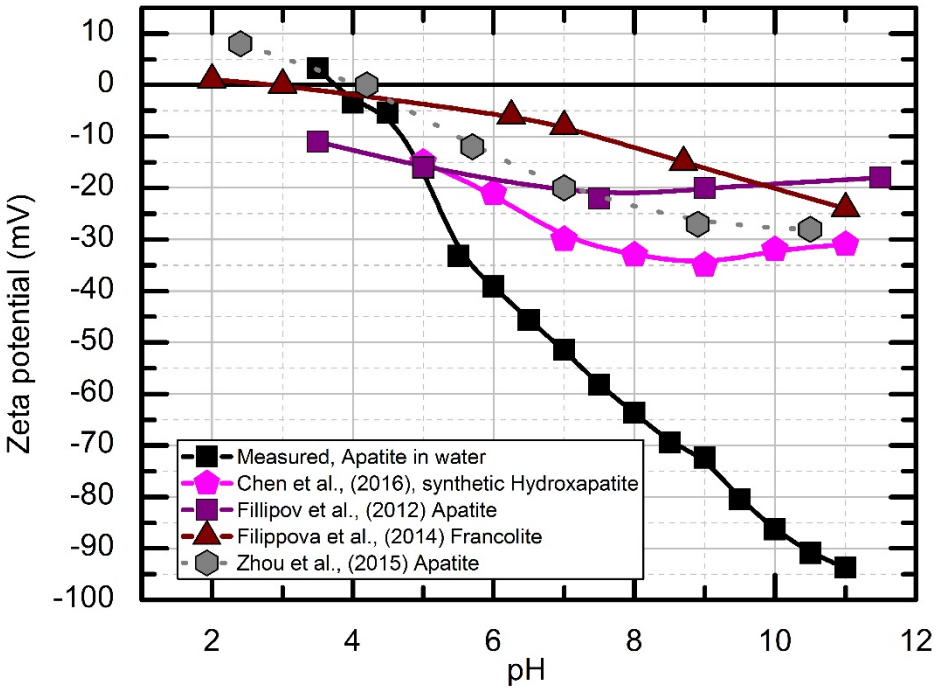

Figure 5.9 Measured surface charge of apatite as a function of pH compared to of zeta potential measurements of apatite identified within the literature as containing REE.

From studies into doping by synthetic apatite it can be demonstrated that small % (1-5%) of ions such as F, Cl, Ca and Si can significantly affect the zeta potential measurements of a mineral [253, 254, 255]. From reviewing the purity

of the natural apatite used in many of the mineral processing studies it becomes apparent that a large percentage contain contamination, with ions or increased concentrations of certain elements or do not specify the exact purity [12]. Although REE enrichment (up to 10%) does not appear from the studies reviewed here to have a significant effect on zeta potential values of apatite other ions do and this may be why there is such a large range in both IEP values and zeta potential curves. Recent work by Filippova *et al.,* [256] on calcite and fluorapatite has shown that impurities may be linked to the calcium dissolution and collector adsorption.

5.5.2 Collector conditions

In figure 5.10, measured zeta potentials of apatite under water and collector conditions are plotted as a function of pH. As mentioned in section 5.3.2, hydroxamic acid and fatty acids are both anionic collectors and therefore lower the surface charge. The surface charge of apatite was reduced by over 30mV, causing the IEP of apatite under both collectors to be <pH 3.5.

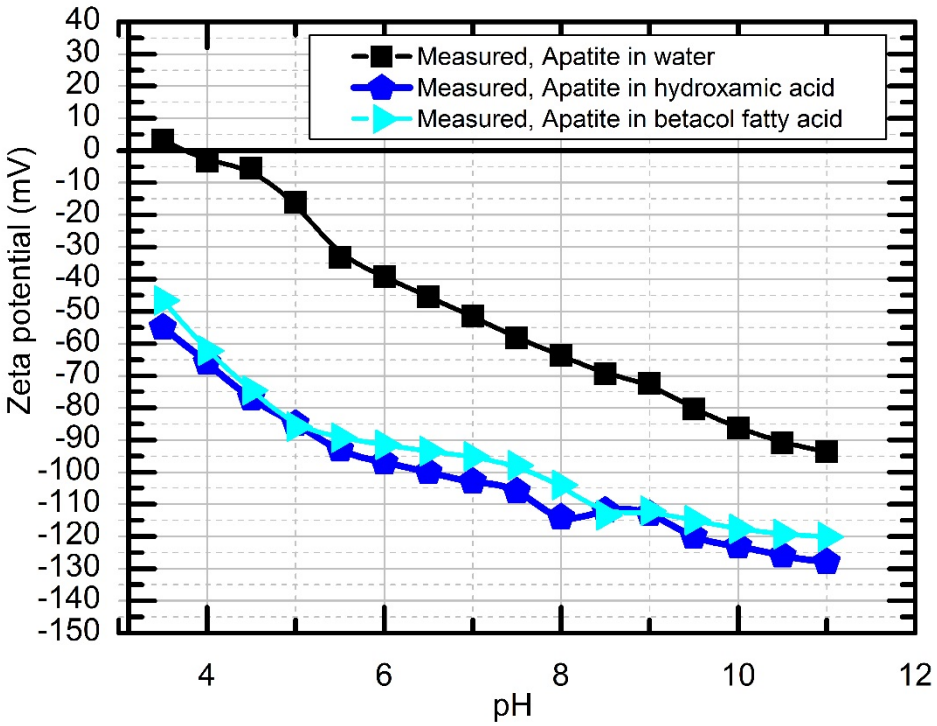

Figure 5.10 Measured surface charge (mV) of apatite under water, fatty acid and hydroxamic acid conditions as a function of pH.

To compare the zeta potential values of REE enriched apatite (figure 5.10), to non REE enriched apatite, the results of zeta potential investigations from Nduwa-Mushidi *et al.,* [85] were also extracted. Nduwa-Mushidi *et al.,* [85] was selected due to the use of the same methodology and equipment, these results are plotted on figure 5.11.

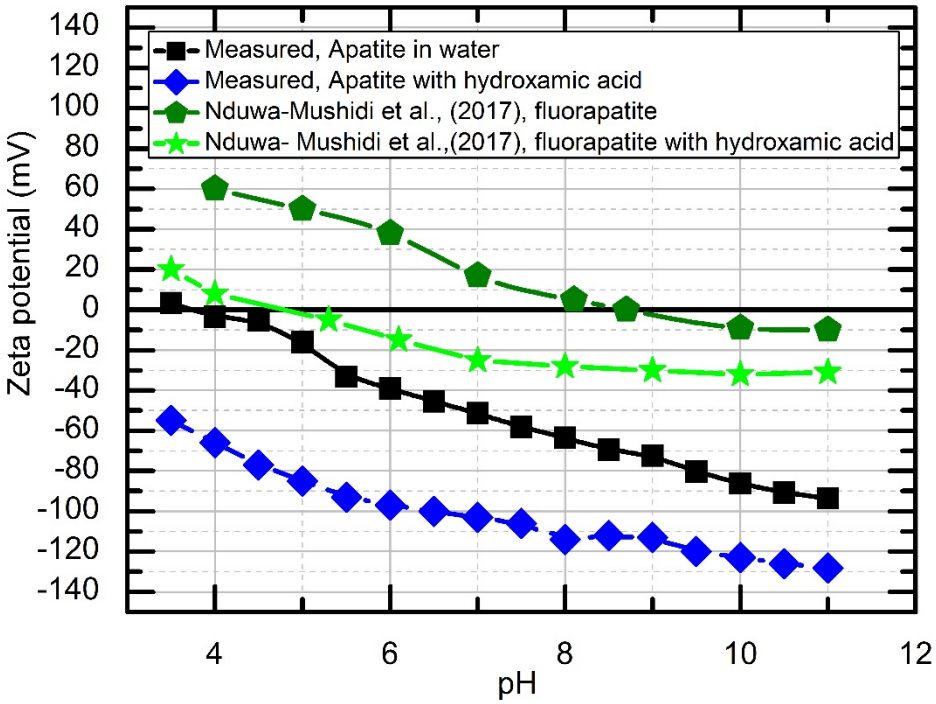

Figure 5.11 Comparison of measured surface charge of apatite under water and hydroxamic acid conditions as a function of pH with literature values from Nduwa-Mushidi et al., [85].

As shown in figure 5.11 all zeta potentials showed a negative zeta potential at a pH above 9, with the addition of hydroxamic acid in both this study and Nduwa-Mushidi *et al.,* [85] causing the zeta potential to reduce to a lower charge. Nduwa-Mushidi *et al.,* [85] showed a shift of IEP from pH 8.7 to around pH 4.8 with the addition of hydroxamic acid. In this study the IEP was shifted from 3.8 to <2. The magnitude of the shift between studies was of the order of magnitude expected as in previous studies some hydroxamic acids have a larger effect on

flotation than others. The mole per liter used was also different with this study using 5 x 10^{-4}M and Nduwa-Mushidi *et al.,* [85] using 10^{-3} M. The behaviour of apatite containing REE under hydroxamic collector is similar to apatite not containing REE, this may allow apatite containing REE to be processed the same way as its non-enriched counterparts.

As apatite is one of the most bountiful minerals on the planet and a wide range of deposits exist which contain REE bearing apatite, this is of future interest to REE sourcing [11, 1]. The results in figure 5.10 show that REE enriched apatite behaves similarly to non-enriched apatite, and is effected by hydroxamic acid and fatty acid in a similar way. Previous work by Filippova *et al.*, [93] of a REE enriched apatite under micro flotation showed a high recovery with sodium oleate, similar to non REE enriched apatite. As many deposits such as Hoidas Lake, Canada and Jaquia, Brazil contain REE enriched apatite [257, 258] the use of reagent regimes already well researched on apatite is very useful for mineral processing. Although apatite is most commonly enriched with LREE, which are less valuable than HREE some deposits, such as Songwe Hill, Malawi are enriched with HREE making mining more economically viable. These REE deposits could supply the future green technology.

5.6 Summary

In conclusion, zeta potential measurements of REE enriched apatite in water and collector conditions were made. The IEP of REE enriched apatite in water was measured at pH 3.8, in the middle of reported IEP values of apatite in the literature. Zeta potential measurements of the apatite were also conducted in a collector solution of hydroxamic acid and betacol fatty acid. The behaviour of REE enriched apatite under collector conditions is similar to other apatite. Thereby indicating that REE enrichment does not affect the surface behaviour of apatite under common rare earth collectors. This implies that flotation research into apatite could be applied to future mineral processing of REE enriched apatite. This is an important finding for further development of REE enriched apatite deposits, such as Songwe Hill in Malawi or Kovdor in Russia.

Zeta potentials measurements of parisite, the first of their kind, produced an iso electric point (IEP) of pH 5.6. This value is at the lower end of the IEP values of bastnäsite, which range from pH 4.6 to pH 9.3 in the literature. Under reagent collector conditions parisite behaves in a similar way to bastnäsite, with the value of zeta potential decreasing with increasing pH, and the IEP shifting to lower values compared to those obtained under water conditions. This similar behaviour extends to zeta potential values under supernatant conditions, where a decrease in zeta potential values with increasing pH was measured, compared to those obtained under water, as have previously been observed for bastnäsite. As zeta potential measurements in the presence of reagents and supernatants are the most rigorous way of determining the efficiency of a flotation reagent, the agreement between parisite zeta potentials obtained here and previous work on bastnäsite suggests that parisite may be processed using similar reagent schemes to bastnäsite. As many REE fluorcarbonate deposits, particularly those containing synchysite and parisite are already processed in a similar way to bastnäsite, this research validates this approach. This is important for future processing of REE deposits, comprising of more complex REE mineralogy. The surface behaviour of rare earth fluorcarbonates, in particular synchysite will be further explored in chapter 6.

Chapter 6
Nanobubbles on mineral surfaces

6.1 Overview

Surface nanobubbles have a range of interesting properties, such as their incredibly long lifetimes and small contact angles. They are of wide interest to a number of research fields, ranging from mineral processing to microfluidics. In mineral processing, they have been used to provide a clear indication of the hydrophobicity at the surface of a mineral, which is important for froth flotation. Previous work has focused on complex ores containing minerals such as eudialyte and chalcopyrite. Nanobubbles formation on hydrophobic surfaces has long been confirmed, but the factors controlling their size and location are less well understood. Identifying these factors is vital to enable nanobubbles to be successful implemented in industrial applications, such as large scale froth flotation.

This chapter investigates, using non-contact atomic force microscopy, the properties of surface nanobubbles on the minerals dolomite and synchysite under reagent conditions favourable for froth flotation. Dolomite is a common carbonate mineral, which is commercially mined in a wide number of deposits and is particularly important in processing carbonate rare earth element deposits. Synchysite is a rare earth fluorcarbonate mineral, which is of future interest in sourcing rare earth elements. The background and sourcing of the mineral samples is covered in section 6.2. Atomic force microscopy is the most common method for imaging nanobubbles at the surface of materials, as it produces both high resolution images and enables the identification of the nanobubbles contact angle and lateral length. The experimental setup of the atomic force microscope and liquid cell to measure nanobubbles is discussed in section 6.3. Analysis of the nanobubbles is covered in section 6.4. The bubble density of the nanobubbles detected is described in section 6.5. The contact angle of the nanobubbles and the oversaturation of the surrounding liquid is examined in section 6.6. Section

6.7 discusses the links between macroscopic studies and the nanobubble populations measured. Finally, section 6.8 summarizes chapter 6.

6.2 Mineral samples

6.2.1 Dolomite

The carbonate mineral dolomite ($CaMg(CO_3)_2$) was selected for investigation as it is a common gangue (waste) mineral, it is also associated with many carbonate rare earth element deposits [1]. Two of the largest rare earth mines, Mountain Pass in California and Bayan Obo in China contain dolomite as a major gangue mineral. The surface properties of dolomite have also been well studied with investigations into its surface behaviour under common collectors [62, 259]. Thereby allowing the nanobubble formation to be linked with macro scale hydrophobicity and flotation experiments. The dolomite used in this work was supplied by Edgar Schach and Martin Rudolph (Helmholtz Institute of Resource Technology).

The dolomite sample was analysed using x-ray diffraction and its composition confirmed with reference to the RTUFF database [192]. The sample was found to be very pure with a purity of 87.5%. The dolomite sample was set in epoxy resin then machine polished to ensure a smooth surface for non-contact- atomic force microscopy imaging.

6.2.2 Synchysite

Synchysite was selected due to previous research in chapter 2 and chapter 5 on the surface behaviour of fluorcarbonates. As these minerals are relatively unstudied understanding the hydrophobicity and flotation performance of synchysite is of great interest.

Synchysite- (Ce) ($CaCe(CO_3)_2$ F) is a rare earth fluorcarbonate mineral which contains over 30% rare earth elements [9]. Although not as prominent as its fluorcarbonate sibling bastnäsite, which currently supplies over 45% of the world's REE, synchysite is still economically important in a number of deposits [233, 234, 244]. It is also important as a secondary ore mineral to deposits such as Bear Lodge, Wyoming and Nechalacho, Canada [195, 260]. Understanding the effect of reagents on the surface properties of synchysite is important for optimum processing of these deposits.

The ore containing synchysite from Songwe Hill, Malawi was provided by Mkango Resources Ltd. Songwe Hill is a carbonatite deposit within the Chilwa Alkaline Province, the main ore minerals are apatite and synchysite with the main gangue minerals being ankerite and calcite. For more details of the Songwe Hill deposit geology see Al Ali [9], Broom-Fendley *et al.,* [185] and Broom-Fendley *et al.,* [261]. The mineralogy of the sample was analysed on particles in a polished epoxy resin grain mount using Mineral Liberation Analysis (MLA) software and the SEM microscope (FEI Quanta 650 MLA-FEG machine) in combination with X-Ray spectroscopy detectors (Bruker Quantax X-Flash 5030 EDS-Detectors) in Freiberg, Germany, similar to Bachmann *et al.,* [262]. In figure 6.1, the mineral composition of samples from Songwe Hill, Malawi is shown, where different colours represent different mineral species. Note that the composition is not representative of the ore geology shown at Songwe Hill, please see QEMSCAN results in Al Ali [9] for more details. However, the X- Ray spectra and MLA processed images enabled the identification of the synchysite mineral investigation area within the ore sample. Raman spectroscopy was used to navigate to the location of the synchysite mineralisation. One ore section was chosen, highlighted in red, to undertake measurements of synchysite

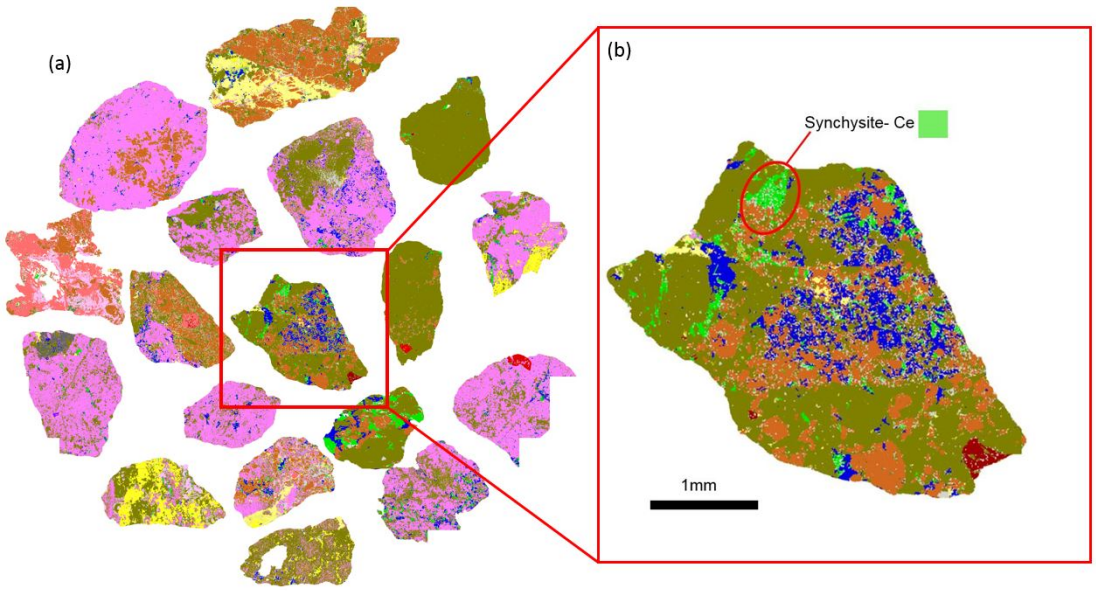

Figure 6.1(a) Mineral Liberation analysis of Songwe Hill ore, light green shows synchysite, dark green is the carbonate mineral ankerite with calcite in bright pink (b) Magnified area investigated in NC-AFM images. The sample area is highlighted in red.

6.3. Experimental Setup

6.3.1 Liquid cell

Fatty acids and hydroxamate collectors were selected due to their use in rare earth flowsheets, such as the Mountain Pass bastnäsite mine in California and the Nachalacho REE deposit in Canada [75, 245]. The chemical bonding between hydroxamic acids and bastnäsite and dolomite has also been explored by Espiritu *et al.,* [7] and Espiritu *et al.,* [259]. From the results of chapter 5, synchysite and bastnäsite are expected to behave similarly under these collectors. Common depressants were also used to determine the effect of collectors on nanobubbles at the surface of dolomite. The composition and name of the depressants is subject to non-disclosure.

For non-contact- atomic force microscopy measurements on dolomite, water with KCl 10^{-3}mol/L background electrolyte and a collector solution (of combined fatty acids (betacol) and hydroxamates (AM810) in usual proportions for

flotation) were prepared before measurements and cooled to 5^{o} C. This methodology was repeated with the water solution and depressant solution (combination of depressants from mineral processing). The synchysite sample was measured using the same methodology.

The liquid cell of the atomic force microscopy was filled by injecting up to 750µl of collector, reagent, water or depressant solution using a clean disposable plastic nozzle attached to a pipette. Although plastic contamination has been found in nanobubble research [133, 263], this study used the same equipment and methodology as Babel *and* Rudolph [15]. Babel *and* Rudolph [15], investigated the force curves of nanobubbles showing the nanobubbles to contain gas not plastic.

The liquid was then heated to between 20^{o}C and 30^{o}C for nanobubble measurements on dolomite in a temperature controlled room of 21^{o}C ±1^{o}C. For the synchysite measurement the liquid was heated to between 30^{o}C and 40 ^{o}C under the same temperature controlled conditions. Between measurements the mineral surface was polished with diamond suspension [DiaPro $\frac{1}{4}$ µm Struers] to provide a fresh surface for each experiment. Subsequently, the surface was thoroughly washed with water, ethanol and distilled water again.

6.3.2 Atomic force microscopy

Non-contact atomic force microscopy (NC-AFM) of the sample of dolomite resulted in five good resolution images, two images in water, two images in collector solution and one image in depressant solution. The measurements of the polished cross section containing synchysite resulted in one good image under a mixed reagent regime.

The original NC-AFM image of synchysite mineral sample had a large range of phase and topography so a smaller area was selected, 5 µm x 6µm, to enable identification of nanobubbles, see figure 6.2.

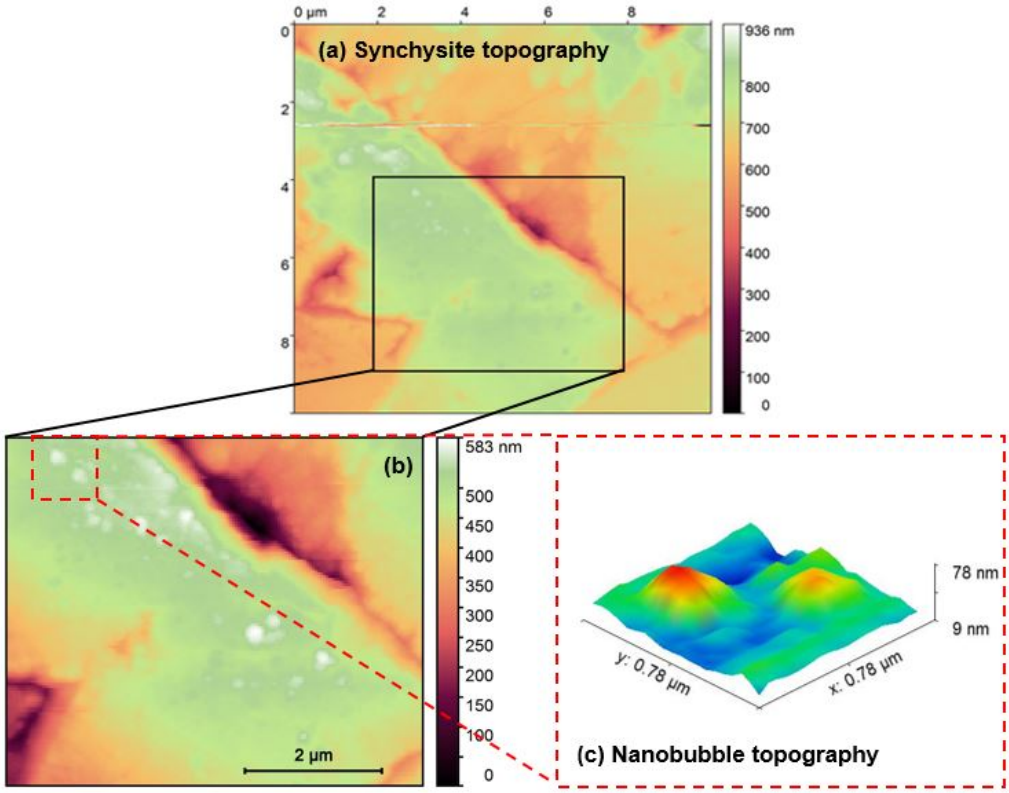

Figure 6.2. (a) Non-contact atomic force microscopy of synchysite topography (b) magnified section of synchysite topography (c) magnified section of b, showing two possible nanobubbles.

In figure 6.2, the NC-AFM analysis of a high resolution area of 6 µm x 5µm is shown. As can be clearly seen in figure 6.2 (d) there are several small circular areas which are much higher than the surrounding topography.

In both the dolomite and synchysite images, circular areas of higher topography, over 8nm, were identified as potential nanobubbles by comparing with changes in phase and finally fitting the potential nanobubbles to cross sections. The areas of high topography were also selected to link with changes in phase diagram, as the phase diagram should clearly show changes in surface stiffness and the adhesion between tip and surface in the presence of nanobubbles. The selection and analysis of nanobubbles is covered in more detail in section 6.4.

6.4. Analysis of nanobubbles

6.4.1 Phase and Topography comparison

Analysis of topography and phase in the NC- AFM images of dolomite was conducted by lining up specific areas of the phase and topography image against each other, see figure 6.3.

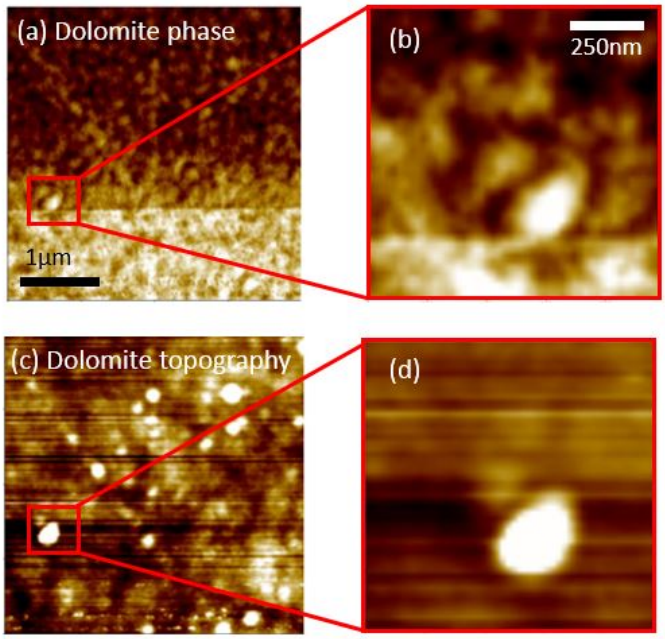

Figure 6.3 Topography and phase diagrams of dolomite nanobubbles in collector solution. a) and b) are phase diagrams for nanobubbles in collector conditions, with b) being an enlargement of image a). c) and d) are topographical images over the same area as a) and b) respectively.

When the nanobubble showed in both the topography and the phase on the dolomite sample it was accepted for further analysis, otherwise it was discounted. Of the 30 nanobubbles identified on the collector images, 9 were deselected using a combination of phase and spherical fitting. On the water images, 16 were deselected out of 27.

In the synchysite image the extreme topography of the mineral grain caused the phase to be difficult to interpret due to the phase ranging from 0 to 83 degrees.

Previous studies such as Rangharajan *et al.,* [264] have shown phase differences between areas of bubbles and non-bubbles of 8 degrees, the phase difference in the images analysed in this study is often over 50 degrees. The area of phase and topography was magnified, which show indications of nanobubbles presence, figure 6.4.

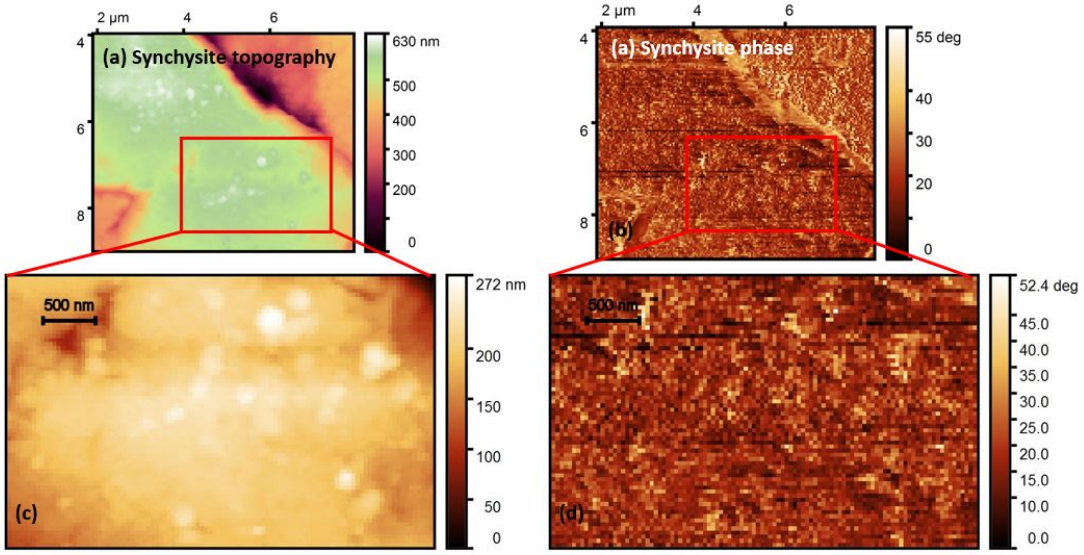

Figure 6.4 (a) Topography on synchysite mineral and (b) phase on synchysite mineral over section with nanobubbles (c) magnified topography, (d) magnified phase.

The topography and phase of every possible nanobubble on the synchysite is shown in figure 6.5.

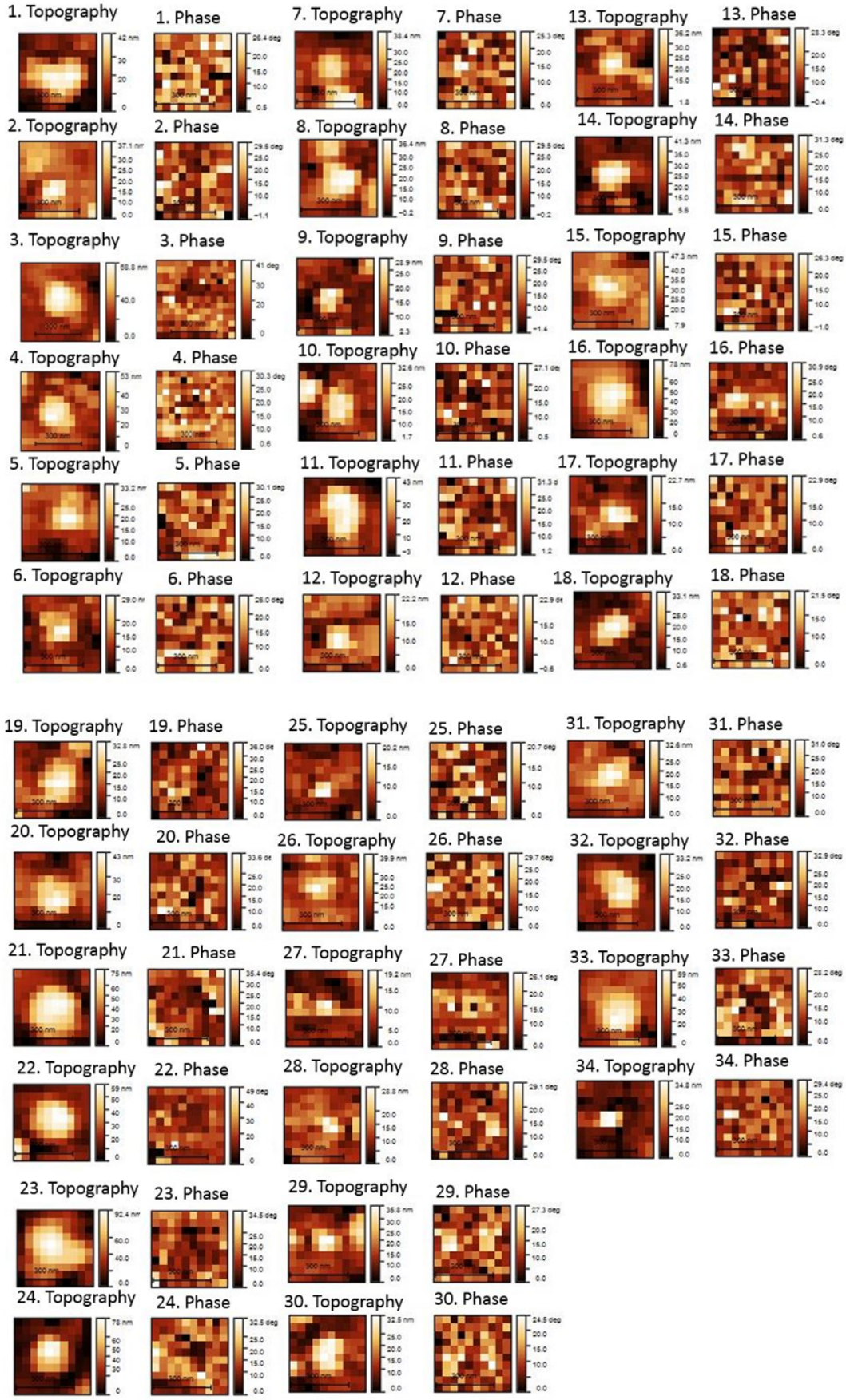

Figure 6.5 Topography and phase non-contact atomic force microscopy images from synchysite.

In comparison we show phase and topography on areas of the graph without changes in topography, see figure 6.6.

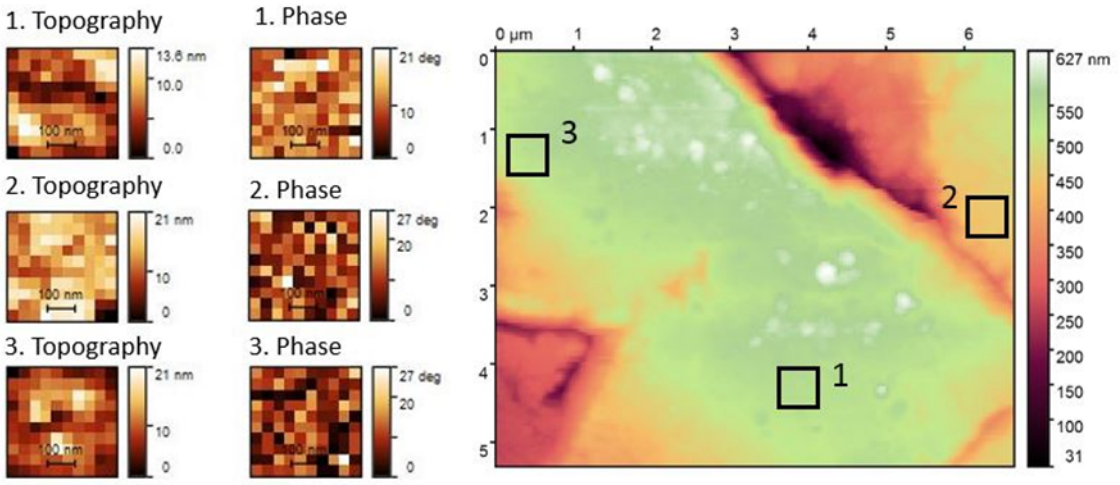

Figure 6.6 Comparison of three areas of phase and topography without nanobubbles.

Although visually there were indications of nanobubbles, a quantified methodology was conducted. The image analysis software, ImageJ was used to evaluate the images. ImageJ is regularly used in biology from research ranging from cancer in mice [265] to human intestinal cells, at the time of writing, (2019) the original ImageJ paper has over 19,000 citation of investigations that have used its analysis. ImageJ was used to compare the average value of the pixels within a set circle defined by the topography compared to the overall average of the selected nanobubble surrounding area [266].

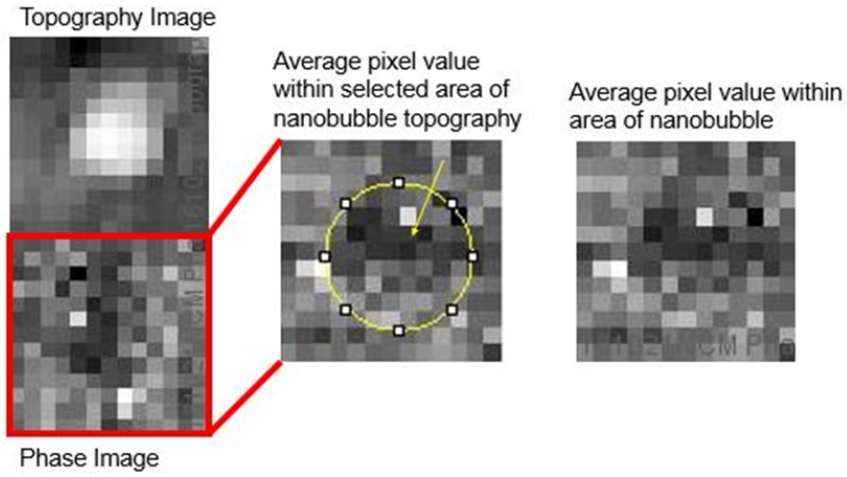

Figure 6.7 Phase and topography image compared and the selected area for pixel averaging.

However when plotted the standard deviation of the background noise was too great to make this an effective technique, see figure 6.8.

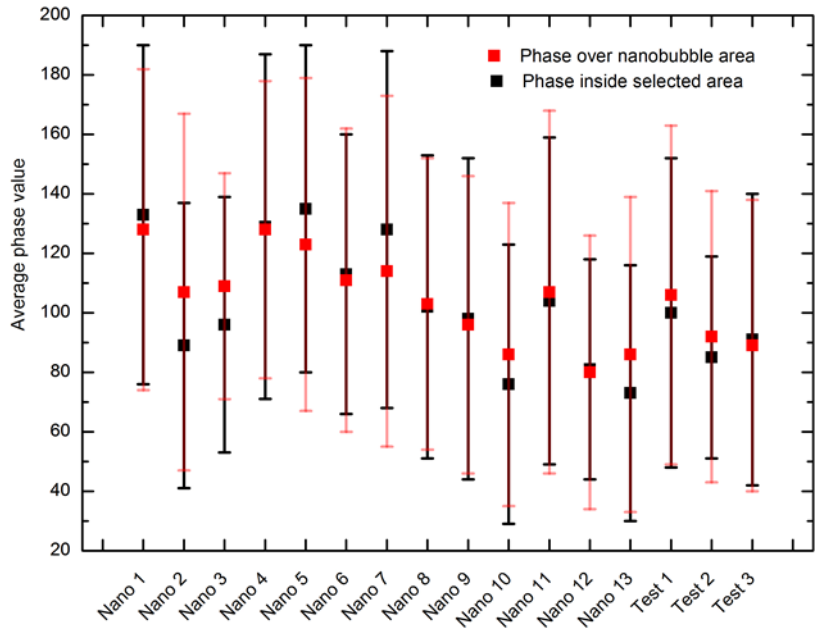

Figure 6.8 Average phase value of pixels around the nanobubble and within a set circle of synchysite nanobubbles with standard deviation values as errors. Test 1,2,3 are of the sections highlighted in figure 6.6 where there was no nanobubble topography.

ImageJ was unable to differentiate differences within experimental variables on the synchysite nanobubbles. We would expect systematic differences within the

phase between inside the nanobubble and outside in the selected area. We believe processing effects are to fault rather than no difference in the data as differences can be seen optically.

Due to the range of phase values and the indication of the nanobubbles presence all synchysite images were analysed using cross sections fitting.

6.4.2. Cross section fitting

The cross sectional fits were fitted following methodology followed work by Rangharajan *et al.,* [264] and Li *et al.,* [267], using the spherical cap model proposed by Lohse *and* Zhang [112]. Cross sections were fitted across four angles of the nanobubble. Figure 6.9 shows an example for the selection with regression coefficient $R_{ec}^{\ 2}$ fitting over a 0.8 for all four cross sections. If two of the cross sections had a $R_{ec}^{\ 2} < 0.8$ then the nanobubble was discounted. Nanobubbles below 8nm in all four cross sections were also discounted, these are highlighted on figure 6.9 in black.

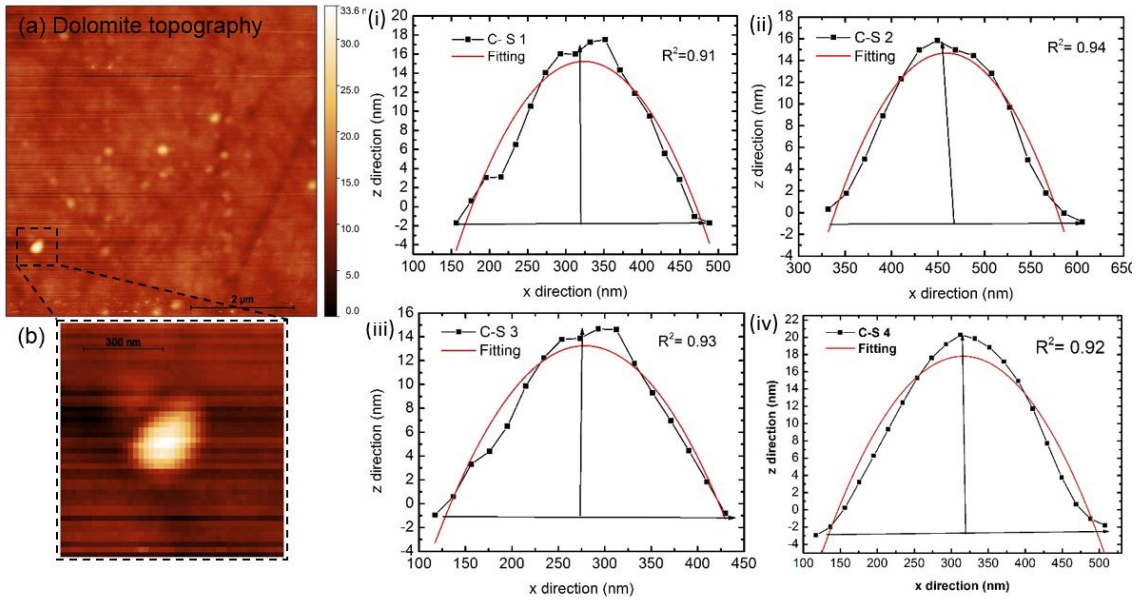

Figure 6.9 Nanobubble selection using cross sections. (a) Nanobubbles on the surface of dolomite 4µm x 4µm, nanobubbles circled and numbered in red (b) enlarged section with nanobubble investigated in cross sections i, ii, iii, iv. The regression coefficient (R_{ec} ^{2}) values of i, ii, iii, iv cross sections are shown below the figure.

Nanobubbles were fitted to a spherical cap using Origin 8.6 Data Analysis graphing software using non-linear curve fit. This was fit following the spherical cap model outlined in chapter 3, described by equation 3.5

$$R = \frac{(L^2 + 4H^2)}{8H} = \frac{L}{2\sin(\theta)} \qquad [3.5]$$

(Where *R* is the radius of circle, *L* is length of nanobubble, *H* is the nanobubble height and *θ* is the contact angle of the nanobubble).

The fitting started with 3 initial parameters (co-ordinates of the center of circle and radius) with y the dependent variable and z the independent variable.
From selecting areas of higher topography over 8nm, fitting with spherical cap and comparing with the phase, 32 nanobubbles were identified from 63 possible candidates on dolomite. The extracted nanobubble height ranged from, 73.9nm to 7.8nm, which compares to the value of 1.4nm obtained for the root mean square (RMS) of the surface roughness of the dolomite surface.

25 nanobubbles were selected out a possible 35 nanobubble candidates on the synchysite .The nanobubbles ranged in height from 71.9nm to 14.6nm, with their heights being much greater than the root mean square surface roughness (RMS) measured on this sample of synchysite of 1.9nm.

6.5. Bubble density of surface nanobubbles

Bubble density on dolomite was calculated by dividing the number of bubbles by surface area, and under collector conditions the nanobubble density on dolomite was 0.656 per μm^2. In contrast the nanobubbles in water conditions on dolomite had a bubble density of 0.342 nanobubbles per μm^2, with depressants much lower at 0.0625 nanobubbles per μm^2. The bubble density differences of dolomite are shown in figure 6.10.

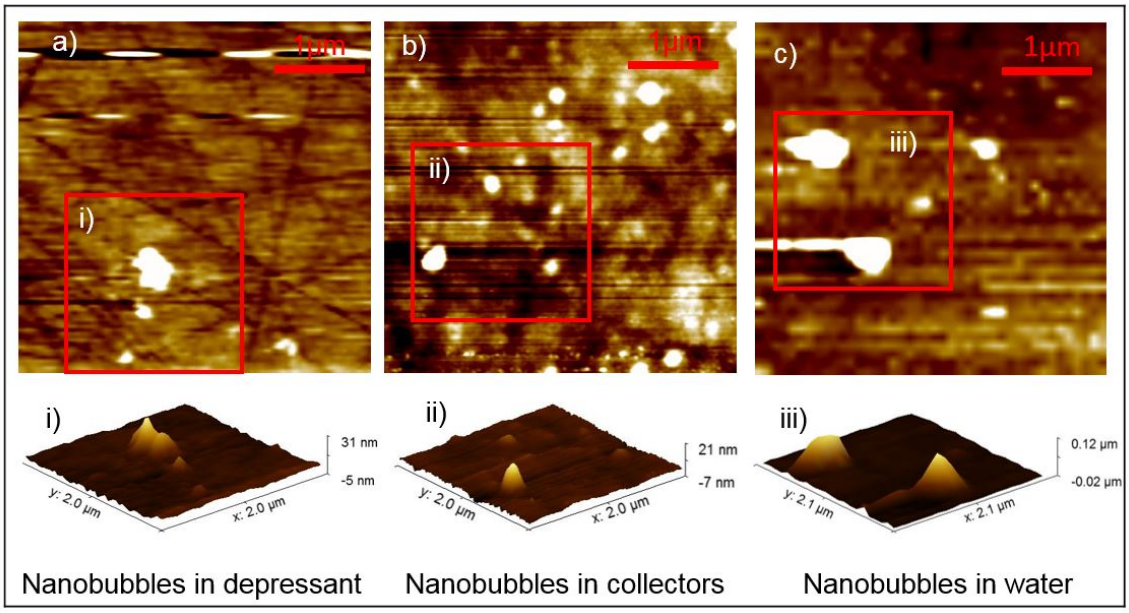

Figure 6.10 Nanobubble density differences of dolomite with topographical AFM images of nanobubbles in depressant (a) collectors (b) and water (c). Each image is 4 µm x 4 µm across.

As the synchysite nanobubbles were identified in only one image, from a magnified section, bubble density was not calculated.

6.6. Contact angle and oversaturation of surface nanobubbles.

Cantilever tips have long been known as an area of error for the width measurement of a nanobubble. This is due to the cantilever distorting the shape of the nanobubble with the force of imaging the surface, see figure 6.11.

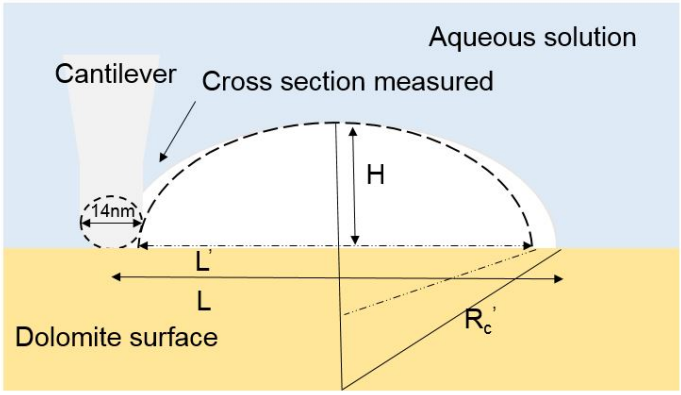

Figure 6.11 adapted from Wang et al., [125] schematic of interaction between nanobubble and cantilever tip.

Equations for the correction of nanobubble radius, diameter (*L*) and contact angle (θ) were taken from Wang *et al.,* [125], equations 6.1-6.3.

$$R_c{}' = \frac{(D)^2 + 4H^2}{8H} - R_{tip} \qquad [6.1]$$

$$L' = \sqrt{L^2 - 8HR_{tip}} \qquad [6.2]$$

$$\theta' = 2\arctan\left(\frac{2H}{L'}\right) \qquad [6.3]$$

Where $R_c{}'$ is the corrected radius, L' is the corrected length (diameter) of the nanobubble and θ' is the corrected contact angle.

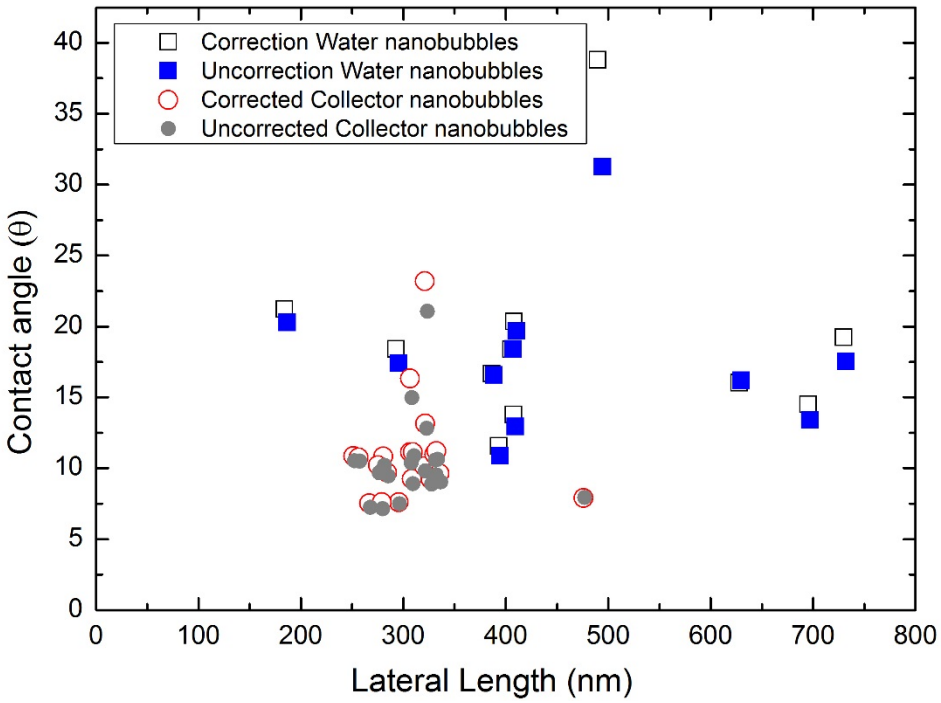

Figure 6.12 Width of nanobubbles against contact angle of both water and collector nanobubbles in corrected and uncorrected form.

Figure 6.12 shows that the cantilever tip correction does not have a significant effect on the width and contact angles of the nanobubbles. In this study, a cantilever with a tip radius of 7nm was used [268, 269], and correction of the contact angle was calculated following methodology from Wang *et al.,* [125].

When tip correction was applied the nanobubbles on dolomite in the collector reagent scheme had an average contact angle of 9.4 ^{0} with standard deviation ±3, whereas those in water conditions had an average contact angle of 15^{o} with standard deviation of ±9^{o}, as plotted in box and whisker format in figure 6.12. The collector contact angle was the average of 21 nanobubble contact angles with the water being an average of 11 nanobubble values. These values are plotted in figure 6.13.

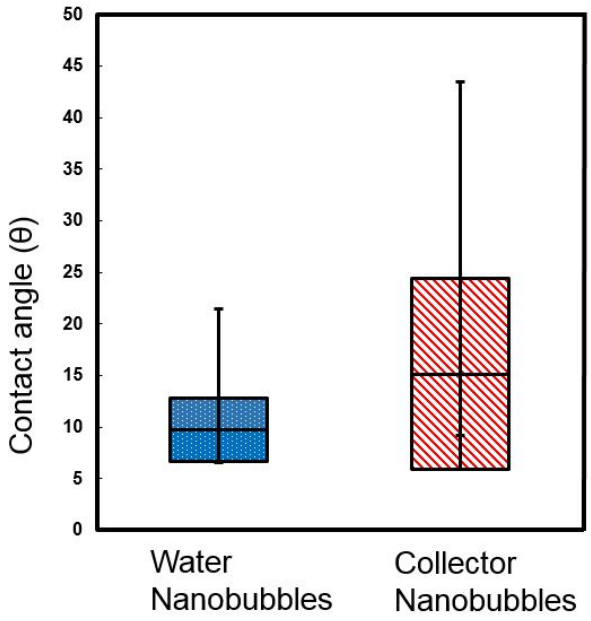

Figure 6.13 box and whisker plot of contact angles of surface nanobubbles on dolomite under collector and DI water conditions (the data was selected using fitting of a spherical cap model after Lohse and Zhang [2015]).

The average contact angle of the nanobubbles measured on synchysite was 24 degrees ± 8 standard deviation. The large standard deviation in contact angle values could be due to variation in line pinning highlighted by Ditscherlein *et al.,* [155] during their investigation of nanobubbles on rough alumina. The average contact angle of 24^0 was higher than on the mineral dolomite under both collectors and water conditions. When using the typical cross sections provided by Mikhlin *et al.,* [163], the surface nanobubble contact angle on galena was 4 (10mM collector) and 9 degrees (0.1mM collector), also below the values of the synchysite nanobubbles. However, previous research on the silicate mineral mica has found a wide range of contact angles between 30 and 60 degrees, demonstrating that the synchysite and dolomite contact angles are not unusually high [17, 23]. The surface roughness of the synchysite was also greater than the dolomite, RMS of 1.9 nm compared to a RMS of 1.4nm. Studies by Agrawal *et al.,* [27], and Wang *et al.,* [26], have demonstrated that physical patterning, and therefore surface roughness, can affect the location and size of nanobubbles at a surface. This subject of surface patterning and its effect on nanobubbles is further explored in chapter 7.

6.7. Discussion

Nanobubbles long lifetimes are caused by the oversaturation of the liquid around the nanobubble, surface hydrophobicity and the pinning of the nanobubbles on the three phase contact line [24, 112]. With a (a fixed) gas oversaturation within the liquid ζ > 0, there exists a stable equilibrium defined by;

$$\sin(\theta) = \xi \frac{P_o L}{4\sigma} = \xi \frac{L}{L_c} \qquad [3.11]$$

(θ is the contact angle*, L* the lateral length, and L_c the critical lateral extension *(L_c=4σ/P_0* $\approx 2.84\mu m$ [14]*),* *σ* is the surface tension and P_0 the ambient pressure*).*The origin and derivation of this equation is described in more detail in chapter 3, section 3.2.

This equilibrium equation can be used to calculate the oversaturation of the liquid. However, as many AFM systems, such as the one used in this study, are open to the surrounding atmosphere therefore values of saturation must be treated with caution.

Although reagents such as fatty acids have been shown to effect surface tension in macroscopic bubbles, the contact angle and therefore surface tension of nanobubbles does not necessarily appear to be effected by reagents [19, 270].

In figure 6.14, the sine of the contact angle of both synchysite and dolomite nanobubbles is plotted as a function of the nanobubble length under both water and collector conditions. In both cases sin (θ) shows an approximately linear dependence on the length (the straight lines shown are linear fits to the data), consistent with equation 4. Values of the ratio of ξ/L_c of 0.6 μm^{-1} and 0.5 μm^{-1}, for nanobubbles in water and collector respectively, were extracted from gradient (equation 3.11) of the linear fits shown. Wang *et al.,* [125], obtained a value of ξ/L_c of 2.9 μm^{-1}, for nanobubbles induced in nanopits, which coupled with a value of L_c of 2.84 m, led to an estimated oversaturation ξ of 8.2. Taking the same value

of L_c, the gradient leads to an estimated oversaturation ξ of 1.7 under water conditions. The value of oversaturation obtained in this work therefore seems reasonable given the different methodologies in which nanobubbles were induced in these studies. Using the same methodology on the nanobubbles on synchysite produces a gradient of 1.45μm^{-1}, and therefore an oversaturation of 4.1. A higher oversaturation is expected as the liquid surrounding synchysite was heated to between 30^0 C and 40^0 C rather than 20^0 C to 30^0 C on dolomite.

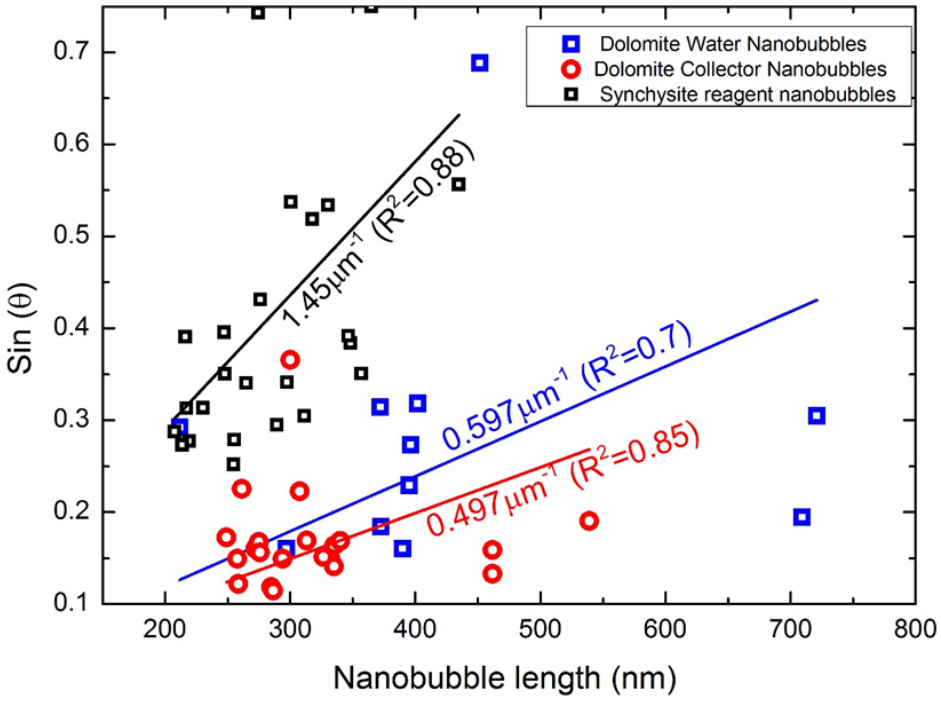

Figure 6.14 sine of the contact angle of dolomite and synchysite surface nanobubbles as a function of the lateral length under water and collector conditions.

In addition, there is no significant difference between the values of ξ/L_c obtained under water and collector conditions. Assuming that the over-saturation and the ambient pressure were the same in both cases, this also implies that the surface tension was not affected by the collector. This is consistent with the thin film model of nanobubbles developed by Zhang *et al.,* [19, 271]. However, the difference in the density of bubbles observed under water and collector conditions suggests that the collector has affected the pinning of the bubbles, which in turn determines the lateral length. Previous work by Xiao *et al.,* [272] investigating the

stability of nanobubbles under surfactants has shown with molecular dynamics simulations that the contact angle does not depend on pinning, whereas the density of nanobubbles does [272]. This is consistent with earlier results by Mikhlin *et al.,* [163] who investigated nanobubbles at the surface of the sulphide mineral galena (PbS) and found that the number of nanobubbles increased after the surface had been pre-treated using a xanthate collector rather than with water.

Tan *et al.,* [114] investigated the exact value of the pinning force by using an AFM tip to deform nanobubbles whilst imaging the mechanical response using total internal reflection fluorescence microscopy (TIRFM). The pinning strength varied between 5mN/m to 20mN/m, with the variation attributed to chemical and physical heterogeneities of the surface. The relative smoothness of the mineral surface in this case indicates that it is chemical heterogeneities induced by the collector that affects the bubble pinning. Previous work by Xie *et al.,* [113] has shown non uniform adsorption of xanthate on sphalerite caused differing regions of hydrophobicity on the mineral surface.

6.7.1 Dolomite studies

The increase in the observed number of nanobubbles under collector conditions in dolomite is also consistent with macroscopic studies investigating micro flotation for minerals processing. Both Espiritu *and* Waters [259] and Azizi *and* Larachi [62] investigated micro flotation of dolomite under collector (hydroxamic acid and fatty acid. In Azizi *and* Larachi [62], 75.3% of dolomite was recovered (floated) with hydroxamic collector compared to 4.1% of dolomite was floated (recovered) under water conditions. Surface nanobubbles could therefore be playing an important part in froth flotation, although much work is required to quantify the significance of this contribution. Future work may focus on more minerals and reagent regimes, linking micro- flotation experiments to further nanobubble systems.

6.7.2 Synchysite studies

The large number of nanobubbles at the synchysite surface indicate that the surface was highly hydrophobic. Recent studies of bastnäsite have shown it has similar surface behaviour under flotation conditions to synchysite [57]. The crystal system and calcium content of bastnäsite is different to synchysite, hexagonal with no calcium compared to monoclinic with 12% calcium [37, 40, 41]. However, similar surface behaviour is not unexpected as both synchysite and bastnäsite are rare earth fluorcarbonates with significant rare earth element concentrations, 33-43% and 63-52% respectively [273]. Flotation investigations of bastnäsite ores have shown high recovery from bastnäsite with collectors such as hydroxamates and fatty acids [6]. Recent research into bastnäsite surface behaviour using zeta potential measurements and Fourier- transform infrared spectroscopy (FTIR) has found that hydroxamates bonding is heavily influenced by the metal cation on the mineral surface which chelates with the hydroxamic acid [7, 243]. When using 330mg/L benzohydroxamic acid, the recovery of dolomite in micro-flotation tests was found to recovery of around 20%, whereas recovery of bastnäsite climbed to 70% [7]. As synchysite behaves similarly to bastnäsite, it would not be unexpected that hydrophobicity and therefore recovery of synchysite would be high under similar collectors (chapter 5).

Finally, these results provide the expansion of an analytical method to measure the hydrophobicity of the surface of a mineral using nanobubbles [15, 16, 120]. This methodology would be particularly applicable in ores that are highly complex with small grain sizes where micro-flotation or conventional contact angles are not feasible. Future work on rare earth fluorcarbonates should focus on producing samples less prone to splintering, either through different cleaning techniques or through the production of synthetic samples. This would enable the calculation of synchysite nanobubble density under set conditions. These results also provide some insight into synchysite surface behaviour, a highly unstudied mineral building on previous work on other rare earth fluorcarbonates in chapter 5.

6.8. Summary

In this chapter, the first images of nanobubbles on the minerals dolomite and synchysite were presented. Surface nanobubbles on dolomite, induced using the air water supersaturation method, were imaged using non-contact- atomic force microscopy under water, collector and depressant surfactant conditions. The observed bubble density was highest under collector conditions, with 0.656 bubbles per μm^2, compared to 0.342 nanobubbles per μm^2 under water conditions. Analysis of the bubble contact angles, which were extracted by fitting a spherical cap to the nanobubbles, suggests that the collector does not affect the surface tension, but does affect their pinning. This is consistent with both the observed bubble density, but also with macroscopic flotation studies. These results are the first nanobubbles imaged on the surface of dolomite and only the fifth study of nanobubbles on mineral surfaces. Previous studies have only confirmed the existence of nanobubbles on minerals and have not looked into the bubbles contact angle or density. As dolomite is commonly used in processing fields, this research opens up future development in linking nanobubbles with flotation.

Synchysite is a rare earth fluorcarbonate mineral, which is economically important in a broad selection of deposits, located in countries ranging from Malawi to India. Relatively little research has been conducted on synchysite, with only a few papers on its surface behaviour and flotation. Nanobubbles were found on synchysite under reagent conditions expected to induce hydrophobicity in rare earth minerals, which is required for efficient processing. Nanobubbles were selected using the same methodology as the dolomite surface nanobubbles, with the average contact angle of the nanobubbles on synchysite was 24 degrees ± 8. These are in line with contact angles found on mica and galena by previous studies. The presence of nanobubbles on synchysite under these reagents, demonstrated the hydrophobicity of the surface under flotation conditions. This work into synchysite builds on work into the surface behaviour of rare earth fluorcarbonates conducted in chapter 5. Chapter 7 continues on the theme of nanobubbles, investigating the effect of pinning first investigated in this chapter.

Chapter 7
Nanobubbles on patterned graphene

7.1 Overview

As detailed in chapter 3 and 6, nanobubbles are tiny domains of gas at the surface of hydrophobic materials [17, 108]. They have unusually long lifetimes and very small contact angles compared to their macroscopic siblings [18, 22]. Nanobubbles have been identified as a possible tool in improving froth flotation and understanding the surface hydrophobicity's of complex ore systems [15, 20]. The use of nanobubbles in flotation and on mineral's hydrophobicity was explored in chapter 6. Nanobubbles have also been identified as being linked to the causes of decompression sickness and a possible tool for cancer treatment [104, 105].

The small contact angle and long lifetime of nanobubbles are due to pinning along the three phase contact line and gas oversaturation within the liquid [24, 112]. However, the factors controlling the pinning and gas oversaturation are still not fully understood. Although nanobubble pinning is affected by physical and chemical heterogeneities, full control of nanobubble formation is still currently out of reach. Physically patterning the surface of a material effects the size and contact angle of nanobubbles with previous studies investigating both dots and ribbons within the surface [26, 27]. Graphene, a 2D material with a thickness of 0.34nm, provides an exciting platform to investigate the chemical effect of patterning the surface. Separately the surface properties of graphene under aqueous conditions is also of interest due to graphene's possible applications in bio-sensing [274].

In this chapter, nanobubbles were imaged on the surface of both patterned and unpatterned graphene using high-speed atomic force microscopy. Section 7.2 discusses the samples used and the method of patterning of the graphene. The

experimental setup is described in section 7.3. The methodology to analyse the nanobubbles is detailed in section 7.4. Section 7.5 overviews the results of the nanobubbles on graphene and their properties compared to previous studies. Finally, section 7.6 summarizes the contents of chapter 7.

7.2 Samples

Samples were fabricated using single layer graphene, grown by chemical vapor deposition (CVD) and transferred (by Graphenea) onto Si/SiO_2 substrates. The substrates consisted of a 300-nm thick thermally oxidised SiO_2 layer on top of an undoped silicon substrate, allowing visual inspection of the graphene. On one sample, the graphene was patterned using e-beam lithography and reactive ion etching using oxygen and argon. The ring pattern was composed of graphene rings of external radius of 500nm and an internal radius of 200nm, the total area of the ring was $0.66\mu m^2$. The pattern periodicity was 1.5μm in both x and y. Samples were fabricated and patterned by Cheng Shi, University of Exeter. For full pattern see figure 7.1

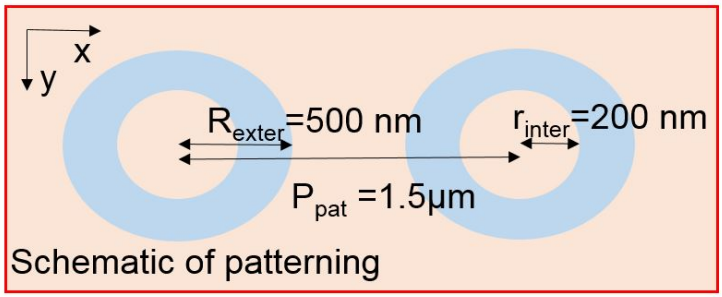

Figure 7.1 Patterning of graphene sample. (Figure 7.1 is part (iii) of figure 4.1).

7.3 Experimental Setup

Nanobubbles were produced using the solvent exchange process, which is the most commonly used protocol for nanobubble production, and has previously been shown to produce the highest bubble density [138, 139, 140]. Solvent exchange involves the washing of the liquid cell with water, then ethanol and then refilling with water. MilliQ water was used, produced from Millipore synergy

185 system. 1ml plastic syringes were used to fill the liquid cell, then the cell was refilled with 0.5ml acetone and then finally refilled with MilliQ water.

Nanobubbles were imaged using high-speed atomic force microscopy (HS-AFM). The HS-AFM was a custom prototype from Bristol Nano Dynamics Ltd (University of Bristol) located at the Single Cell Genomics Laboratory at Plymouth Marine Laboratory, United Kingdom. A triangle cantilever was used (Bruker Nano, MSNL- 10-Triangle-C), with a very low spring constant 0.01-0.03N/m. 2.5MHz bandwidth laser Doppler vibrometer (Polytec) was used to measure cantilever vertical defection. Customized Labview software was used to collect the data at 2 million pixels per second. This system has previously been used in by Landels *et al*., [275] to measure hydrogel. For further details of HS-AFM, see Payton *et al.,* [232]. All HS-AFM measurements were conducted in ambient conditions at room temperature. The image acquisition size ranged from 4.28μm x 4.232μm to 1.135μm x 1.458μm.

In this work, plastic syringes have been used, which have been shown to be an area that induces polydimethylsiloxane (PDMS) contamination [133, 151]. Although plastic contamination has been found in some nanobubble work it is not expected to occur here, due to previous work using the HS-AFM system in liquid showing no bubble anomalies [227, 275].

7.4 Analysis of nanobubbles

High-speed atomic force microscopy was used to image the surface of patterned and unpatterned graphene under air, water and after solvent exchange. The patterning of the graphene was divided into four types, ribbons, rings, dots (circles) of graphene on SiO_2 and dots (circles) of SiO_2 within graphene. The images from the patterning of ribbons, dots of SiO_2 and dots of graphene were less numerous and the patterning was difficult to identify on the surface of the material. Therefore, the samples of unpatterned graphene and patterned rings were focused on.

The high-speed atomic force microscopy acquires data in the form of video files. Gwyddion images were extracted from the video files, when the images had a high resolution and the patterning was clear. The gwyddion is an open access software that enables the analysis of AFM images [276]. The gwyddion images were then reselected to only analyse the images with good resolution and clear patterning. Figure 7.2 shows the comparison of between an image selected and an image that was not selected due to a reduced resolution. This reduced resolution can be due to the HS-AFM moving very fast across the surface and blurring of the image.

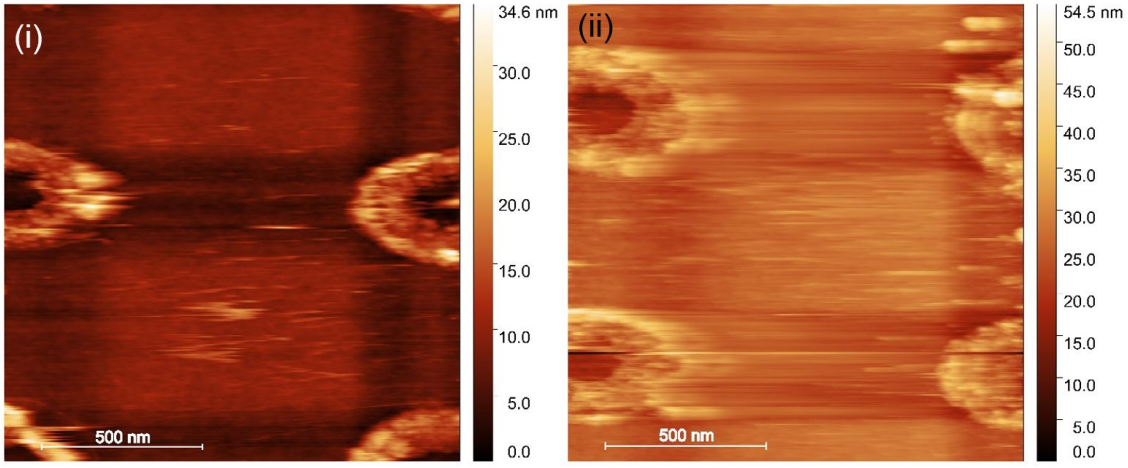

Figure 7.2(i) image selected for analysis (ii) image rejected due to blurring of the image.

Although significant number of images were acquired of HS-AFM in water, there appeared to be a strong variation in bubble formation. Indicating that the solvent exchange might have been occurring during these images as a result of ethanol contamination with the liquid cell. For this reason the images of HS-AFM in water were discounted.

7.4.1 Cross sectional analysis

Figure 7.3, shows HS-AFM images of patterned and unpatterned graphene in air and after solvent exchange. After solvent exchange small spherical domains appeared at the surface of both patterned and plain graphene.

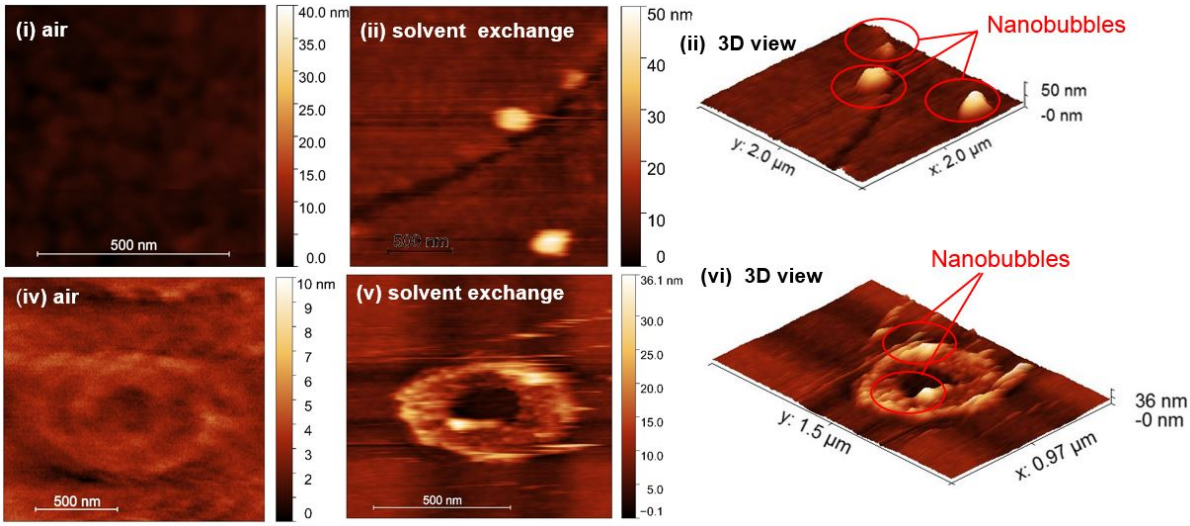

Figure 7.3 (i) Plain monolayer graphene in air, (ii) plain monolayer graphene in water after solvent exchange, (iii) 3D view of (ii), (iv) patterned graphene ring in air, (v) patterned graphene ring in water after solvent exchange, (vi) 3D view of (v).

These raised spherical domains were then identified as nanobubbles by selecting the domains with a height over 10nm and a width of 50nm, then fitting to a spherical cap over four cross sections, see figure 7.4. The increased height of 10nm compared to the selection of 8nm in chapter 6 was due to the stepgate of the patterned graphene. This height over 10nm is compared to the background surface roughness of plain monolayer CVD graphene of 1.6 nm, previous papers have found surface roughness of CVD graphene of between 0.1 to 2nm [174, 277, 278, 279]. Nanobubbles were identified by whether a spherical cap could be used to fit to four-cross sections. The fitting started with 3 initial parameters (co-ordinates of the center of circle and radius) with y the dependent variable and z the independent variable. Domains where the regression coefficient was less than 0.8 for two of the four cross sections were discarded. This is the same spherical cap fitting used in chapter 6, described in section 6.4.2.

In chapter 6, nanobubbles measured using NC-AFM were corrected for the effect of the cantilever tip on the nanobubble shape (section 6.6). Nanobubbles imaged here using HS-AFM were not corrected for the cantilever tip interaction as previous imaging of nanobubbles using HS-AFM has not used tip correction [124].

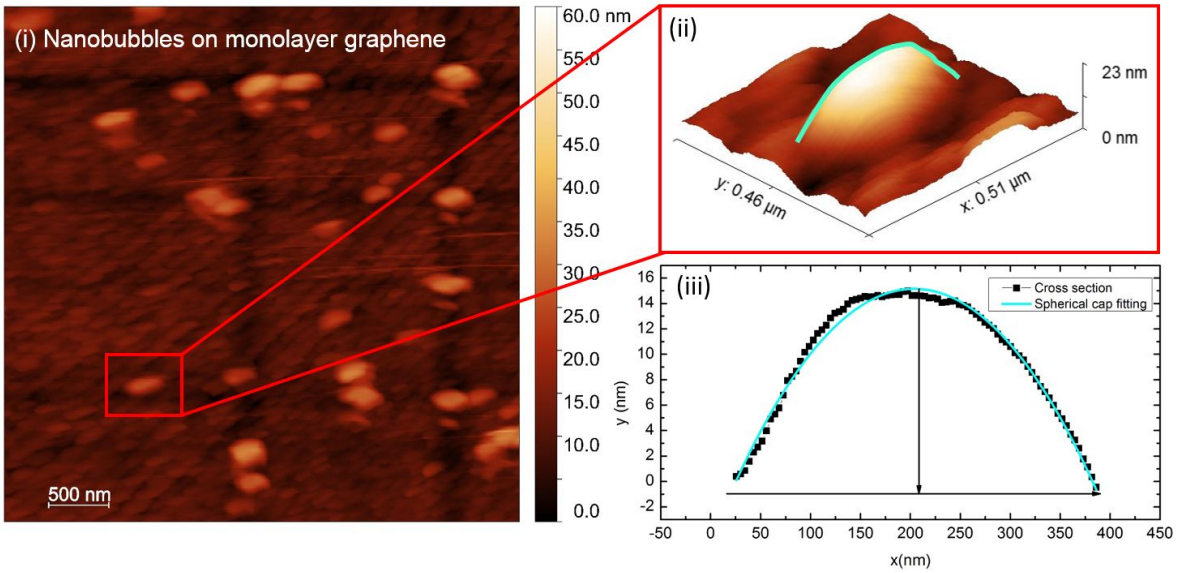

Figure 7.4 (i) Nanobubbles at the surface of plain monolayer graphene, (ii) 3D view of magnified region of (i), (iii) cross section of the nanobubbles identified in (ii).

In the sample containing unpatterned graphene, 49 nanobubbles were identified out of a possible 57 candidates. Nanobubbles were imaged repeatedly on multiple samples on different days. On the sample containing patterned graphene, 16 nanobubbles in total were identified from a possible 34 possible candidates on the graphene rings. No nanobubbles were identified on the underlying SiO_2.

7.5 Discussion

The average height of the nanobubbles on the patterned graphene was 17.1nm with a standard deviation of 4.7nm, with an average lateral length of 209.4nm with a standard deviation of 96nm. The average height of nanobubbles on the monolayer plain graphene was 24.8nm with a standard deviation of 12nm, with the average lateral length of 339nm with a standard deviation of 100nm. The height and lateral length of nanobubbles on graphene in plotted in figure 7.5.

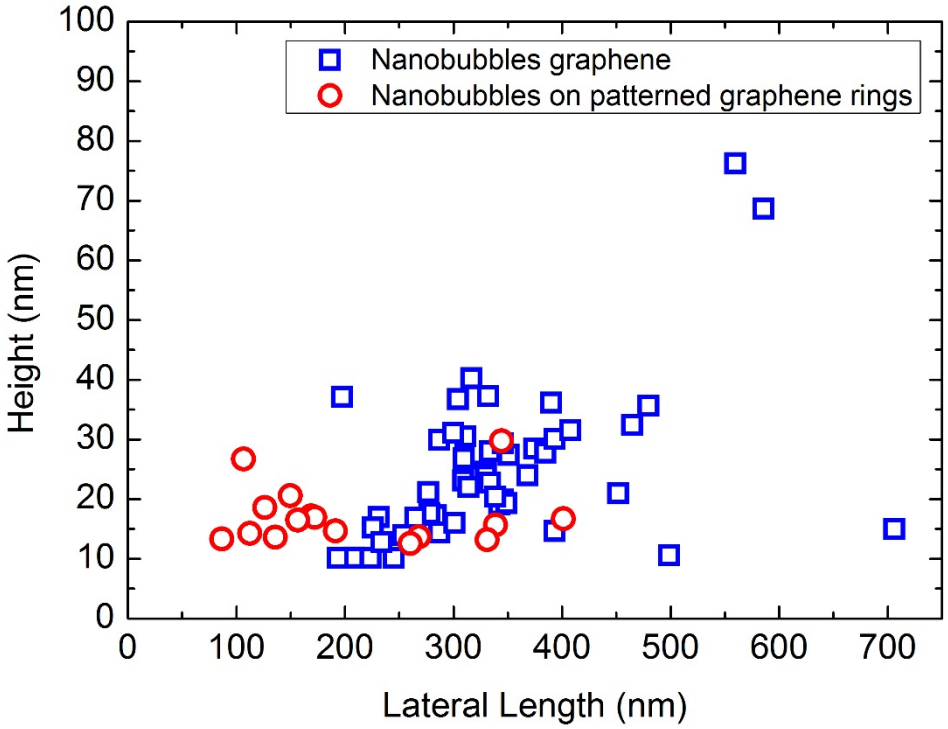

Figure 7.5. Nanobubbles after ethanol exchange plotted height against lateral length.

Nanobubbles located on the graphene rings show a reduced height and lateral length compared to those on unpatterned graphene. Nanobubbles on the plain graphene had lateral lengths up to 700nm, whereas on the patterned graphene only one bubble was observed with a lateral length greater than 300nm, indicating the patterning constrains the nanobubble dimensions. This is consistent with previous studies of nanobubble formation on patterned ZEP and PMMA [26], and polystyrene and poly methyl methacrylate [27]. When different

geometries of dots, nanopores and ribbons were investigated, nanobubbles formed predominantly at the top of the ribbons and on top of the dots if they were of diameter 500nm. Wang *et al.,* [26], investigated patterned nanopores and ribbons on a hydrophobic surface found that these reduced the height and lateral length of the nanobubbles. Although it must be noted that the patterning of the PMMA and ZEP was of a depth of 30nm, whereas single layer graphene only has a thickness of 0.34nm. The stepgate of patterned graphene and the surface was measured as between 1nm to 7nm, this is attributed to either wrinkles within the graphene or the etching cutting into the SiO_2.

The contact angle, θ, of the nanobubbles can be calculated using:

$$sin\,\theta = \frac{4LH}{(L^2 + 4H^2)} \qquad [3.5]$$

Where, *L* is the lateral length of the nanobubble, and *H* is the nanobubble height [112]. The background of this equation is covered in more detail in chapter 3, section 3.2. The average contact angle of nanobubbles on the plain graphene is 16.7 degrees with a standard deviation of 6.5 degrees, whereas the average contact angle of the nanobubbles on the patterned graphene is 22.4 degrees with a standard deviation of 11.3 degrees. The contact angle of nanobubbles on both patterned and unpatterned graphene are consistent with previous values from HOPG and mechanically exfoliated graphene [139, 154]. Theory deviated from Lohse *and* Zhang [112], linked nanobubble contact angle to gas oversaturation, with recent work by Tan *et al.,* [24], building on their earlier work to produce a link between contact angle, gas oversaturation and the hydrophobicity of the surface. The contact angle of the nanobubbles is plotted against the lateral length of the nanobubbles in figure 7.6.

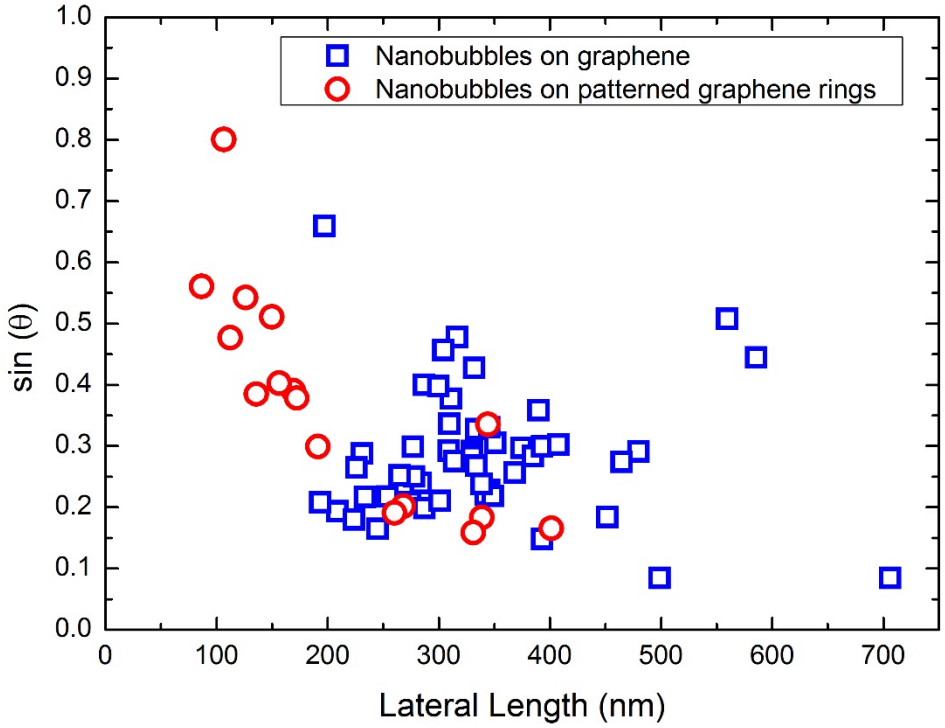

Figure 7.6 Nanobubble length plotted against the contact angle.

The contact angle of the nanobubbles varied significantly, with no clear correlation between lateral length and sin (θ). This lack of clear correlation may be due to measurements being conducted during different days and the solvent exchange process being variable, which would cause changes in localised oversaturation of the gas at the surface. Controlling the solvent exchange process is known to be challenging with many factors effecting the protocol including but not limited to liquid shear, flow boundaries and the saturation within the gas [140]. Therefore, it is not unexpected that the oversaturation varies between different data acquisitions, with previous work also showing negligible correlation between lateral length and contact angle [139].

The nanobubble density within the graphene rings was 0.606 nanobubbles per μm^2, compared to the plain graphene was 0.43 nanobubbles per μm^2, with no nanobubbles found on the SiO_2. The similar value of bubble density on the graphene rings and unpatterned graphene is perhaps as expected as the same solvent exchange process was used for both, and both surfaces have the same hydrophobicity. As the nanobubble images were acquired in multiple sessions

with sample repeats, it is expected that the variation of the solvent exchange process was accounted for with the average of the measurements. The solvent exchange process is expected to be more variable than the gas oversaturation method used in chapter 6.

Nanobubbles are known to be pinned by either physical or chemical heterogeneities [18]. As the monolayer graphene has a thickness of 0.34nm, the depth of the patterning is much smaller than that used in previous studies (15nm-40nm), indicating that the pinning may be predominately due to the chemical differences of the surface, rather that the physical patterning. In this case, there would have to be a difference in the hydrophobicity of the patterned graphene and the underlying SiO_2.

The surface behaviour of graphene is complex, with the underlying substrate and production method affecting the wettability in some cases [107]. Previous work on graphene has shown the macroscopic contact angle, a value of the wettability, to range from 96 degrees to 127 degrees, although the more recently agreed value is between 95- 100 degrees. These results show that graphene is predominantly hydrophobic [280, 281, 282, 283], consistent with previous studies of nanobubbles on graphene. Hong *et al.,* [284], investigated the surface of CVD graphene on top of SiO_2/Si substrate, extracting a contact angle of 88 degrees for macroscopic droplets on the graphene, and a contact angle of 46 degrees for macroscopic bubbles on the underlying SiO_2. The greater hydrophobicity of graphene compared to the underlying substrate would lead to a greater density of bubble formed on the graphene than the SiO_2, as observed in these measurements. It should be noted that the hydrophobicity of graphene can be altered over time, and can be reduced due to the presence of water [174]. As the nanobubbles in this work were not compared to the time in which they formed, it is uncertain if this effect played a role in the nanobubble density.

Previous research has shown that nanobubbles can form on the surface of the natural form of silicon dioxide, quartz. Although many studies have investigated nanobubbles on silicon dioxide, mostly they involve surfaces that have been coated to increase the hydrophobicity with substances such as PFDDMCS, with the hydrophobicity largely depending on the coating [116, 285, 286]. Nanobubbles have not been measured on silicon dioxide however they have been measured at the surface of the natural form of silicon dioxide (quartz) by Babel *and* Rudolph [15]. As the nanobubbles surface of the quartz were measured in potassium octylxanthate, a collector used to hydrophobize the surface, it would be expected nanobubbles would form compared to the de-ionised water used here [15]. Tan *et al.,* [24, 25]*,* found that nanobubbles formation and stability not only depends on the nanobubble pinning, but also the oversaturation or hydrophobicity. In this case, it is therefore likely solvent exchange resulted in an oversaturation too small to form nanobubbles on the surface of SiO_2 [112].

Finally, although nanobubbles are commonly identified using either force-separation curves or changes in the phase image of the AFM image, this was not possible in the HS-AFM system used as the contact mode does not produce phase images, and the mechanical head cannot be tested at a single location for force separation curves as the HS-AFM works with no z direction feedback. Studies have shown that in some cases when using solvent exchange, instead of nanobubbles, nanodroplets or nanoparticles can be produced at the surface [287]. Nanodroplets are bubbles filled with liquid rather than gas [288], which can be experimentally distinguished from nanobubbles using AFM [152, 153], but normally by using force separation curves. An *et al.,* [152], showed that nanodroplets imaged using a high force AFM (>3nN) were neither moved nor destroyed, but deformed from a standard bubble shape with a spherical cap. In these measurements, as shown in figure 7.7, the nanobubbles did not deform, but could be moved whilst retaining their shape. This is consistent with previous work [114], and indicates that the domains studied were nanobubbles rather than nanodroplets.

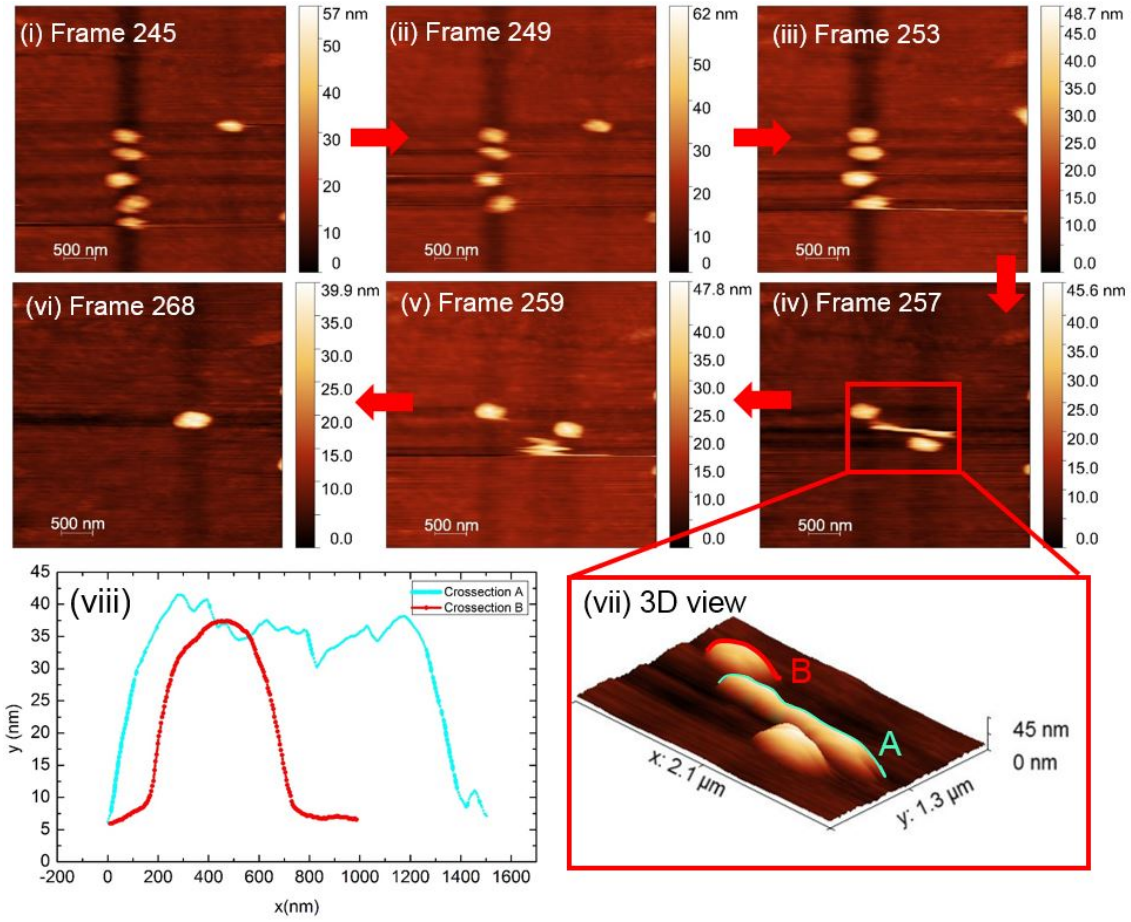

Figure 7.7 Movement of nanobubbles at the surface of graphene under HS-AFM imaging. (i),(ii),(iii),(iv),(v),(vi) nanobubbles under HS-AFM imaging reducing from six nanobubbles to one nanobubble.(vii) 3D magnified view of (iv) where a nanobubble is stretched (viii) cross sections of A, normal nanobubble, B stretched nanobubble.

Future work will focus on a wider range of geometries, and the use of other 2D materials, to further explore the effect of patterning on nanobubbles size, contact angle and density, this is discussed in more detail in chapter 8.

7.6 Summary

In this chapter, surface nanobubbles, produced using the solvent exchange production method, were imaged using high-speed atomic force microscopy at the surface of patterned and unpatterned monolayer graphene. On the sample containing patterned graphene, nanobubbles were only found on the surface of the graphene and not on the underlying SiO_2, which is consistent with the difference in hydrophobicity between graphene and SiO_2. The patterning of the graphene into rings constrained the geometry of the nanobubbles, with the lateral length reduced and the contact angle increased. This agrees with previous work on patterning which showed nanobubbles can be constrained using patterned surfaces. Graphene's potential use in microfluidics makes it an ideal candidate for future studies, as nanobubbles could play a role in some lab-on-a-chip processes, and could ultimately lead to the ability to dynamically move nanobubbles using, for example, an applied gate bias to change the surface properties of the graphene. Finally, the use of high-speed atomic force microscopy further validates this technique for the study of nanobubbles.

This work builds on the results in chapter 6, on the pinning of nanobubbles at the surface of materials .The future development of work discussed here is described in chapter 8.

Chapter 8
Conclusions and future work

The research in this thesis focuses on the surface behaviour of materials for improving their processing. The surface behaviour of surfaces can be measured in a wide range of methods. The two methods focused on in this work were zeta potential measurements and atomic force microscopy. These were selected as they have been regularly used to measure surface charge and nanobubbles respectively.

The surface behaviour of minerals is important in their processing and extraction as many mineral deposits are processed using froth flotation, which relies on the physio-chemical properties of the mineral surface [60]. As ore deposits are exhausted, the deposits remaining are more complex with a lower percentage of ore minerals [4]. This is particularly true of rare earth ore deposits, which often contain over 20 minerals and therefore multiple highly complex steps of processing [5]. Zeta potential measurements are used to understand the surface behaviour of a mineral under different aqueous conditions [65, 259]. As many rare earth minerals have only become commercially viable recently, few have had their surface behaviour characterized, limiting developments in new deposits [5]. The fluorcarbonate mineral bastnäsite has been mined for rare earth elements since the 1950's, and is one of the few rare earth minerals with well characterized surface behaviour [57]. This earlier work on bastnäsite inspired the work into zeta potentials of the rare earth fluorcarbonate mineral, parisite conducted in this thesis. A major finding of this research is that the surface behaviour of the rare earth fluorcarbonates are similar under collector and supernatant conditions.

Nanobubbles are thought to play an important role in froth flotation, and can indicate a minerals' hydrophobicity [15, 20]. They have small contact angles and long lifetimes due to a combination of gas oversaturation, surface

hydrophobicity and surface pinning [24, 112]. Nanobubbles have been shown to be important in a wide range of processes, from mineral processing to cancer treatment [105, 120]. However, nanobubbles have only been investigated on a limited number of mineral surfaces making understanding nanobubble populations on minerals challenging [15, 163]. This thesis builds upon the work on nanobubbles at the surface of minerals, investigating nanobubbles' properties such as contact angle and lateral size, under different reagent conditions.

The surface behaviour of materials such as graphene is important in its possible uses in areas such as cancer treatment and electrolysis [107, 174]. Nanobubbles between layers of graphene have previously been shown to have potential industry applications in energy storage [171]. By improving understanding by the use of nanobubbles, the utilisation of graphene in sensing devices can also be improved [106]. The characteristics of graphene, in particular the thickness of monolayer graphene, makes it ideal for investigating the pinning of nanobubbles by physical and chemical heterogeneities.

This chapter discusses the main findings of the thesis and future directions of research based on this work. In section 8.1, surface charge measurements of rare earth minerals to improve their processing using froth flotation are described. The measurement and interpretation of nanobubbles on both a rare earth mineral surface and a common rare earth gangue (waste) mineral are reviewed in section 8.2. Section 8.3 summaries the investigation of nanobubbles on both patterned and non-patterned graphene surfaces to investigate pinning on chemical and physical heterogeneities. Finally, section 8.4 discusses possible future research.

8.1 Behaviour of rare earth minerals

The surface charge properties of rare earth minerals were investigated using zeta potential measurements. The zeta potential measurements were conducted on a rare earth fluorcarbonate mineral, parisite and a rare earth enriched phosphate mineral, apatite. Although some rare earth minerals, such as bastnäsite, have previously been investigated, these are the first results of surface behaviour of parisite and rare earth enriched apatite.

Parisite from Snow Bird Mine, Montana was investigated using electro-streaming to measure zeta potential. The iso electric point of parisite was measured at pH 5.6 in water. This value is at the lower end of the IEP values of bastnäsite, which range from pH 4.6 to pH 9.3 in the literature. Under reagent collector conditions parisite behaves in a similar way to bastnäsite, with the value of zeta potential decreasing with increasing pH, and the IEP shifting to lower values compared to those obtained under water conditions. This similar behaviour extends to zeta potential values under supernatant conditions, where a decrease in zeta potential values was measured, compared to those obtained under water, as have previously been observed for bastnäsite. As many REE fluorcarbonate deposits, particularly those containing synchysite and parisite are already processed in a similar way to bastnäsite, this research validates this approach.

In exploration and development of rare earth element (REE) deposits, not only is the deposit size vital but, particularly in the case of REE, the ease of extraction is extremely important [3]. If it is possible to predict that all REE fluorcarbonates behave in a similar way to bastnäsite during flotation, then much of the research that has already been conducted into surface behaviour with regards to reagent addition remains valid.

In the second part of this work, the iso electric point of REE enriched apatite from Brazil was measured at pH 3.8 in water conditions. The surface charge of the REE enriched apatite under hydroxamic and fatty acid conditions was highly

reduced, giving an IEP of <3.5. This behaviour is similar to non-REE enriched apatite surface behaviour. Thereby indicating that REE enrichment does not affect the surface behaviour of apatite under common rare earth collectors. This implies that flotation research into apatite could be applied to future mineral processing of REE enriched apatite.

8.2 Nanobubbles on minerals

Nanobubbles were imaged at the surface of the carbonate mineral, dolomite, and the rare earth fluorcarbonate mineral, synchysite, using dynamic mode non-contact force microscopy. Dolomite is a common gangue mineral in many rare earth ore deposits with the rare earth fluorcarbonate mineral synchysite being an important ore mineral in a number of mines such as Strange Lake, Quebec and Songwe Hill, Malawi. Although the surface behaviour of dolomite is well researched, synchysite is a highly unstudied mineral with few studies on its behaviour. Although nanobubbles have been investigated on a wide range of material surfaces, their relationship to froth flotation is still poorly understood. Previous research into nanobubbles on mineral surfaces have focused on galena or chalcopyrite, without investigating the contact angles or links between reagents and pinning to the surface. These measurements provide the first images of nanobubbles on dolomite and synchysite, and enable the investigation of the nanobubble contact angle and density at mineral surfaces.

Nanobubbles were created using the gas oversaturation method by heating cooled liquid to induce oversaturation at the material surface. The nanobubbles were identified from the images by comparing the phase and topography images from NC-AFM, and then by fitting to spherical cap model. On dolomite the observed bubble density was highest under collector conditions, with 0.656 bubbles per μm^2, compared to 0.342 nanobubbles per μm^2 under water conditions. Due to the limited image acquisitions for synchysite no bubble density was calculated. The average contact angle of 23.8^o of synchysite in collector conditions was higher than surface nanobubbles on the mineral dolomite, which showed a contact angle of between 15.14^o and 9.74^o

depending on the aqueous conditions. These results were in range with previous studies on mineral surfaces which had contact angles between 8 and 60 degrees [15, 120, 163].

The presence of nanobubbles on the synchysite sample indicated the surface was highly hydrophobic under collector reagent conditions. This is one of the first results of synchysite surface behaviour, previous work has focused on other rare earth fluorcarbonates or complex ores. The differences in bubble density on dolomite in different reagents implies that the reagents effect both the hydrophobicity and the bubble pinning between the surface and the nanobubble. As pinning has previously been shown to be affected by both chemical and physical heterogeneities in the surface, in this system it is suggested that the chemical heterogeneities dominate the pinning.

.

8.3 Nanobubbles on patterned graphene

Surface nanobubbles were imaged using high-speed atomic force microscopy at the surface of patterned and plain monolayer chemical vapour deposition graphene. Nanobubbles were produced using the solvent exchange production method, with ethanol the solvent used. The nanobubbles were only found on the surface of the patterned graphene, but not on the underlying SiO_2. The surface of graphene is known to be hydrophobic and previous research into graphene coated SiO_2 wafers covered with graphene has shown nano sized bubbles in water [174]. The patterning of rings constrained the geometry of the nanobubbles, with the lateral length reduced and the contact angle increased. This agrees with previous work on patterning which showed nanobubbles can be constrained using patterned surfaces [26, 27]. As the thickness of graphene is 0.34nm, it is expected that the pinning is dominated by chemical heterogeneities rather than physical patterning.

Nanobubble density between unpatterned and patterned monolayer graphene was not significantly different with the bubble density ranging from 0.43 to 0.6

nanobubbles per μm^2, as it is expected that the nanobubble density would not be significantly affected by patterning. This is only the second time nanobubbles have been imaged using high-speed atomic force microscopy, a method which has shown significant advances in imaging in biology and other materials sciences. Although nanobubbles have been studied in depth on surfaces such as highly ordered pyrolytic graphite and mechanically exfoliated graphene, this is the first time conventional nanobubbles on chemical vapour deposition graphene have been investigated. This work aids research into the application of nanobubbles in microfluidics, and increases the understanding of nanobubble formation within patterning.

8.4 Future work

8.4.1 Rare earth minerals

An important aspect of this work was the study of the surface behaviour of rare earth minerals. However, a limitation of this work, was the volume of studies, which was due to many REE minerals only occurring in small quantities. A promising area of investigation into rare earth minerals behaviour is the creation of synthetic samples that are more representative of minerals within mineral processing [289]. Although many studies of synthetic apatites have been conducted, their properties do not always match the properties of natural apatite [12, 253]. This could be improved as manufacturing of synthetic minerals is refined. In apatite research more studies of hydroxylapatite and chlorapatite are important due to possible differences in their surface behaviour. As rare earth fluorcarbonates such as synchysite and röntgenite exist in such small quantities in natural ore samples [81], the production of synthetic samples opens an exciting avenue for additional tests on these minerals including investigations into the bonding between collectors and the surface.

The bonding between the reagents and the mineral surfaces is a key aspect in the understanding and optimising of flotation [72]. This is an area although discussed in this thesis was not experimentally investigated. Methods such as

attenuated total reflectance fourier transform infrared (ATR-FTIR) spectroscopy and x- ray photoelectron spectroscopy (XPS) can indicate the bonding between mineral and reagents and has shown it can significantly improve understanding of bastnäsite flotation [7, 62, 290, 291]. Future work is suggested to investigate the bonding mechanisms between rare earth fluorcarbonates other than bastnäsite and common collectors to continue to investigate rare earth fluorcarbonate surface behaviour.

Apart from the rare earth fluorcarbonates there are over 200 rare earth minerals currently identified [5]. There is still a significant number of REE minerals of economic interest, whose surface behaviour under common collectors is not known. These minerals include rare loparite [292]. Loparite, $(Ce,Na,Ca)(Ti,Nb)O_3$, is known as one of the main REE ore minerals within the Kola Penninsula, Russia [293, 294]. Although there are many published investigations into the mineralogy, gravity separation and leaching of loparite, there is no published data on zeta potential measurements under flotation conditions [295, 296, 297]. Although as loparite is primarily mined in Russia, it is likely that more research has been conducted on loparite which is either not published or not translated into English. Loparite has also been found in deposits such as Saima, Northeastern China, Schryburt Lake, Canada and Pilansberg, South Africa making future understanding of its surface behaviour of economic interest [298, 299, 300]. Future work is suggested to investigate the fundamental surface behaviour of different loparites under common REE collectors, such as hydroxamic acid or fatty acids. It is suggested that the loparites selected have a minimal Th or U content to enable safe handling.

8.4.2 Nanobubbles at the surface of minerals

The use of nanobubbles in mineral processing has long been theorized and is a promising area of future research [15, 20]. However, the limited number of studies into the effects of mineral parameters limits the progress in the field. A major finding of this research is the measurement of nanobubbles at the surface of the minerals dolomite and synchysite. Future work could investigate

nanobubbles at the surface of different minerals, in particular to determine if the effect on nanobubble population density is consistent with other reagent regimes. For example xanthate collector reagents at the surface of the sulphide mineral galena [301].

Recent work into mapping the hydrophobicity of minerals provides insight to the possibility of using nanobubbles as a tool to improve flotation [15]. Nanobubbles could be good indicators of the hydrophobicity of the sample, thereby mapping the floatability of different minerals within one ore mineral cross section under a specific reagent regime. This could determine if the surface of the ore mineral is hydrophobic and the surface of the waste minerals are hydrophilic. This is particularly pertinent when ore minerals are found in too small amounts for micro flotation or other common methods to determine surface hydrophobicity [15]. As many mineral deposits being explored are more complex, due to exhaustion of more high-grade less complex deposits, this tool could enable optimisation in flotation [302]. Rare earth element deposits consistently have highly complex mineralogy and such a tool to understand hydrophobicity under collector reagents could improve processing [5, 57, 6]. Future work could explore this avenue in improving flotation.

8.4.3 Nanobubbles at the surface of 2D materials and for heating

A key finding of this work was the measurement of nanobubbles at the surface of patterned and unpatterned monolayer graphene. This measurement of nanobubbles on graphene rings validated the earlier findings that nanobubbles can be constrained by patterning of hydrophobic and hydrophobic surfaces [26, 27]. However, only a limited number of geometries have been explored such as nanopores, ribbons and dots. Future work could focus on a greater variation of patterned geometries to determine when the nanobubbles can become constrained by specific patterning. A suggested geometry would be thinning and thickening ribbons, which would enable the detection of lateral length constraints for nanobubble formation. Previous findings have been contrasting

to other results with nanobubble formation at hydrophilic domains being increased, comparing future work to such results would be advantageous [18].

Controlling the solvent exchange process and water heating method of inducing oversaturation is key to controlling gas oversaturation and therefore nanobubble formation [18, 140]. As controlling the oversaturation within a gas system requires a closed liquid cell, few studies have investigated this area [18]. Zhang *et al.,* [303] made the first steps toward understanding flow conditions for nanodroplet formation using solvent exchange, finding that the volume of the nanodroplets increases with the Peclet number in flow conditions. Future work could apply this area of research to nanobubble formation using solvent exchange. This could be achieved by experimentally altering flow rate and channel width for nanobubble formation and then modelling these changes with a finite element model system such as COMSOL Multiphysics software. COMSOL has previously been used to model nanobubbles generated using electrolysis [304, 305]. As controlling nanobubbles using patterning is only one facet of the nanobubble story, optimising the production method for nanobubbles is key to control formation.

Finally, nanostructured surfaces have been shown to improve nucleate heating [306], with recent work demonstrating a new method of nucleate boiling via oscillating microbubbles on an electrical micro-heater [307, 308]. In these systems, the size and density of the surface bubbles determines the thermal contact between the heating element and fluid, with smaller bubbles increasing the efficiency of boiling. As such if microbubbles significantly improve the efficiency of boiling, nanobubbles could extend on this improvement within this system. Therefore controlling formation of surface nanobubbles has the potential to further optimise this heating process. Future work could combine controlling nanobubble formation on patterned surfaces and nano heating devices.

List of Publications

[1] Owens, C.L., Nash, G.R., Hadler, K., Fitzpatrick, R.S., Anderson, C.G. and Wall, F., 2018. Zeta potentials of the rare earth element fluorcarbonate minerals focusing on bastnäsite and parisite. *Advances in colloid and interface science*, *256*, pp.152-162.

[2] Owens, C.L., Schach, E., Rudolph, M. and Nash, G.R., 2018. Surface nanobubbles on the carbonate mineral dolomite. *RSC Advances*, *8*(62), pp.35448-35452.

[3] Owens, C.L., Nash, G.R., Hadler, K., Fitzpatrick, R.S., Anderson, C.G. and Wall, F., 2019. Apatite enrichment by rare earth elements: A review of the effects of surface properties. *Advances in colloid and interface science*. 265. pp 14-28.

[4] Owens, C. L., Schach, E., Heinig, T., Rudolph, M., Nash, G. R., 2019 Surface nanobubbles on the rare earth fluorcarbonate mineral synchysite. *Journal of Colloid and Interface Science.* 552, pp. 66-71.

Appendix

Table A.1. shows XRF results with the full elementary and chemical composition with estimated error, of a parisite-(Ce) sample from Snowbird Mine, Mineral Country, Montana, USA.

Compound	Wt%	Est.Error	Element	Wt %	Est.Error
CeO2	33.62	0.24	Ce	27.37	0.19
La2O3	16.66	0.19	La	14.20	0.16
CaO	13.46	0.17	Ca	9.62	0.12
Nd2O3	13.09	0.17	Nd	11.22	0.14
Pr6O11	3.67	0.10	Pr	3.04	0.09
ThO2	2.75	0.08	Th	2.42	0.07
Y2O3	2.73	0.08	Y	2.15	0.06
BaO	2.67	0.19	Ba	2.39	0.17
SiO2	2.23	0.07	Si	1.04	0.03
Sm2O3	1.81	0.08	Sm	1.56	0.07
Cs2O	1.68	0.15	Cs	1.59	0.14
Gd2O3	1.57	0.17	Gd	1.36	0.15
Na2O	1.08	0.38	Na	0.804	0.28
As2O3	0.516	0.11	As	0.391	0.08
Dy2O3	0.413	0.05	Dy	0.360	0.048
Fe2O3	0.361	0.018	Fe	0.252	0.013
I	0.319	0.10	I	0.319	0.10
K2O	0.318	0.016	K	0.264	0.013
PtO2	0.197	0.023	Pt	0.169	0.020
P2O5	0.158	0.040	Px	0.0691	0.017
NiO	0.121	0.014	Ni	0.0950	0.011
Ag2O	0.116	0.06	Ag	0.108	0.05
WO3	0.105	0.041	W	0.0835	0.032
Au	0.0885	0.017	Au	0.0885	0.017
SO3	0.0767	0.021	Sx	0.0307	
Er2O3	0.0675	0.031	Er	0.0590	0.027
Cl	0.0491	0.029	Cl	0.0491	0.029
ZrO2	0.0441	0.033	Zr	0.0327	0.025
CuO	0.0301	0.013	Cu	0.0241	0.010

Table A.1. XRF chemical composition analysis results.

Table A. 2 shows XRF results with the full elementary and chemical composition with estimated error, of apatite from Jacupiranga, Brazil.

Compound	Wt%	Est.Error	Element	Wt%	Est.Error
P2O5	39.03	0.24	P	17.03	0.11
CaO	35.59	0.24	Ca	25.45	0.17
BaO	8.77	0.42	Ba	7.86	0.37
Cs2O	5.59	0.32	Cs	5.28	0.31
Na2O	3.63	0.10	Na	2.69	0.08
I	2.55	0.23	I	2.55	0.23
SrO	1.42	0.06	Sr	1.20	0.05
TeO2	1.20	0.28	Te	0.957	0.22
Cl	0.447	0.022	Cl	0.447	0.022
As2O3	0.424	0.07	As	0.321	0.05
Ag2O	0.229	0.08	Ag	0.213	0.08
SiO2	0.212	0.015	Si	0.0993	0.0072
ThO2	0.190	0.07	Th	0.167	0.06
Nb2O5	0.149	0.033	Nb	0.104	0.023
K2O	0.140	0.0070	K	0.116	0.0058
RuO4	0.128	0.07	Ru	0.0974	0.05
Rb2O	0.0637	0.021	Rb	0.0583	0.019
ZrO2	0.0503	0.041	Zr	0.0372	0.030
Fe2O3	0.0457	0.0038	Fe	0.0320	0.0026
Au	0.0295	0.0089	Au	0.0295	0.0089
SO3	0.0282	0.0049	S	0.0113	0.0020
PtO2	0.0204	0.011	Pt	0.0175	0.0096
CuO	0.0158	0.0041	Cu	0.0126	0.0033
Er2O3	0.0146	0.0079	Er	0.0127	0.0069
ZnO	0.0119	0.0048	Zn	0.0096	0.0039
Tb4O7	0.0087	0.0080	Tb	0.0074	0.0068
NiO	0.0052	0.0036	Ni	0.0041	0.0028
MnO	0.0050	0.0033	Mn	0.0039	0.0026

Table A.2. XRF chemical composition analysis results.

Table A.3 Table of selected REE fluorcarbonates.

Mineral	Example of locations	Chemical Formula	Theoretical or measured chemical composition in oxides	Crystal System	Ref.
Bastnäsite-(Ce)	Bayan Obo, China. Mountain Pass, USA. Fen, Norway	$Ce(CO_3)F$	Ce =63%. C=5%. O=21.9%. F=8.67%	Hexagonal	[273, 309]
Bastnäsite-(La)	Pike Peaks, Colorado, USA	$La(CO_3)F$	La= 63%. C=5%. O=22%. F=8.72%	-	[36]
Bastnäsite-(Nd)	Clara Mine, Germany Stetind pegmatite, Norway	$Nd(CO_3)F$	Nd =26%, La =18%, Ce=18%, F=9%, (CO_2 was not measured due to paucity of mineral).	Hexagonal	[238, 310]
Bastnäsite-(Y)	Bayan Obo, China. Nissi Bauxite Laterite Deposit, , Greece	$Y(CO_3)F$	Y=52%. C=7.15%. O=28%.F=11%	-	[311, 312]
Thorbastnäsite	Yaja granite, China Eastern Siberia, Russia	$ThCa(CO_3)_2F_2$ $3H_2O$	Ce=6.88%, C=4.72%, Ca=5.9%, Th=45.57%, H=1.19%, F=7.46%	Hexagonal	[313, 314]
Hydroxylbastnäsite-(Ce)	Kami-houri, Miyazaki Prefecture, Japan, Trimouns, France	$Ce(CO_3)(OH)$	Ce=64%, O=29%, C=5.53%, H=0.46%	Hexagonal	[42, 315]

Hydroxylbastnäsite-(Nd)	Montenegro	Nd (CO_3) (OH)	Nd=65%, O=28%, C=5.43%, H=0.46%	Hexagonal	[316]
Parisite-(Ce)	Muzo, Bayaca, Columbia	$CaCe_2(CO_3)_3F_2$	Ce=28%. La=23%. C=6%. O=26% F=7%. Ca=7%	Monoclinic	[81, 317]
Parisite-(La)	Mula Mine, Bahia, Brazil	$CaLa_2(CO_3)_3F_2$		Monoclinic	[318]
***Parisite-(Nd)**	Bayan Obo, ,China found in 1986	$CaNd_2(CO_3)_3F_2$	Nd=23%. La=20%. Ce=10%. C=6%. O=25%. F=6%. C=6%	-	[319, 320]
Röntgenite-(Ce)	Narssârssuk, Greenland (Denmark). Muso, Columbia	Ca_2Ce_3 $(CO_3)_5F_3$	Ce=37%. La=12%. C=7%.O=28%. F=6%. Ca=9%.	Hexagonal	[37, 39]
Synchysite-(Ce)	Songwe Hill, Malawi. Springer Lavergne, Canada	$CaCe(CO_3)_2F$	Ce=43%. C=8%. O=30%. F=6%. Ca=13%	Monoclinic	[41, 185, 321]
Synchysite-(Y)	Kutessay, Kyrgyzstan	$CaY(CO_3)_2F$	Y=33%. C=9%. O=36%. F=7%. Ca=14%.	Monoclinic	[1, 322]
Synchysite-(Nd)	Triolet Glacier, Italy Grebnik deposit, Kosovo	$CaNd(CO_3)_2F$	Nd=44%. C=7%. O=30%. F=6%. Ca=12%.	No XRD data	[322, 323]

*Table A.3 Table of selected REE fluorcarbonates, chemical composition and examples of localities. Location lists the deposit name, country as stated by the literature, which may not cover modern borders. Chemical formulae are taken from International Mineral Association (IMA) Commission on New Minerals, Nomenclature and Classification (CNMNC). *Parisite-(Nd) not officially recognised by IMA CNMNC list as of July 2017.*

Table A.4. Table of selected REE enriched apatite deposits.

Deposit Name	Geological Setting	Country	Type of apatite	REE (% or ppm)	Reference
Phalaborwa	Carbonatite	South Africa		La 1245ppm	Dawson *and* Hinton [324]
Songwe Hill	Carbonatite	Malawi	Fluorapatite	6200ppm Ce, 3400ppm Nd	Broom-Fendley *et al.,* [261]
Juquia		Brazil	-	1035ppm	Walter *et al.,* [257]
Kovdor	Carbonatite	Kola,-Russia	-	1740ppm Nd, 3770 ppm Ce	Kempe *and* Gotze [325]
Ermakorka (Transbaikalia)	Carbonatite	Russia	-	6610ppm Ce, 5130ppm La	Kempe *and* Gotze [325]
Hillside deposit	Iron-oxide-copper-gold	Australia	Fluorapatite	1100ppm- >2%	Ismail *et al.,* [326]
Oka, Quebec	Carbonatite	Canada	Fluorapatite- hydroxyl-fluorapatite	6000-34000ppm REE	Hornig-Kjarsgaard *et al.,* [247]
Hoidas Lake, Saskatchewan	Monzogranitic and tonalitic gneiss.	Canada	Fluorapatite	1.5-5% REE enrichment	Halpin *et al.,* [327] Pandur *et al.,* [258]

Minami-Torishima Area, Southeastern Japan	Deep sea mud	Japan	-	9300–32,000 REE	ppm	Kon *et al*., [328]
Esfordi		Yazd Province, Iran	Fluorapatite, Britholite			Soltani *et al.,* [50]

*Table A4. adapted from Broom-Fendley et al., [32]. A sample of REE enriched apatite deposits. This list includes a selection of REE enriched apatite deposits and is not representative of the entire list of deposits. *%REE denotes investigations into the mineralogy of deposits and does not represent the enrichment of all apatite within the deposit or its economic viability.*

Table A5. Published studies of REE fluorcarbonate zeta potentials.

Mineral	Deposit	Country	Purity	Size µm	PZC	IEP	Background Electrolyte	IEP in collector	Method	Year	Study
Bastnasite (Ce)	-	-		D_{50} =2.3		7-8	10^{-3}M/L NaCL		Electrokinetic	2017	Espiritu et al., 2017 [243]
Bastnäsite	Mountain Pass	USA	some barite	<5	-	7	10^{-1} M KNO_3	na	-	2017	Azizi et al., 2017 [71]
Bastnäsite (Ce)	Mountain Pass	USA	some barite	<5	-	7	10^{-1} M KNO_3	5.8		2016	Sarvaramini et al., 2016 [72]
Bastnäsite	-	-	-	<10	-	8	10^{-3}M NaCl		-	2016	Espiritu et al., 2016 [202]
Bastnäsite	Zagi Mountain	Pakistan		-45		9	-		-	2016	Liu et al., 2016 [73]
Bastnäsite	Mountain Pass	USA	some barite	<5	-	7	10^{-1} M KNO_3	4	-	2016	Azizi et al., 2016 [74]
Bastnäsite-(Ce)	-	-	Handpicked	<32	-	8.2	-	6.6, 5.2		2015	Anderson 2015 [75]
Bastnäsite-(Ce)	Mountain Pass	USA	57.4 REO% compared to 75 pure REO%	<37	9.2	-	10^{-3} M $NaNO_2$ Also 10^{-3}M NaF		-	2015	Pradip et al., 2015 [84]

Bastnäsite	synthetic	-	100% pure		7.8		10^{-3} M $NaNO_2$ Also 10^{-3}M NaF			2015	Pradip et al., 2015 [84]
Bastnasite	Zagi Mountain	Pakistan		-45	8.1				Micro-electrophoresis	2014	Zhang 2014 [329]
Bastnäsite	-	-	72.05REO %	-25	-	5.3	10^{-2} M KCl	-	-	2014	Fang et al., 2014 [76]
Bastnäsite-(Ce)	Mountain Pass	USA		d50=1.9	-	6.4	10^{-3}M KCl	8.9	Electrophoresis	2014	Jordens et al., 2014 [57]
Bastnäsite-(Ce)	-	Madagascar		d50=2	-	8.1	10^{-3}M KCl	10.2	Electroacoustic	2014	Jordens et al., 2014 [57]
Bastnäsite-(Ce)	-	Madagascar		d50=2	-	6.2	10^{-3}M KCl	7.6	Electrophoresis	2014	Jordens et al., 2014 [57]
Bastnäsite	Birthday Claim, Mountain Pass	USA	52% Cerium	75	-	9.3	Na NO_3	-	Electro kinetic	2013	Herrera-Urbina et al., 2013 [83]
Bastnäsite-(Ce) or Bastnäsite-(La)	Zagi Mountain	Pakistan	-	45	8.1		-	-		2013	Zhang et al., 2013 [290]
Bastnäsite		Vietnam				4.7	-			2010	Kim et al., 2010 [330]

Bastnasite	Haoniuping Mine	China	96.50% pure	37	-	7.8	-	-	Electrophoresis	2000	Ren et al., 2000 [77]
Bastnäsite-(Ce)	Maoniuping Mine, Sichuan Province	China	98.10% pure	37	-	8	Water	5.9	Electrophoresis	1997	Ren et al., 1997 [78]
Bastnäsite-(Ce)	Pocos de Caldas, MG.	Brazil	-	37	-	4.9	10^{-3} KCl	4.2	Micro Electrophoresis	1996	Pavez et al., 1996 [79]
Bastnäsite	Mountain Pass	USA	Handpicked	<10	-	4.6	Pure water	-	-	1986	Smith and Shonnard 1986 [82]
Bastnäsite	Bayan Obo	China	Handpicked	10	-	7	10^{-3} KNO_3	-	Electrophoresis	1984	Luo and Chen 1987 [331]
Bastnäsite	synthetic		100%			7.8	Pure water			1982	Li 1982 [332]
Bastnäsite	Mountain Pass	USA				9.25	-			1981	Pradip 1981 [333]
Bastnäsite	Mountain Pass	USA	Handpicked	1-10	-	5.3 (>30 minutes)	water-		Electrophoresis	1980	Smith and Steiner 1980 [80]
Bastnäsite	Mountain Pass	USA	Handpicked	1-10		6.8 (2 hours)	water-		Electrophoresis	1980	Smith and Steiner 1980 [80]
Bastnäsite	Mountain Pass	USA	Handpicked	1-10		7.2 (24 hours)	-water		Electrophoresis	1980	Smith and Steiner 1980 [80]

Table A5. Published studies on the surface behaviour investigations into bastnäsite. Purity column uses the description of purity stated within the reference. Blanks within the column are due to the information not being stated within the referenced material. Gaps in the table correspond to where literature does not specify details. For results from Pradip (2015) the 'also' between values of electrolytes denotes that the study conducted two experiments with different electrolytes.

Bibliography

[1] A. R. Chakhmouradian and F. Wall, “Rare earth elements: minerals, mines, magnets (and more),” *Elements,* vol. 8, no. 5, pp. 33-340, 2012.

[2] G. P. Hatch, “Dynamics in the global market for rare earths,” *Elements,* vol. 8, no. 5, pp. 341-346, 2012.

[3] F. Wall, A. Rollat and R. Pell, “Responsible sourcing of critical metals,” *Elements,* vol. 13, no. 5, pp. 313-8, 2017.

[4] K. Goodenough, F. Wall and D. Merriman, “The Rare Earth Elements: Demand, Global Resources, and Challenges for Resourcing Future Generations,” *Nat. Resour. Res.,* vol. 27, no. 2, pp. 1-16, 2017.

[5] A. Jordens, Y. P. Cheng and K. E. Waters, “A review of the beneficiation of rare earth element bearing minerals,” *Miner. Eng.,* vol. 41, pp. 97-114, 2013.

[6] X. Yang, J. V. Satur, K. Sanematsu, J. Laukkanen and T. Saastamoinen, “Beneficiation sutdies of a complex REE ore,” *Miner. Eng.,* vol. 71, pp. 55-64, 2015.

[7] E. Espiritu, S. Naseri and K. Waters, “Surface chemistry and flotation behaviour of dolomite, monazite and bastnasite in the presence of benzohydroxamate, sodium oleate and phosphoric acid ester collectors.,” *Colloid Surf., A,* vol. 546, pp. 254-265, 2018.

[8] U. G. Survey, “Mineral commodity summaries,” US Geological Survey , 2016.

[9] Al Ali S, “Mineralogy and mineral processing to optimise recovery of synchysite (Ce) and apatite from carbonatite at Songwe Hill, Malawi,” *PhD Thesis, University of Exeter, UK,* 2016.

[10] S. Al-Ali, W. F, R. Sheridan, J. Pickles and R. Pascoe, “Magnetic properties of REE fluorcarbonate minerals and implications for minerals processing,” *Miner. Eng.,* vol. 131, pp. 392-397, 2019.

[11] J. M. Hughes, “The many facets of apatite,” *Am. Mineral.,* vol. 100, pp. 1033-1039, 2015.

[12] L. A. Barros, E. E. Ferreira and A. E. Peres, “Floatability of apatites and gangue minerals of an igneous phosphate ore,” *Miner. Eng.,* vol. 21, pp. 994-999, 2008.

[13] R. Houot, “Beneficiation of phosphatic ores through flotation: review of industrial applications and potential developments,” *Int. J. Mineral. Process,* vol. 9, pp. 353-384, 1982.

[14] L. O. Filippov, D. A., I. V. Filippova, H. Kasaini and J. Thiry, “Selective flotation of silicates and Ca bearing minerals: The role of non-ionic reagent on cationic flotation,” *Miner. Eng.,* vol. 36, pp. 314-323, 2012.

[15] B. Babel and M. Rudolph, “Characterizing mineral wettabilities on a microscale by colloid probe atomic force microscopy,” *Miner. Eng.,* vol. 121, pp. 212-219, 2018.

[16] M. Rudolph and U. Peuker, “Mapping hydrophobicity combining AFM and Raman spectroscopy,” *Miner. Eng. ,* vol. 66, pp. 181-190, 2014.

[17] S. Lou, Z. Ouyang, Y. Zhang, X. Li, J. Hu, M. Li and F. Yang, “Nanobubbles on solid surface image by atomic force microscopy,” *J. Vac. Sci. Technol., B: Microelectron. Nanometer Struct.--Process., Meas., Phenom,* vol. 18, no. 5, pp. 2573-2575, 2000.

[18] D. Lohse and X. Zhang, “Surface nanobubbles and nanodroplets,” *Rev. Mod. Phys. ,* vol. 87, no. 3, p. 981, 2015.

[19] X. Zhang, N. Maeda and V. Craig, “Physical properties of nanobubbles on hydrophobic surfaces in water and aqueous solutions,” *Langmuir,* vol. 22, no. 11, pp. 5025-5035, 2006.

[20] S. Calgaroto, K. Wilberg and J. Rubio, “On the nanobubbles interfacial properties and future applications in flotation,” *Miner. Eng.,* vol. 60, pp. 33-40, 2014.

[21] J. Weijs and D. Lohse, “Why surface nanobubbles live for hours,” *Phys. Rev. Lett.,* vol. 110, no. 5, p. 054501, 2013.

[22] J. Seddon and D. Lohse, “Nanobubbles and micropancakes: gaseous domains in immersed substrates.,” *J. Phys.: Condens. Matter,* vol. 23, no. 13, p. 13301, 2011.

[23] X. Wang, B. Zhao, W. Ma, W. Y., X. Gao, R. Tai, X. Zhou and L. Zhang, “Interfacial nanobubbles on atomically flat substrates with different hydrophobicities,” *Chem. Phys. Chem.,* vol. 16, no. 5, pp. 1003-1007, 2015.

[24] B. Tan, H. An and C. Ohl, “Surface nanobubbles are stabilized by hydrophobic attraction,” *Phys. Rev. Lett.,* vol. 120, no. 16, p. 164502, 2018.

[25] B. Tan, H. An and C. Ohl, “Stability, dynamics, and tolerance to undersaturation of surface nanobubbles,” *Phys. Rev. Lett.,* vol. 122, no. 13, p. 134502, 2019.

[26] L. Wang, X. Wang., L. Wang, J. Hu, C. Wang, B. Zhao, X. Zhang, R. Tai, M. He, L. Chen and L. Zhang, “Formation of surface nanobubbles on nanostructured substrates.,” *Nanoscale,* vol. 9, no. 3, pp. 1078-1086, 2017.

[27] A. Agrawal, J. Park, D. Ryu, P. Hammond, T. Russell and G. McKinley, “Controlling the location and spatial extent of nanobubbles using hydrophobically patterned surfaces.,” *Nano Lett.,* vol. 5, no. 9, pp. 1751-1756, 2005.

[28] F. Wall, “Rare earth elements,” *Critical metals handbook,* pp. 312-339, 2014.

[29] S. Zhang, Y. Ding, B. Liu and C. C. Chang, “Supply and demand of some critical metals and present status of their recycling in WEE,,” *Waste Management,* vol. 65, pp. 113-127, 2017.

[30] F. Wall and C. Owens, “The Critical West: raw materials and rare earths.,” in *Proceedings of the Open University Geological Society*, Exeter, UK, 2017.

[31] A. R. Chakhmouradian, E. P. Reguir, A. N. Zaitsev, C. Coueslan, C. Xu, J. Kynicky, A. H. Mumin and P. Yang, “Apatite in carbonatitic rocks:

Compositional variatin, zoning, element partitioning and petrogenetic significance," *Lithos,* vol. 274, pp. 188-213, 2017.

[32] J. D. Grice and G. Y. Chao, "Horvathite-(Y), rare earth-fluorocarboante, a new mineral species from Mont Saint-Hilaire, Quebec,," *Can. Mineral.,* vol. 35, pp. 734-749, 1997.

[33] J. D. Grice and G. Y. Gao, "Lukechangite-(Ce), a new rare-earth fluorocarbonate mineral from Mont Saint-Hilaire, Quebec.," *Am. Mineral.,* vol. 82, pp. 1255-1260, 1997.

[34] D. Holtstam and U. Andersson, "The REE minerals of the Bastnas-type deposits, South Central Sweden,," *Can. Mineral.,* vol. 45, pp. 1073-1114, 2007.

[35] A. V. Mokhov, P. M. Kartashov, O. A. Bogatikov, N. A. Ashikhmina, L. O. Magazina and E. V. Koporulina, "Fluorite, hachettolite, calcium sulfate and bastnasite-(Ce) in the lunar regolith from Mare Crisium," *Dokl. Earth Sci.,* vol. 422, pp. 1178-1180, 2008.

[36] M. M. Muller, H. J. Kleebe, S. Lauterbach and G. Zito, "Crystallographic orientation relationship between bastnaesite, fluocerite and cerianite observed in a crystal from the pikes peak pegmatites," *Zeitschrift fur Kristallographie- Crystalline Materials,* vol. 226, pp. 467-475, 2011.

[37] G. Donnay and J. Donnay, "The crystallography of bastnaesite, parisite, roentgenite and synchysite.," *Am. Mineral.,* vol. 38, pp. 932-963, 1953.

[38] P. Bayliss and A. A. Levinson, "A system of nomenclature for rare-earth mineral species: revision and extension,," *Am. Mineral.,* vol. 73, pp. 422-423, 1988.

[39] J. Van Landuyt and S. Amelinckx, "Multiple beam direct lattice imaging of new mixed layer compounds of the bastnasite-synchysite series of minerals.," *Am. Mineral.,* vol. 60, no. 5-6, pp. 351-358, 1975.

[40] T. R. Manfredi, "A mineralizacao de parisita-(Ce) associado ao carbonatito Fazenda Varela.," *Masters thesis. Universidade Federal Do Rio Grande Do Sul Instituto de Geosciencias,* 2013.

[41] Y. Ni, J. M. Hughes and A. N. Mariano, "The atomic arrangement of bastnasite- (Ce) Ce(CO3)F, and structural elements of synchysite-(Ce), rontgenite-(Ce), and parisite-(Ce);," *Am. Mineral.,* vol. 78, pp. 415-418, 1993.

[42] K. Michiba, R. Miyawaki, T. Minakawa, Y. Terada, I. Nakai and S. Matsubara, "Crystal structure of hydroxylbastnasite-(Ce) from Kamihouri, Miyazaki Prefecture, Japan," *J. Mineral. Petrol. Sci.,* vol. 108, no. 6, pp. 326-334, 2013.

[43] M. Baijot, F. Hatert, F. Dal Bo and S. Philippo, "Mineralogy and petrography of phosphate mineral associations from the Jacao Pegmatite, Minas Gerais, Brazil," *Can. Mineral.,* vol. 52, no. 2, pp. 373-397, 2014.

[44] F. H. B. Tallarico, N. J. McNaughton, D. I. Groves, I. R. Fletcher, B. R. Figueiredo, J. B. Carvalho, J. L. Rego and A. R. Nunes, "Geological and SHRIMP II U-Pb constraits on the age and origin of the Breves Cu-Au(W-Bi-Sn) deposit, Carajas, Brazil," *Miner. Deposita,* vol. 39, no. 1, pp. 68-86, 2004.

[45] M. V. Lupulescu, J. M. Hughes, J. R. Chiarenzelli and D. G. Bailey, "Texture, Crystal Structure, and Composition of Fluorapatites From Iron

oxide apatite(Ioa) Deposits, Eastern Adirondack Mountains, New York," *Can. Mineral.,* vol. 55, no. 3, pp. 399-417, 2017.

[46] S. Broom-Fendley, M. Styles, J. Appleton, G. Gunn and F. Wall, "Evidence for dissolution reprecipitation of apatite and preferential LREE mobility in carbonatite- derived late stage hydrothermal processes," *Am. Mineral.,* vol. 101, no. 3, pp. 596-611, 2016.

[47] B. Reynard, C. Lecuyer and P. Grandjean, "Crystal-chemical controls on rare-earth element concentrations in fossil biogenic apatites and implications for paleoenvironmental reconstructions," *Chem. Geol.,* vol. 155, no. 3, pp. 233-241, 1999.

[48] J. M. Hughes, M. Cameron and A. Mariano, "Rare earth ordering and structural variations in natural rare earth bearing apatites," *Am. Mineral.,* vol. 76, pp. 1165-1173.

[49] R. Oberti, L. Ottolini, V. G.D. and G. Parodi, "On the symmetry and crystal chemistry of britholite: New structural and microanalytical data," *Am. Mineral.,* vol. 86, no. 9, pp. 1066-1075, 2001.

[50] F. Soltani, M. Abdollahy, S. M. Javad Koleini and D. Moradkhani, "Selection of an appropriate leaching method for light REEs from Esfordi flotation concentration based on mineral characterization.," *J. South. Afr. Inst. Min. Metall.,* vol. 117, no. 5, p. 443, 2017.

[51] H. M. Harbi, A. A. Eldougdoug and M. S. El-Shahawi, "Mineral processing and extraction of rare earth elements from the Wadi Khamal Nelsonite Ore, Northwestern Saudi Arabia," *Arabian J. Geosci.,* vol. 4, pp. 353-363, 2011.

[52] S. S. Serdyuk, V. G. Lomayev, V. I. Kuzmin, D. S. Flett, N. V. Gudkova, D. V. Kuzmin, M. A. Mulagaleeva, V. N. Kuzmina, S. N. Kalyakin and O. A. Logutenko, "The Chuktukon niobium-rare earth metals deposit: Geology and investigation into the processing options of the ores.," *Miner. Eng. ,* vol. 113, pp. 8-14, 2017.

[53] A. Jordens, R. S. Sheridan, N. A. Rowson and K. E. Waters, "Processing a rare earth mineral deposit using gravity and magnetic separation.," *Miner. Eng.,* vol. 62, pp. 9-18, 2014.

[54] N. Krishnamurthy and C. K. Gupta, Extractive metallurgy of rare earths, Taylor Francis, 2015.

[55] K. K. Keekan, J. C. Jalondhara and Abhilash, "Extraction of Ce and Th from Monazite Using REE Tolerant Aspergillus niger," *Miner. Process. Extr. Metall. Rev.,* vol. 38, no. 5, pp. 312-320, 2017.

[56] M. K. Corbett, J. J. Eksteen, X. Z. Niu, J. P. Croue and E. L. Watkin, "Interactions of phosphate solubilising microorganisms with natural rare-earth phosphate minerals: a study utilizing the Western Australian monazite," *Bioprocess and Biosystems: Engineering,* vol. 40, no. 6, pp. 929-942, 2017.

[57] A. Jordens, C. Marion, O. Kuzmina and K. E. Waters, "Surface chemistry considerations in the flotation of bastnasite," *Miner. Eng.,* vol. 66, pp. 119-129, 2014.

[58] S. Chelgani, M. Rudolph, T. Leistner, J. Gutzmer and U. A. Peuker, "A review of rare earth minerals flotation: monazite and xenotime.," *International Journal of Mining and Science and Technology,* vol. 25, no. 6, pp. 877-883, 2015.

[59] Fuestenau D W, *Trans AIME ,* vol. 208, p. 1365, 1957.

[60] W. Fuerstenau and Pradip, “Zeta potentials in the flotation of oxide and silicate minerals,,” *Adv. Colloid. Interface Sci.,* vol. 114, pp. 9-26, 2005.

[61] L. Xu, T. Peng, J. Tian, Z. Lu, Y. Hu and W. Sun, “Anisotropic surface physicochemical properties of spodumene and albite crystals: Implications for flotation separation,” *Appl. Surf. Sci.,* vol. 426, pp. 1005-1022, 2017.

[62] D. Azizi and F. Larachi, “Surface interactions and flotation behavior of calcite, dolomite and ankerite with alkyl hydroxamic acid bearing collector and sodium silicate.,” *Colloids Surf., A,* vol. 537, pp. 126-138, 2018.

[63] M. Kosmulski, “IEP as a parameter characterizing the pH dependent surface charging of minerals other than metal oxides,” *Adv. Colloid Inteface Sci.,* vol. 171, pp. 77-86, 2012.

[64] A. V. Delgado, F. Gonzalez- Caballero, R. J. Hunter, L. Koopal and J. Lyklema, “Measurement and interpretation of electrokinetic phenomena(IUPAC technical report),” *Pure Applied Chemistry,* vol. 77, no. 10, pp. 1753-1805, 2005.

[65] Hunter R J, Zeta potentials in colloid science: principles and applications, Vol 2. ed., New York: Academic press, 2013.

[66] D. W. Fuestenau, Pradip and R. Herrera-Urbina, “The surface chemistry of bastaesite, barite and calcite in aqueous carbonatite solutions.,” *Colloid Surf., A,* vol. 68, pp. 95-102, 1992.

[67] R. Greenwood, “Review of the measurement of zeta potentials in concentrated aqueous suspensions using electroacoustics,” *Adv. Colloid Interface Sci.,* vol. 106, pp. 55-81, 2003.

[68] R. Houot, J. P. Cuif, Y. Mottot and J. C. Samama, “Recovery of Rare Earth Minerals with Emphasis on Flotation Process.,” *International Conference on Rare Earth Minerals and Minerals for Electronic uses.,* pp. 301-324, 1991.

[69] M. Kosmulski, “The pH dependant surface charging and points of zero charge. VI. Update,” *J. Colloid Interface Sci.,* vol. 426, pp. 209-212, 2014.

[70] D. Fuestenau and J. Shibata, “On using electrokinetics to interpret the flotation and interfacial behavior of maganese dioxide,” *Int. J. Miner. Process.,* vol. 57, pp. 205-217, 1999.

[71] D. Azizi, A. Sarvaramini and F. Larachi, “Liquid-liquid mineral separation via ionic-liquid complexation of monazite and bastnasite- An alternative route for rare-earth mineral beneficiation,” *Colloids Surf., A,* vol. 520, pp. 301-323, 2017.

[72] A. Saravaramini, D. Azizi and F. Larachi, “Hydroxamic acid interactions with solvated cerium hydroxides in the flotation in the flotation of monazite and bastnasite- Experiments and DFT study,” *Appl. Surf. Sci.,* vol. 387, pp. 986-995, 2016.

[73] W. Liu, X. Wang, Z. Wang and J. D. Miller, “Flotation chemistry features in bastnaesite flotation with potassium lauryl phosphate,” *Miner. Eng.,* vol. 85, pp. 17-22, 2016.

[74] D. Azizi, F. Larachi and M. Latifi, “Ionic-liquid collectors for rare earth minerals flotation: Case of tetrabutylammonium bis(2-ethylhexyl) -

phosphate for monazite and bastnasite recovery,," *Colloids Surf., A.,* vol. 506, pp. 74-86, 2016.

[75] C. D. Anderson, "Improved understanding of rare earth surface chemistry and its application to froth flotation," *PhD thesis, Colorado School of Mines,* 2015.

[76] F. Zhou, L. X. Wang, Z. H. Xu, Q. X. Liu and R. A. Chi, "Interaction of reactive oily bubble in flotation of bastnaesite.," *J. Rare Earth,* vol. 32, pp. 772-778, 2014.

[77] J. Ren, S. Song and A. Lopez-Valdivesco, "Selective flotation of bastnaesite from monazite in rare earth concentrates using potassium alum as depressant.," *Int. J. Miner. Process.,* vol. 59, no. 3, pp. 237-245, 2000.

[78] J. Ren, S. Lu, S. Song and J. Niu, "A new collector for rare earth mineral flotation.," *Miner. Eng.,* vol. 10, no. 12, pp. 1395-1404, 1997.

[79] O. Pavez, P. R. G. Brandao, Peres and A E C, "Adsorption of oleate and octyl-hydroxamate on to rare-earth minerals," *Miner. Eng.,* vol. 9, no. 3, pp. 357-366, 1996.

[80] R. W. Smith and S. D. Steiner, "Autoactivation in anionic flotation of bastanaesite,," *Solids Separation Processes, Institute of Chemical Engineers Symposium Series,* vol. 4, pp. 1-12, 1980.

[81] A. N. Mariano and A. Mariano, "Rare earth mining and exploration in North America," *Elements,* vol. 8, no. 5, pp. 369-376, 2012.

[82] R. W. Smith and D. Shonnard, "Electokinetic study of the role of modifying agents in flotation of salt-type minerals," *AIChE Journal,* vol. 32, pp. 865-868, 1986.

[83] R. Herrera-Urbina, Pradip and D. W. Fuerstenau, "Electrophoretic moblity and computations of solid-acqueous solution equilibria for the bastaesite H 2O system," *Miner. Metall. Process,* vol. 30, pp. 18-23, 2013.

[84] Pradip, C. C. Li and D. W. Fuerstenau, "Surface chemical characterization of bastnaesite through electrokinetics," *KONA Powder Part J.,* vol. 32, pp. 176-183, 2015.

[85] J. Nduwa-Mushidi and C. Anderson, "Surface chemistry and flotation behaviours of Monazite-Apatite-Ilmenite-Quartz-Rutile-Zircon with octanohydroxamic acid," *Journal of Sustainable Metallurgy,* vol. 3, no. 1, p. 62, 2017.

[86] R. Cheng, C. Li, X. Liu and S. Deng, "Synergism of octane phenol polyoxyethylene-10 and oleic acid in apatite flotation," *Physicochemical Problems in Mineral Processing,* vol. 53, no. 2, pp. 1214-1227, 2017.

[87] J. Yu, Y. Ge, W. Guo and X. Guo, "Flotation collophane from high-iron phosphate ore by using sodium ligninsulfonate as depressant," *Sep. Sci. Technol.,* vol. 52, no. 3, pp. 557-566, 2017.

[88] X. Li, Q. Zhang, B. Hou, J. Ye, S. Mao and X. Li, "Flotation separation of quartz from collophane using an amine collector and its adsorption mechanisms," *Powder Technol.,* vol. 318, pp. 224-229, 2017.

[89] J. Yu, Y. Ge, X. Guo and W. Guo, "The depression effect and mechanism of NSFC on dolomite in the flotation of phosphate ore.," *Sep. Purif. Technol,* vol. 161, pp. 88-95, 2016.

[90] J. Yu, Y. Ge and J. Hou, “Behaviour and mechanism of collophane and dolomite separation using alkyl hydroxamic acid as a flotation collector,” *Physicochem. Probl. Miner. Process.,* vol. 52, p. 155, 2016.

[91] F. Zhou, L. Wang, Z. Xu, Q. Liu and R. Chi, “Reactive oily bubble technology for flotation of apatite, dolomite and quartz,” *Int J Miner Process,* vol. 134, p. 74, 2015.

[92] A. P. L. Nunes, A. E. C. Peres and G. E. S. Valadao, “The influence of lattice ions on the electrokinetic potential of primary and secondary phosphates,” *Sep. Sci. Technol.,* vol. 50, no. 13, pp. 2023-2031, 2015.

[93] I. V. Filippova, L. Filippov, D. A and S. VV, “Synergetic effect of a mixture of anionic and nonionic reagents: Ca mineral contrast separation flotation at neutral pH,” *Miner. Eng.,* vol. 66, pp. 135-144, 2014.

[94] H. Yang, Q. Tang, C. Wang and J. Zhang, “Flocculation and flotation response of Rhodococcus erythropolis to pure minerals in hematite ores,” *Miner. Eng.,* vol. 45, pp. 67-72, 2013.

[95] J. Kou, D. Tao and G. Xu, “Fatty acid collectors for phophate flotation and their adsorption behaviour using QCM-D.,” *Int. J. Mineral. Process.,* vol. 95, no. 1, pp. 1-9, 2010.

[96] C. Chairat, E. H. Oelkers, J. Schott and J. E. Lartigue, “Fluorapatite surface composition in aqueous solution deduced from potentiometric, electrokinetic, and solubility measurements, and spectroscopic observations,” *Geochim Cosmochim Acta,* vol. 71, p. 5888, 2007.

[97] Y. Hue, R. Chi and Z. Xu, “Solution chemistry study of salt-type mineral flotation systems:role of inorganic dispersants,” *Ind Eng Chem Res,* vol. 42, p. 1647, 2003.

[98] Y. Hu and Z. Xu, “Interactions of amphoteric amino phosphoric acids with calcium containing minerals and selective flotation,” *Int. J. Mineral. Process.,* vol. 72, no. 1, pp. 87-94, 2003.

[99] J. Perrone, B. Fourest and E. Giffaut, “Surface characterization of synthetic and mineral carbonate fluorapatites,” *J. Colloid Interface Sci.,* vol. 249, no. 2, pp. 441-452, 2002.

[100] S. Simukanga and W. Lombe, “Electrochemical properties of apatite and other minerals of Zambian phosphate ores in aqueous solution,” *Nutr. Cycl. Agroecosyst.,* vol. 41, p. 159, 1995.

[101] K. H. Rao, B. M. Anitti and E. Forssberg, “Mechanism of oleate interactions on salt type minerals, part II. Adsorption and electrokinetic studies of apatite in the presence of sodium oleate and sodium metasilicate.,” *Int. J. Mineral. Process.,* vol. 28, no. 1-2, pp. 59-79, 1990.

[102] S. K. Mishra, “Electrokinetic properties and flotation behaviour of apatite and calcite in the presence of sodium oleate and sodium metasilicate.,” *Int. J. Miner. Process.,* vol. 9, no. 1, pp. 59-73, 1982.

[103] S. K. Mishra, “The electrokinetics of apatite and calcite in inorganis electrolyte environment.,” *International Journal of Minerals Engineering,* vol. 5, no. 1, pp. 69-83, 1978.

[104] R. Arieli, “Nanobubbles form at active hydrophobic spots on the luminal aspect of blood vessels: consequences for decompression illness in diving and possible implications for autoimmune disease- an overview,” *Frontiers in Physiology ,* vol. 8, p. 591, 2017.

[105] P. Bhandari, G. Novikova, C. Goergen and J. Irudayaraj, “Ultrasound beam steering of oxygen nanobubbles for enhanced bladder cancer therapy.,” *Sci. Rep.,* vol. 8, p. 3112, 2018.

[106] Q. Li, J. Froning, M. Pykal, S. Zhang, Z. Wang, M. Vondrak, P. Benas, K. Cepe, P. Jurecka, J. Sponer and R. Zbonl, “RNA nanopatterning on graphene,” *2D Mater.,* vol. 5, no. 3, p. 031006, 2018.

[107] C. Melios, C. Giusca, V. Panchal and O. Kazakova, “Water on graphene: review of recent progress,” *2D Mater.,* vol. 5, no. 2, p. 022001, 2018.

[108] N. Ishida, T. Inoue, M. Miyahara and K. Higashitani, “Nanobubbles on a hydrophobic surface in water observed by tapping-mode atomic force microscopy,” *Langmuir,* vol. 16, no. 16, pp. 6377-6380, 2000.

[109] P. Epstein and M. Plessset, “On the stability of gas bubbles in liquid gas solutions,” *J. Chem. Phys.,* vol. 18, no. 11, pp. 1505-1509, 1950.

[110] M. Alheshibri, J. Qian, M. Jehannin and V. Craig, “A history of nanobubbles,” *Langmuir,* vol. 32, no. 43, pp. 11086-11100, 2016.

[111] H. Teshima, T. Nishiyama and K. Takahashi, “Nanoscale pinning effect evaluated from deformed nanobubbles,” *J. Chem. Phys. ,* vol. 146, no. 1, p. 014708, 2017.

[112] D. Lohse and X. Zhang, “Pinning and gas oversaturation imply stable single surface nanobubbles,” *Phys. Rev. E,* vol. 91, no. 3, p. 031003, 2015.

[113] L. Xie, Doctoral Thesis, University of Alberta , 2017.

[114] B. Tan, H. An and C. Ohl, “Resolving the pinning force of nanobubbles with optical microscopy,” *Phys. Rev. Lett.,* vol. 118, no. 5, p. 054501, 2017.

[115] E. White, M. Mecklenburg, S. Singer, S. Aloni and B. Regan, “Imaging nanobubbles in water with scanning transmission electron microscopy,” *Appl. Phys. Express,* vol. 4, no. 5, p. 055201, 2011.

[116] S. Karpitschka, E. Dietrich, J. Seddon, H. Zandvliet, D. Lohse and H. Riegler, “Nonintrusive optical visualization of surface nanobubbles,” *Phys. Rev. Lett.,* vol. 109, no. 6, p. 066102, 2012.

[117] C. Chan and C. Ohl, “Surface Nanobubble Nucleation Visualized with TIRF Microscopy,” *arXiv preprint,* 2012.

[118] G. Binnig, C. Quate and C. Gerber, “Atomic force microscope,” *Phys. Rev. Lett.,* vol. 56, no. 9, p. 930, 1986.

[119] M. Allen, E. Bradbury and R. Balhorn, “AFM analysis of DNA-protomine complexes bound to mica,” *Nucleic Acids Res.,* vol. 25, no. 11, pp. 2221-2226, 1997.

[120] M. Rudolph and U. Peuker, “Hydrophobicity of minerals determined by atomic force microscopy- a tool for flotation research,” *Chem. Ing. Tech. ,* vol. 86, no. 6, pp. 865-873, 2014.

[121] N. Jalili and K. Laxminarayana, “A review of atomic force microscopy imaging systems: application to molecular metrology and biological sciences,” *Mechatronics,* vol. 14, no. 8, pp. 907-945, 2004.

[122] G. Zavala, “Atomic force microscopy: a tool for characterization, synthesis and chemical processes,” *Colloid Polym. Sci.,* vol. 286, no. 1, pp. 85-95, 2008.

[123] X. Xue-Hua, L. Gang, W. Zhi-Hua, Z. Xiao-Dong and H. Jun, “Effect of temperature on the morphology of nanobubbles at the mica/water interface,” *Chin. Phys.,* vol. 14, no. 9, p. 1774, 2005.

[124] H. Liao, C. Yang, H. Ko, E. Hwu and S. Hwang, “Imaging initial formation processes of nanobubbles at the graphite-water interface through high-speed atomic force microscopy,” *Appl. Surf. Sci.,* vol. 434, pp. 913-917, 2018.

[125] Y. Wang, X. Li, S. Ren, H. Alem, L. Yang and D. Lohse, “Entrapment of interfacial nanobubbles on nano-structured surfaces,” *Soft Matter,* vol. 13, no. 32, pp. 5381-5388, 2017.

[126] C. Chan and C. Ohl, “Total-internal-reflection-fluorescence microscopy for the study of nanobubble dynamics,” *Phys. Rev. Lett.,* vol. 109, no. 17, p. 174501, 2012.

[127] C. Chan, M. Arora and C. Ohl, “Coalescence, growth, and stability of surface-attached nanobubbles,” *Langmuir,* vol. 31, no. 25, pp. 7041-7046, 2015.

[128] J. Jin, Z. Feng, F. Yang and N. Gu, “Bulk Nanobubbles Fabricated By Repeatedly Compression of Microbubbles,” *Langmuir,* vol. 35, no. 12, pp. 4238-4245, 2019.

[129] X. Zhang, A. Quinn and W. Ducker, “Nanobubbles at the Interface between Water and a Hydrophobic Solid,” *Langmuir,* vol. 24, no. 9, pp. 4756-4764, 2008.

[130] S. German, X. Wu, H. An, V. Craig, T. Mega and X. Zhang, “Interfacial nanobubbles are leaky: Permeability of the gas/water interface,” *ACS Nano,* vol. 8, no. 6, pp. 6193-6201, 2014.

[131] M. Switkes and J. Ruberti, “Rapid cryofixation/freeze fracture for the study of nanobubbles at the solid-liquid interfaces,” *Appl. Phys. Lett.,* vol. 84, no. 23, pp. 4759-4761, 2004.

[132] X. Zhang, “Quartz crystal microbalance study of the interfacial nanobubbles,” *Phys. Chem. Chem. Phys.,* vol. 10, no. 45, pp. 6842-6848, 2008.

[133] R. Berkelaar, E. Dietrich, G. Kip, E. Kooji, H. Zandvliet and D. Lohse, “Exposing nanobubble-like objects to a degassed environment,” *Soft Matter,* vol. 10, no. 27, pp. 4947-4955, 2014.

[134] J. Seddon, E. Kooji, B. Poelsema, H. Zandvliet and D. Lohse, “Surface Bubble Nucleation Stability,” *Phys. Rev. Lett. ,* vol. 106, no. 5, p. 05610, 2011.

[135] X. Zhang, X. Zhang, S. Lou, Z. Zhang, J. Sun and J. Hu, “Degassing and temperature effects on the formation of nanobubbles at the mica/water interface,” *Langmuir,* vol. 20, no. 9, pp. 3813-3815, 2004.

[136] R. Berkelaar, J. Seddon, H. Zandvliet and D. Lohse, “Temperature dependence of surface nanobubbles,” *Chem. Phys. Chem.,* vol. 13, no. 8, pp. 2213-2217, 2012.

[137] J. Millare and B. A. Basilia, “Nanobubbles from Ethanol-Water Mixtures: Generation and Solute Effects via Solvent Replacement Methods,” *ChemistrySelect,* vol. 31, no. 3, pp. 9268-9275, 2018.

[138] M. A. Hampton, B. Donose and A. Nguyen, “Effect of alcohol-water exchange and surface scanning on nanobubbles and the attraction

between hydrophobic and hydrophilic surfaces," *J. Colloid Interface Sci.,* vol. 325, no. 1, pp. 267-274, 2008.

[139] Z. Zou, N. Quan, X. Wang, S. Wang, L. Zhou, J. Hu, L. Zhang and Y. Dong, "The properties of surface nanobubbles formed on different substrates," *Chin. Phys. B,* vol. 27, p. 086803, 2018.

[140] Q. Xiao, Y. Liu, Z. Guo, Z. Liu, D. Lohse and X. Zhang, "Solvent exchange leading to nanobubble nucleation: A molecular dynamics study," *Langmuir,* vol. 33, no. 32, pp. 8090-8096, 2017.

[141] Q. Chen, L. L., H. Faraji, S. Feldberg and H. White, "Electrochemical measurements of single H2 nanobubble nucleation and stability at Pt nanoelectrodes," *J. Phys. Chem. Lett.,* vol. 5, no. 20, pp. 3539-3544, 2014.

[142] K. Kikuchi, S. Nagata, Y. Tanaka, Y. Sihara and Z. Ogumi, "Characteristics of hydrogen nanobubbles in solutions obtained with water electrolysis," *J. Electroanal. Chem.,* vol. 600, no. 2, pp. 303-310, 2007.

[143] S. Yang, P. Tsai, E. Kooij, A. Prosperetti, H. Zandvliet and D. Lohse, "Electrolytically generated nanobubbles on highly orientated pyrolytic graphite surfaces," *Langmuir,* vol. 25, no. 3, pp. 1466-1474, 2009.

[144] L. Zhang, Y. Zhang, X. Zhang, Z. Li, G. Shen, M. Ye, C. Fan, H. Fang. and J. Hu, "Electrochemically controlled formation and growth of hydrogen nanobubbles," *Langmuir,* vol. 22, no. 19, pp. 8109-8113, 2006.

[145] A. Soto, S. German, H. Ren, D. Van Der Meer, D. Lohse, M. Edwards and H. White, "The nucleation rate of single O2 nanobubbles at Pt nanoelectrodes," *Langmuir,* vol. 34, no. 25, pp. 7309-7318, 2018.

[146] S. German, Q. Chen, M. Edwards and H. White, "Electrochemical Measurement of Hydrogen and Nitrogen Nanobubble Lifetimes at Pt Nanoelectrodes.," *J. Electrochem. Soc.,* vol. 163, no. 4, pp. 3160-3166, 2016.

[147] J. Seddon, D. Lohse, W. Ducker and V. Craig, "A deliberation of nanobubbles at surfaces and in bulk," *Chem. Phys. Chem.,* vol. 13, no. 8, pp. 2179-2187, 2012.

[148] J. Qui, Z. Zou, S. Wang, X. Wang, L. Wang, Y. Dong, H. Zhao, L. Zhang and J. Hu, "Formation and stability of bulk nanobubbles generated by ethanol-water exchange," *Chem. Phys. Chem.,* vol. 18, no. 10, pp. 1345-1350, 2017.

[149] N. Nirmalkar, A. Pacek and M. Bariqou, "On the existence and stability of bulk nanobubbles," *Langmuir,* vol. 34, no. 37, pp. 10964-10973, 2018.

[150] X. Zhang, X. Zhang, J. Sun, Z. Zhang, G. Li, H. Fang, X. Xiao, X. Zeng and J. Hu, "Detection of novel gaseous states at the highly oriented pyrolytic graphite-water interface," *Langmuir,* vol. 23, no. 4, pp. 1178-1783, 2007.

[151] H. An, G. Liu and V. Craig, "Wetting of nanophases: Nanobubbles, nanodroplets and micropancakes on hydrophobic surfaces," *Adv. Colloid Interface Sci.,* vol. 222, pp. 9-17, 2015.

[152] H. An, B. Tan and C. Ohl, "Distinguishing nanobubbles from nanodroplets with AFM: the influence of vertical and lateral imaging forces.," *Langmuir,* vol. 32, no. 48, pp. 12710-12715, 2016.

[153] C. Chan, L. Chen, M. Arora and C. Ohl, “Collapse of surface nanobubbles,” *Phys. Rev. Lett.,* vol. 114, no. 11, p. 114505, 2015.

[154] H. Ko, W. Hsu, C. Yang, C. Fang, Y. Lu and I. Hwang, “High-resolution characterization of preferential gas adsorptionat the graphene-water interface,” *Langmuir,* vol. 32, no. 43, pp. 11164-11171, 2016.

[155] L. Ditscherlein, J. Fritzsche and U. Peuker, “Study of nanobubbles on hydrophilic and hydrophobic alumina surfaces,” *Colloids Surf., A,* vol. 497, pp. 242-250, 2016.

[156] B. Wills and J. Finch, Wills' mineral processing technology: an introduction to the practical aspects of ore treatment and mineral recovery, Butterworth-Heinemann, 2015.

[157] S. R. Rao, Surface Chemistry of Froth flotation: Volume : Fundamentals, Springer Science & Business Media, 2013.

[158] N. Ahmed and G. Jameson, “The effect of bubble size on the rate of flotation of fine particles,” *Int. J. Miner. Process.,* vol. 14, no. 3, pp. 195-215, 1985.

[159] H. Schubert, “Nanobubbles, hydrophobic effect, heterocoagulation and hydrodynamics in flotation,” *Int. J. Mineral. Process. ,* vol. 78, no. 1, pp. 11-21, 2005.

[160] A. Sobhy and D. Tao, “Nanobubble column flotation of fine coal particles and assocatiated fundamentals.,” *J. Miner. Process. ,* vol. 124, pp. 109-116, 2013.

[161] Y. Tao, J. Liu, S. Yu and D. Tao, “Picobubble enhanced fine coal flotation,” *Sep. Sci. Technol.,* vol. 41, no. 16, pp. 3597-3607, 2006.

[162] A. Rosa and J. Rubio, “On the role of nanobubbles in particle-bubble adhesion for the flotation of quartz and apatitic minerals.,” *Miner. Eng. ,* vol. 127, pp. 178-184, 2018.

[163] Y. Mikhlin, A. Karacharov and M. Likhatski, “Effect of adsorption of butyl xanthate on galena, PbS, and HOPG surfaces as studied by atomic force microscopy and spectroscopy and XPS,” *Int. J. Mineral. Process.,* vol. 144, pp. 81-89, 2015.

[164] T. Stark, I. Silin and H. Wotruba, “Mineral processing of eudialyte ore from Norra Karr,” *Journal of Sustainable Metallurgy,* vol. 3, no. 1, pp. 32-38, 2017.

[165] A. Borst, H. Friis, T. Nielsen and T. Waight, “Bulk and mush melt evolution in agpaitic intrusions: Insights from compositional zoning in eudialyte, Ilimaussaq complex, South Greenland,” *J. Petrol.,* vol. 59, no. 4, pp. 589-612, 2018.

[166] V. Vaccarezza and C. Anderson, “Beneficiation and Leaching Study of Norra Karr Eudialyte Mineral,” in *TMS Annual Meeting and Exhibition 2018*, 2018.

[167] K. Novoselov, A. Geim, S. Morozov, D. Jiang, Y. Zhang, S. Dubonos, I. Grigorieva and A. Firsov, “Electric field effect in atomically thin carbon films,” *Science,* vol. 306, no. 5696, pp. 666-669, 2004.

[168] A. Geim and K. Novoselov, “The rise of graphene,” *Nanoscience and Technology: A Collection of Reviews from Nature Journals,* pp. 11-19, 2010.

[169] T. Poole and G. Nash, “Acoustoelectric current in graphene nanoribbons,” *Sci. Rep. ,* vol. 7, no. 1, p. 1767, 2017.

[170] C. Shi, J. Luxmoore and G. Nash, “Gate tunable graphene-integrated metasurface modulator for mid-infrared beam steering,” *Opt. Express,* vol. 27, no. 10, pp. 14577-14584, 2019.

[171] H. An, B. Tan, J. Moo, S. Liu, M. Pumera and C. Ohl, “Graphene nanobubbles produced by water splitting,” *Nano Lett.,* vol. 17, no. 5, pp. 2833-2838, 2017.

[172] N. Levy, S. Burke, K. Meaker, M. Panlasigui, A. Zettl, F. Guinea, A. Neto and M. Crommie, “Strain-induced pseudo-magnetic fields greater than 300 tesla in graphene nanobubbles,” *Science,* vol. 329, no. 5991, pp. 544-547, 2010.

[173] C. Lim, A. Sorkin, Q. Bao, A. Li, K. Zhang, M. Nesladek and K. Loh, “A hydrothermal anvil made of graphene nanobubbles on diamond,” *Nat. Commun.,* vol. 4, p. 1556, 2013.

[174] L. Zhou, L. Islas, N. Taylor, O. Bikondoa, E. Robles and W. Briscoe, “Graphene surface structure in aqueous media: Evidence for an air-bubble layer and ion adsorption,” *Carbon,* vol. 143, pp. 97-105, 2019.

[175] E. Lukianova-Hleb, Y. Hu, L. Latterini, L. Tarpani, S. Lee, R. Drezek, J. Hafner and D. Lapotko, “Plasmonic nanobubbles as transient vapor nanobubbles generated around plasmonic nanoparticles,” *ACS Nano,* vol. 4, no. 4, pp. 2109-2123, 2010.

[176] N. Rapoport, Z. Gao and A. Kennedy, “Multifunctional nanoparticles for combining ultrasonic tumor imaging and targeted chemotherapy,” *Journal of the National Cancer Institute,* vol. 99, no. 14, pp. 1096-1106, 2007.

[177] L. Anderson, E. Hansen, E. Lukianova-Hleb, J. Hafner and D. Lapotko, “Optically guided controlled release from liposomes with tunable plasmonic nanobubbles,” *J. Controlled Release,* vol. 144, no. 2, pp. 151-158, 2010.

[178] S. Emelianov, “Light, sound, nanobubbles: New approach to constract-enhanced ultrasound and photoacoustic imaging,” *The Journal of the Acoustical Society of America ,* vol. 145, no. 3, p. 1779, 2019.

[179] E. Lukianova-Hleb, X. Ren, R. Sawart, X. Wu, V. Torchilin and D. Lapotko, “On-demand intracellular amplification of chemoradiation with cancer-specific plasmonic nanobubbles,” *Nat. Med. ,* vol. 20, no. 7, pp. 778-784, 2014.

[180] G. Campbell, Bubbles in food, St Paul, Minn., USA: Eagan Press, 1999.

[181] I. Kamei, “Nanobubble-containing composition and use therefor.”. United States patent application Patent 15/193,176, 2 March 2017.

[182] K. Ebina, K. Shi, M. Hirao, J. Hashimoto, Y. Kawato, S. Kaneshiro, T. Morimoto, K. Koizumi and H. Yoshikawa, “Oxygen and air nanobubble water solution promote the growth of plants, fishes and mice,” *PLoS One,* vol. 8, no. 6, p. 65339, 2013.

[183] W. Shi, G. Pan, Q. Chen, L. Song, L. Zhu and X. Ji, “Hypoxia remediation and methane emission manipulation using surface oxygen nanobubbles,” *Environ. Sci. Technol.,* vol. 52, no. 15, pp. 8712-8717, 2018.

[184] Metz M C, “The geology of the Snowbird deposit, Mineral Co. Montana,” *MSc Thesis, Washington State University ,* 1971.

[185] S. Broom-Fendley, A. E. Brady, F. Wall, G. Gunn and W. Dawes, “REE minerals at the Songwe Hill carbonatite, Malawi: HREE enrhciment in late stage apatite.,” *Ore Geol. Rev.,* vol. 81, pp. 23-41, 2017.

[186] A. Neto, F. Guinea, N. Peres, K. Novoselov and A. Geim, “The electronic properties of graphene,” *Rev. Mod. Phys.,* vol. 81, no. 1, p. 109, 2009.

[187] L. Bandhu and G. Nash, “Temperature dependence of the acoustoelectric current in graphene,” *Appl. Phys. Lett.,* vol. 105, no. 26, p. 263106, 2014.

[188] S. Stankovich, D. Dikin, G. Dommett, K. Kohlaas, E. Zimney, E. Stach, R. Piner, S. Nguyen and R. Ruoff, “Graphene-based composite materials,” *Nature,* vol. 442, no. 7100, p. 282, 2006.

[189] A. Obraztsov, “Chemical vapour deposition: making graphene on a large scale,” *Nat. Nanotechnol. ,* vol. 4, no. 4, pp. 212-213, 2009.

[190] P. Nemes-Incze, Z. Osvath, K. Kamaras and L. Biro, “Anomolies in thickness measurements of graphene and a few layer graphite crystals by tapping mode atomic force microscopy,” *Carbon,* vol. 46, no. 11, pp. 1435-1442, 2008.

[191] S. Chatterjee, X-ray diffraction: its theory and applications, PHI Learning Pvt. Ltd., 2010.

[192] B. Lafuente, R. T. Downs, H. Yang and N. Stone, “The power of databases: the RRUFF project, Highlights of mineralogical crystallography,,” *De Gruyter,* pp. 1-29, 2016.

[193] A. Bell, J. Smith, J. Attfield, J. Rawson and W. David, “A synchrotron X-ray powder diffraction study of 4-(2, 3, 4- trifluorophenyl)-1, 2,3,5-dithiadiazolyl. Crystal structure determination using a global optimisation method.,” *New J. Chem.,* vol. 23, no. 6, pp. 565-567, 1999.

[194] K. Harris, M. Tremayne and B. Kariuki, “Contempory advances in the use of powder X-ray diffraction for structure determination,” *Angewandte Chemie International Edition,* vol. 40, no. 9, pp. 1626-1651, 2001.

[195] T. Grammatikopoulos, W. Mercer and C. Gunning, “Mineralogical characterisation using QEMSCAN of the Nechalacho heavy rare earth metal deposit, Northwest Territories, Canada.,” *Can. Metall. Q.,* vol. 52, no. 3, pp. 265-277, 2013.

[196] C. Clayton, “Applications of radioisotope X-ray fluorescence analysis in geological assay, mining and mineral processing,” *Nuclear techniques and mineral resources ,* 1969.

[197] M. Mantler and M. Schreiner, “X-ray fluorescence spectrometry in art and archeology,” *X-Ray Spectrometry: An International Journal,* vol. 29, no. 1, pp. 3-17, 2000.

[198] H. Niu and R. Houk, “Fundamental aspects of ion extracted in inductively coupled plasma mass spectrometry,” *Spectrochim. Acta,* vol. 51, no. 8, pp. 779-815, 1996.

[199] W. Zhang and R. Honaker, “A fundamental study of octanohydroxamic acid adsorption on monazite surfaces.,” *Int. J. Miner. Process.,* vol. 164, pp. 26-36, 2017.

[200] J. Goulle, L. Mahieu, J. Castermant, N. Neveu, L. Bonneau, G. Laine, D. Bouige and C. Lacroix, “Metal and metalloid multi-elementary ICP-MS validation in whole blood, plasma, urine and hair: reference values,” *Forensic Sci. Int.,* vol. 153, no. 1, pp. 39-44, 2005.

[201] W. Zhang, R. Q. Honaker and J. G. Groppo, “Flotation of monazite in the presence of calcite part I: Calcium ion effects on the adsorption of hydroxamic acid.,” *Miner. Eng.,* vol. 100, pp. 40-48, 2017.

[202] E. Espiritu, G. de Silva and K. E. Waters, “IMPC:XXVIII International Mineral Processing Congress Proceedings.,” Quebec, 2016.

[203] Y. Gu, “Automated scanning electron microscope based mineral liberation analysis an introduction to JKMRC/FEI mineral liberation analyser,” *J. Miner. Mater. Charact. Eng.,* vol. 2, no. 1, p. 33, 2003.

[204] G. Rollinson, J. Andersen, R. Stickland, M. Bon and R. Fairhurst, “Characterisation of non-sulphide zinc deposits using QEMSCAN,” *Miner. Eng.,* vol. 24, no. 8, pp. 778-787, 2011.

[205] C. Knappett, D. Pirrie, M. Power, L. Nikolakopoulou, J. Hilditch and G. Rollinson, “Mineralogical analysis and provenancing of ancient ceramics using automated SEM-EDS analysis (QEMSCAN): a pilot study on LB I pottery from Akrotiri, Thera,” *Journal of Archeological Science,* vol. 38, no. 2, pp. 219-232, 2011.

[206] D. Smythe, A. Lombard and L. Coetzee, “Rare Earth Element deportment studies utilising QEMSCAN technology,” *Miner. Eng.,* vol. 52, pp. 52-61, 2013.

[207] I. Kheterpal and R. Mathies, “Capillary Array Electrophoresis DNA Sequencing,” *Anal. Chem.,* vol. 71, no. 1, pp. 31-37, 1999.

[208] D. Rugar and P. Hansma, “Atomic force microscopy,” *Phys. Today,* vol. 43, no. 10, pp. 23-30, 1990.

[209] T. Hassenkam, G. Fantner, J. Cutroni, J. Weaver, D. Morse and P. Hansma, “High-resolution AFM imaging of intact and fractured trabecular bone,” *Bone,* vol. 35, no. 1, pp. 4-10, 2004.

[210] A. Alessandrini and P. Facci, “AFM: a versatile tool in biophysics,” *Meas. Sci. Technol.,* vol. 16, no. 6, p. 65, 2005.

[211] Y. Kuwahara, “Muscovite surface structure imaged by fluid contact mode AFM,” *Phys. Chem. Miner.,* vol. 26, no. 3, pp. 198-205, 1999.

[212] K. Boussu, B. Van der Bruggen, A. Volodin, J. Snauwaert, C. Van Haesendonck and C. Vandecasteele, “Roughness and hydrophobicity studies of nanofiltration membranes using different modes of AFM,” *J. Colloid Interace Sci.,* vol. 286, no. 2, pp. 632-638, 2005.

[213] Y. Maeda, T. Matsumoto and T. Kawai, “Observation of single and double stranded DNA using non-contact atomic force microscopy.,” *Appl. Surf. Sci.,* vol. 140, no. 3-4, pp. 400-405, 1999.

[214] Hansma, J. Cleveland, M. Randmacher, D. Walters, P. Hillner, M. Bezanilla, M. Fritz, D. Vie, H. Hansma, C. Prater and J. Massie, “Tapping mode atomic force microscopy in liquids,” *Appl. Phys. Lett.,* vol. 64, no. 13, pp. 1738-1740, 1994.

[215] B. Johnson and R. Mutharasan, “Biosensing using dynamic mode cantilever sensors: A review,” *Biosensors and bioelectronics,* vol. 32, no. 1, pp. 1-18, 2012.

[216] S. Kitamura and M. Iwatsuki, “High-resolution imaging of contact potential difference with ultrahigh vacuum noncontact atomic force microscopy.,” *Appl. Phys. Lett.,* vol. 72, no. 24, pp. 3154-3156, 1998.

[217] A. Weisenhorn, H. P.K., T. Albrecht and C. Quante, “Forces in atomic force microscopy in air and water,” *Appl. Phys. Lett.,* vol. 54, no. 26, pp. 2651-2653, 1989.

[218] X. Yin and J. Drelich, “Surface charge microscopy: novel technique for mapping charge-mosiac surfaces in electrolyte solutions,” *Langmuir,* vol. 24, no. 15, pp. 8013-8020, 2008.

[219] W. Bowen, T. Doneva and J. Stoton, “The use of atomic force microscopy to quantify membrane surface electrical properties,” *Colloids Surf., A,* vol. 201, no. 1-3, pp. 73-83, 2002.

[220] N. Eom, D. Parsons and V. Craig, “Roughness in surface force measurements: Extension of DVLO theory. To describe the forces between Hafnia surfaces,” *J. Phys. Chem. B,* vol. 121, no. 26, pp. 6442-6453, 2017.

[221] D. Parsons, R. Walsh and V. Craig, “Surface forces: surface roughness in theory and experiment,” *J. Chem. Phys. ,* vol. 140, no. 16, p. 164701, 2014.

[222] R. Considine and C. Drummond, “Surface roughness and surface force measurement: A comparison of electrostatic potentials derived from atomic force microscopy and electrophoretic mobility measurements,” *Langmuir,* vol. 17, no. 25, pp. 7777-7783, 2001.

[223] R. C. Barrett and C. F. Quate, “High-speed, large scale imaging with the atomic force microscope,” *J.Vac. Sci Technol,* vol. 9, no. 2, pp. 302-306, 1991.

[224] T. Ando, “High-speed atomic force microscopy coming of age,” *Nanotechnology ,* vol. 23, no. 6, p. 062001, 2012.

[225] A. Humphris, M. Miles and J. Hobbs, “A mechanical microscope: High speed atomic force microscopy,” *Appl. Phys. Lett.,* vol. 86, no. 3, p. 034106, 2005.

[226] L. M. Picco, P. Dunton, A. Ulcinas, D. J. Engeldew, O. Hoshi, T. Ushiki and M. J. Miles, “High-speed AFM of human chromosomes in liquid,” *Nanotechnology,* vol. 19, no. 38, p. 384018, 2008.

[227] C. Evans, O. Payton, L. Picco and M. Allen, “Algal Viruses: The (Atomic) Shape of Things to Come.,” *Viruses,* vol. 10, no. 9, p. 490, 2018.

[228] N. Kodera, D. Yamamoto, R. Ishikawa and T. Ando, “Video imaging of of walking myosin V by high-speed atomic force microscopy,” *Nature,* vol. 468, no. 7320, p. 72, 2010.

[229] M. Endo, K. Hidaka and H. Sugiyama, “Direct AFM observation of an opening event of a DNA cuboid constructed via a prism structure.,” *Org. Biomol. Chem. ,* vol. 9, pp. 2075-2077, 2011.

[230] K. Miyata, J. Tracey, K. Miyazawa, V. Haapasilta, P. Spijker, Y. Kawagoe, A. Foster, K. Tsukamoto and T. Fukuma, “Dissolution processes at step edges of calcite in water investigated by high-speed frequency modulated atomic force microscopy and simluation,” *Nano Lett.,* vol. 17, no. 7, pp. 4083-4089, 2017.

[231] D. Yamamoto, T. Uchihashi, N. Kodera and T. Ando, “Anisotropic diffusion of point defects in a two-dimensional crystal of streptavidin observed by high-speed atomic force microscopy,” *Nanotechnology,* vol. 19, no. 38, p. 384009, 2008.

[232] O. Payton, L. Picco and T. Scott, “High-speed atomic force microscopy for materials science,” *Int. Mater. Rev.,* vol. 61, no. 8, pp. 473-494, 2016.

[233] S. K. Brushan, “Geology of the Kamthai rare earth deposit,” *J. Geol. Soc. India,* vol. 85, no. 5, pp. 537-546, 2015.

[234] R. D. Tucker, H. E. Belkin, K. J. Schulz, S. G. Peters, F. Horton, K. Buttleman and E. R. Scott, “A major light rare-earth element (LREE) resource in the Khanneshin carbonatite complex, southern Afghanistan.,” *Econ. Geol.,* vol. 107, no. 2, pp. 197-208, 2012.

[235] M. C. Metz, D. G. Brookins, P. E. Rosenberg and R. E. Zartman, “Geology and geochemistry of the Snowbird deposit, Mineral County, Montana,” *Econ. Geol.,* vol. 80, no. 2, pp. 394-409, 1985.

[236] I. M. Samson, S. A. Wood and K. Finucane, “Fluid inclusion characteristics of genesis of the fluorite-parisite mineralization in the Snowbird deposit, Montana,” *Econ. Geol.,* vol. 99, no. 8, pp. 1727-1744, 2004.

[237] E. Gavish and G. Friedman, “Quantitative analysis of calcite and Mg calcite by X-ray diffraction: effect of grinding on peak height and peak area.,” *Sedimentology,* vol. 20, no. 3, pp. 437-44, 1973.

[238] R. Miyawaki, K. Yokoyama and T. Husdal, “Bastnasite- (Nd), a new Nd-dominant member of the bastnasite group from the Stetind pegmatite, Tysfjord, Nordland, Norway,” *Eur. J. Mineral.,* vol. 25, no. 2, pp. 187-191, 2013.

[239] A. Pavese, M. Catti, S. Parker and A. Wall, “Modelling of the thermal dependence of structural and elastic properties of calcite, CaCO3,” *Phys. Chem. Miner. ,* vol. 23, no. 2, pp. 89-93, 1996.

[240] O. Pavez, P. R. G. Bradao and A. E. S. Peres, “Technical note-adsorption of oleate and octyl-hydroxamate on to rare earth minerals,” *Miner. Eng.,* vol. 3, no. 9, pp. 357-366, 1996.

[241] D. Al-Mahrouqi, J. Vinogradov and D. Jackson, “Zeat potential of artificial and natural calcite in aqueous solution,” *Adv. Colloid Interface Sci.,* vol. 240, pp. 60-76, 2016.

[242] M. Voigt, J. D. Rodriguez-Blanco, B. Vallina, L. G. Benning and E. H. Oelkers, “An experimental study of hydroxylbastnasite solubility in aqueous solutions at 25C.,” *Chem. Geol.,* vol. 430, pp. 70-77, 2016.

[243] E. Espiritu, G. de Silva, D. Azizi, F. Larachi and K. Water, “The effect of dissolved species on bastnasite, monazite and dolomite flotation using benzohydroxamate collector,” *Colloids Surf., A,* vol. 539, pp. 319-334, 2018.

[244] R. Croll, S. Swindon, M. Hall, C. Brown, G. Beer, J. Scheepers, T. Redellinghuys, G. Wild and G. Trusler, “Mkango Resources Limited, Songwe Hill REE project, Malawi: NI 43-101 Pre-feasibility Report,” MSA Group Pty Ltd, 2014.

[245] A. Jordens, C. Marion, T. Grammatikopoulos, B. Hart and K. E. Waters, “Beneficiation of the Nechalacho rare earth deposit: Flotation response using behzohydroxamic acid.,” *Miner. Eng.,* vol. 99, pp. 158-169, 2016.

[246] B. Yu and M. Aghamirian, “REO mineral separation from silicates and carbonate gangue minerals,” *C. Metall. Q.,* vol. 54, no. 4, pp. 337-387, 2015.

[247] I. Hornig-Kjarsgaard, “Rare earth elements in sovitic carbonatites and their mineral phases,” *J. Petrol.,* vol. 39, pp. 2105-2121, 1998.

[248] G. Melcher, “The carbonatites of Jacupiranga, Sao Paulo, Brazil.,” *Carbonatites ,* vol. 169, no. 181, pp. 1361-1382, 1966.

[249] R. Santos and R. Clayton, “The carbonate content in high-temperature apatite: An analytical method applied to apatite from the Jacupiranga alkaline complex.,” *Am. Mineral.,* vol. 80, no. 3-4, pp. 336-344, 1995.

[250] A. Costanzo, K. Moore, F. Wall and M. Feely, “Fluid inclusions in apatite from Jacupiranga calcite carbonatites: evidence for a fluid-stratified carbonatite magma chamber,” *Lithos,* vol. 91, no. 1-4, pp. 208-228, 2006.

[251] L. Menezes-Filho, D. Atencio, M. Andrade, R. Downs, M. Chaves, A. Romano, S. R. and A. Persiano, “Pauloabibite, trigonal NaBbO3, isostructural with ilmenite, from the Jacupiranga carbonatite, Cajati, Sao Paulo, Brazil,” *Am. Mineral.,* vol. 100, no. 2-3, pp. 442-446, 2015.

[252] X. Chen, X. Jin, J. Tan, W. Li, M. Chen, L. Yao and H. Yang, “Large-scale synthesis of water-soluble luminescent hydroxyapatite nanorods for security printing,” *J. Colloid Interface Sci.,* vol. 468, pp. 300-306, 2016.

[253] E. Skwarek and W. Janusz, “The influence of carbonatite ions on the structure of the electrical double layer at the interface of hydroxyapatite/electrolyte solution,” *Materials Science,* vol. 22, no. 2, pp. 174-178, 2016.

[254] A. Fahami and G. Beall, “Mechanosynthesis of carbonate doped chlorapatite-ZnO nanocomposite with negative zeta potential,” *Ceram. Int.,* vol. 41, no. 9, pp. 12323-12330, 2015.

[255] C. Botelho, M. Lopes, I. Gibson, S. Best and J. Santos, “Structural analysis of Si-substituted hydroxyapatite: zeta potentials and X-ray photoelectron spectroscopy,” *J. Mater. Sci.,* vol. 13, no. 12, pp. 1123-1127, 2002.

[256] I. Filippova, L. Filippov, Z. Lafhaj, O. Barres and D. Fornasiero, “Effect of calcium minerals reactivity on fatty acids adsorption and flotation,” *Colloids Surf., A,* vol. 545, pp. 156-166, 2018.

[257] A. Walter, D. Nahon, R. Flicoteaux, J. Girand and A. Melfi, “Behaviour of major and trace elements and fractionation of REE under tropical weathering of a typical apatite-rich carbonatite from Brazil,” *Earth Planet. Sci. Lett.,* vol. 136, no. 3-4, pp. 591-602, 1995.

[258] K. Pandur, K. Ansdell, D. Kontak, K. Halpin and S. Creighton, “Petrographic and mineral chemical characteristics of the Hoidas Lake deposit, northern Saskatchewan, Canada: constraints on the origin of a distal magmatic- hydrothermal REE system.,” *Econ. Geol.,* vol. 111, no. 3, pp. 667-694, 2016.

[259] E. Espiritu and K. Waters, “Flotation studies of monazite and dolomite,” *Miner. Eng.,* vol. 116, pp. 101-106, 2018.

[260] A. Andersen, J. Clark, P. Larson and J. Donovan, “REE fractionation, mineral speciation, and supergene enrichement of the Bear Lodge carbonatites, Wyoming, USA.,” *Ore Geol. Rev.,* vol. 89, pp. 780-807, 2017.

[261] S. Broom-Fendley, A. Brady, M. Horstwood, A. Woolley, J. Mtegha, F. Wall, W. Dawes and G. Gunn, “Geology, geochemistry and

geochronology of the Songwe Hill carbonatite, Malawi," *J. Afr. Earth Sci.,,* vol. 134, pp. 10-23, 2017.

[262] K. Buchmann, M. Frenzel, J. Krause and J. Gutzmer, "Advanced identification and quantification of In-bearing minerals by scanning electron microscope-based image analysis," *Microsc. Microanal.,* vol. 23, no. 3, pp. 527-537, 2017.

[263] X. Wang, B. Zhao, J. Hu, S. Wang, R. Tai, X. Gao and L. Zhang, "Interfacial gas nanobubbles or oil nanodroplets?," *Phys. Chem. Chem. Phys.,* vol. 19, no. 2, pp. 1108-1114, 2017.

[264] K. Rangharajan, K. Kwak, A. Conlisk, Y. Wu and S. Prakash, "Effects of surface modification on interfacial nanobubble morphology and contact line tension," *Soft Matter,* vol. 11, no. 26, pp. 5214-5223, 2015.

[265] R. Platt, S. Chen, Y. Zhou, M. Yim, L. Swiech, H. Kempton, J. Dahlman, O. Parnas, T. Eisenhaure, M. Jovanovic and D. Graham, "CRISPR-Cas0 knockin mice for genome editing and cancer modeling," *Cell,* vol. 159, no. 2, pp. 440-455, 2014.

[266] C. Schneider, W. Rasband and K. Eliceiri, "NIH Image to ImageJ: 25 years of image analysis," *Nat. Methods ,* vol. 9, no. 7, pp. 671-675, 2012.

[267] D. Li, D. Jing, Y. Pan, W. Wang and X. Zhao, "Coalescence and stability analysis of surface nanobubbles on the polystyrene/water interface," *Langmuir,* vol. 30, no. 21, pp. 6079-6088, 2014.

[268] H. Teshima, K. Takahashi, Y. Takata and T. Nishiyama, "Wettability of AFM tip influences the profile of interfacial nanobubbles," *J. Appl. Phys. ,* vol. 123, no. 5, p. 054303, 2018.

[269] W. Walczyk and H. Schonherr, "Dimensions and the Profile of Surface Nanobubbles: Tip- Nanobubble Interactions and Nanobubble Deformation in Atomic Force Microscopy," *Langmuir,* vol. 30, no. 40, pp. 11955-119656, 2014.

[270] W. Ducker, "Contact angle and stability of interfacial nanobubbles," *Langmuir ,* vol. 25, no. 16, pp. 8907-8910, 2009.

[271] X. Zhang, M. Uddin, H. Yang, G. Toikka, W. Ducker and N. Maeda, "Effects of surfactants on the formation and the stability of interfacial nanobubbles," *Langmuir,* vol. 28, no. 28, pp. 10471-10477, 2012.

[272] Q. Xiao, Y. Liu, Z. Guo, Z. Liu and X. Zhang, "How nanobubbles lose stability: Effects of surfactants," *Appl. Phys. Lett. ,* vol. 111, no. 13, p. 131601, 2017.

[273] Andersen T, "Compositional variation of some rare earth minerals from the Fen complex (Telemark, SE Norway): implications for the mobility of rare earths in a carbonatite system.," *Minerals Magazine ,* vol. 50, pp. 503-509, 1986.

[274] L. Bocquet and P. Tabeling, "Physics and technology aspects of nanofluidics," *Lab Chip,* vol. 14, no. 17, pp. 3143-3158, 2014.

[275] A. Landels, T. Beacham, C. Evans, G. Carnovale, S. Raikova, I. Cole, P. Goddard, C. Chuck and M. Allen, "Improving electrocoagulation floatation for harvesting micoalgae," *Algal Res.,* vol. 39, p. 101446, 2019.

[276] D. Necas and P. Klapetak, "Gwyddion: an open-source software for SPM data analysis," *Open Phys.,* vol. 10, no. 1, pp. 181-188, 2012.

[277] L. Gomez de Arco, Y. Zhang, C. Schlenker, K. Ryu, M. Thompson and C. Zhou, “Continuous, highly flexible, and transparent graphene films by chemical vapor deposition for organic photovoltaics,” *ACS Nano,* vol. 4, no. 5, pp. 2865-2873, 2010.

[278] O. Fursenko, M. Lukosius, G. Lupina, J. Bauer, C. Villringer and A. Mai, “Development of graphene process control by industrial optical spectroscopy setup,” *Modeling Aspects in Optical Metrology VI International Society for Optics and Photonics,* 2017.

[279] L. Zhou, L. Fox, M. Włodek, L. Islas, A. Slastanova, E. Robles, O. Bikondoa, R. Harniman, N. Fox, M. Cattelan and W. Briscoe, “Surface structure of few layer graphene,” *Carbon,* vol. 136, pp. 255-261, 2018.

[280] S. Wang, Y. Zhang, N. Abida and L. Cabrales, “Wettability and surface free energy of graphene films,” *Langmuir,* vol. 25, no. 18, pp. 11078-11081, 2009.

[281] C. Shih, M. Strano and D. Blankschtein, “Wetting translucency of graphene,” *Nat. Mater.,* vol. 12, no. 10, p. 866, 2013.

[282] C. Shih, Q. Wang, S. Lin, K. Park, Z. Jin, M. Strano and D. Blankschtein, “Erratum: Breakdown in the Wetting Transparency of Graphene,” *Phys. Rev. Lett. ,* vol. 115, no. 4, p. 049901, 2015.

[283] F. Taherion, V. Marcon, N. van der Vegt and F. Leroy, “What is the contact angle of water on graphene?,” *Langmuir,* vol. 29, no. 5, pp. 1457-1465, 2013.

[284] G. Hong, Y. Han, T. Schutzius, Y. Wang, Y. Pan, M. Hu, J. Jie, C. Sharma, U. Muller and D. Poulikakos, “On the mechanism of hydrophilicity of graphene,” *Nano Lett.,* vol. 16, pp. 4447-4453, 2016.

[285] S. Yang, S. Dammer, N. Bremond, H. Zandvliet, E. Kooij and D. Lohse, “Characterization of nanobubbles on hydrophobic surfaces in water,” *Langmuir,* vol. 23, no. 13, pp. 7072-7077, 2007.

[286] N. Ishida, K. Matsuo, K. Imamura and V. Craig, “Hydrophobic attraction measured between asymmetric hydrophobic surfaces,” *Langmuir,* vol. 34, no. 12, pp. 3588-3596, 2018.

[287] M. Alheshibri and V. Craig, “Differentiating between Nanoparticles and Nanobubbles by Evaluation of the Compressibility and Density of Nanoparticles,” *J. Phys. Chem.,* vol. 122, no. 38, pp. 21998-22007, 2018.

[288] X. Zhang, J. Ren, H. Yang, Y. He, J. Tan and G. Qiano, “From transient nanodroplets to permanent nanolenses,” *Soft Matter,* vol. 8, pp. 4314-4317, 2012.

[289] A. Geneyton, L. Filippov and N. Menad, “Effects of atom substitutions and dissolved carbonate species on monazite electrophoretic mobility,” *Colloids Surf., A,* vol. 570, pp. 141-146, 2019.

[290] X. Zhang, H. Du, X. Wang and J. Miller, “Surface chemistry considerations in the flotation of rare-earth and other semisoluble salt minerals.,” *Miner. Metall. Process,* vol. 30, no. 1, pp. 24-37, 2013.

[291] J. Cui, G. Hope and A. Buckley, “Spectroscopic investigation of the interaction of hydroxamate with bastnaesite (cerium) and rare earth oxides,” *Miner. Eng.,* vol. 36, pp. 91-99, 2012.

[292] G. Abaka-Wood, J. Addai-Mensah and W. Skinner, “Review of flotation and physical separation of rare earth element minerals,” *4th UMaT Biennial International Mining and Mineral Conference,* pp. 55-62, 2016.

[293] J. Hendrick, S. Sinha and V. Kosynkin, “Loparite, a rare earth ore (Ce, Na, Sr, Ca)(Ti, Nb, Ta, Fe+3) O3,” *J. Alloys Compd.,* vol. 250, no. 1-2, pp. 467-470, 1997.

[294] G. Krysenko, D. Epov, M. Medkov, P. Sitnik and V. Avramenko, “Extraction of Rare-Earth Elements in Hydrofluoride Decomposition of Loparite Concentrate,” *J. Appl. Chem.,* vol. 91, no. 10, pp. 1665-1670, 2018.

[295] M. Khokhulya, A. Fomin, T. Mukhina and T. Kontorina, “Development of complex magneto-gravity separation technology of rare metal minerals using computer modelling,” *International Multidisciplinary Scientific GeoConference: SGEM: Surveying Geology & Mining Ecology Management,* vol. 2, pp. 1057-1064, 2016.

[296] R. Mitchell, P. Burns and A. Chakmouradian, “The crystal structures of loparite-(Ce),” *Can. Mineral.,* vol. 38, no. 1, pp. 145-152, 2000.

[297] D. Feng, R. Shivaramaiah and A. Navrotsky, “Rare-earth perovskites along the CaTiO3-Na0.5La0.5TiO3 join: Phase transitions, formation enthalpies, and implications for loparite minerals,” *Am. Mineral.,* vol. 101, no. 9, pp. 2051-2056, 2016.

[298] R. Platt, “Perovskite, loparite and Ba-Fe hollandite from the Schryburt Lake carbonatite complex, northwestern Ontario, Canada,” *Min. Mag. ,* vol. 58, no. 390, pp. 49-57, 1994.

[299] R. Mitchell and R. Liferovich, “Subsolidus deuteric/hydrothermal alteration of eudialyte in lujavrite from the Pilansberg alkaline complex, South Africa,” *Lithos,* vol. 91, no. 1-4, pp. 352-372, 2006.

[300] B. Wu, R. Wang, J. Yang, F. Wu, W. Zhang, X. Gu and A. Zhang, “Zr and REE mineralization in sodic lujavrite from the Saima alkaline complex, northeastern China. A mineralogical study and comparison with potassic rocks,” *Lithos,* vol. 262, pp. 232-246, 2016.

[301] X. Niu, R. Ruan, L. Xia, L. Li, H. Sun, Y. Jia and Q. Tan, “Correlation of surface adsorption and oxidation with a floatability difference in galena and pyrite in high-alkaline lime systems,” *Langmuir,* vol. 34, no. 8, pp. 2716-2724, 2018.

[302] T. Prior, D. Giurco, G. Mudd, L. Mason and J. Behrisch, “Resource depletion, peak minerals and the implications for sustainable resource management,” *Global Environmental Change,* vol. 22, no. 3, pp. 577-587, 2012.

[303] X. Zhang, Z. Lu, H. Tan, L. Bao, Y. He, C. Sun and D. Lohse, “Formation of surface nanodroplets under controlled flow conditions,” *Proc. Natl. Acad. Sci. U.S.A,* vol. 112, no. 30, pp. 9553-9257, 2015.

[304] L. Luo and H. White, “Electrogeneration of single nanobubbles as sub-50-nm-radius platinum nanodisk electrodes,” *Langmuir,* vol. 29, no. 35, pp. 11169-11175, 2013.

[305] S. German, M. Edwards, Q. Chen, Y. Liu, L. Luo and H. White, “Electrochemistry of single nanobubbles. Estimating the critical size of bubble-forming nuclei for gas-evolving electrode reactions,” *Faraday Discuss.,* vol. 193, pp. 223-240, 2016.

[306] K. Chu, Y. Soo Joung, R. Enright, C. Buie and E. Wang, “Hierarchically structured surfaces for boiling critical heat flux enhancement,” *Appl. Phys. Lett.,* vol. 102, no. 15, p. 151602, 2013.

[307] F. Li, S. Gonzalez-Avila, D. Nguyen and C. Ohl, “Oscillate boiling from microheaters,” *Physical Review Fluids,* vol. 2, no. 1, p. 014007, 2017.

[308] D. Nguyen, L. Hu, J. Miao and C. Ohl, “Oscillate boiling from electrical microheaters,” *Phys. Rev. Appl.,* vol. 10, no. 4, p. 044064, 2018.

[309] K. M. Kanazawa Y, “Rare earth minerals and resources in the world.,” *J. Alloys Comp.,* Vols. 408-412, pp. 1339-1343, 2006.

[310] U. Kolitsch, H. W. Graf and G. Blac, “Untersuchungen uber die Seltenerden-Carbonate Bastnas and Synchisit von der Grube Clara im Schwarzwald: Nachweis von Bastnasit-(Ce), Bastnasit-(Nd), Bastnasit-(La), und Synchisit-(Ce).,” *Aufschluss,* vol. 48, pp. 367-379, 1997.

[311] X. Y. Yang, W. D. Sun, Y. X. Zhang and Y. F. Zheng, “Geochemical constraints on the genesis of the Bayan Obob Fe-Nb-REE deposit in Inner Mongolia, China,” *Geochim. Cosmochim. Acta,* vol. 73, pp. 1417-1435, 2009.

[312] S. Kalatha, M. Perraki, M. Economou-Eliopoulos and I. Mitsis, “On the origin of Bastnaesite-(La, Nd, Y) in the Nissi (Patitira) Bauxite Laterite Deposit, Lokris, Greece,,” *Minerals,* vol. 7, no. 3, p. 45, 2017.

[313] Z. LeMin, H. Zeng Qian, Z. Yuan Chuan and L. Wei, “Study on accessory minerals in Yaja granite, northern Tibet: indicator of the magma source.,” *Acta. Petrol. Sin.,* vol. 27, no. 9, pp. 2786-2794, 2011.

[314] M. Fleischer, “New Mineral Names,” *Am. Mineral.,* vol. 50, p. 1505, 1965.

[315] H. Yang, R. F. Dembowski, P. G. Conrad and R. T. Downs, “Crystal structure and Raman spectrum of hydroxyl-bastnasite (Ce), CeCO3.(OH).,” *Am. Mineral.,* vol. 93, no. 4, pp. 698-701, 2008.

[316] Z. Maksimovi and G. Pant, “Hydroxyl-bastnaesite-(Nd), a new mineral from Montenegro, Yugoslavia.,” *Mineral. Mag.,* vol. 49, no. 354, pp. 717-720, 1985.

[317] Y. Ni, J. Post and J. Hughes, “The crystal structure of parisite-(Ce), Ce2CeF2(CO3)3,” *Am. Mineral.,* vol. 49, pp. 251-258, 2000.

[318] L. A. D. Menezes- Filho, M. L. S. Cheves, N. V. Chukanov, D. Atencio, R. Scholz, I. Pekov, G. Magela da Costa, S. M. Morrison, M. Andrade, E. Freitas, R. T. Downs and D. I. Belakovskiy, “Parisite- (La),” *Mineral. Mag.,* vol. 80, pp. 915-922, 2016.

[319] J. Jambor, E. Burke, T. Ercit and J. Grice, “New mineral names,” *Am. Mineral.,* vol. 73, p. 1499, 1988.

[320] P. Zhang and K. Tao, “Bayan Obo mineralogy,” *Beijing, China: Science Publisher,* vol. 2008, p. (In Chinese with English Summary), 1986.

[321] A. Zaitsev, “Rhombohedral carbonatites from carbonatites of the Khibina massif, Kola Penninsula, Russia.,” *Can. Mineral.,* vol. 34, no. 2, pp. 453-468, 1996.

[322] H. J. Forster, “Synchysite-(Y)- synchysite-(Ce) solid solutions from Markesbach Erzgebirge, Germany: REE and Th mobility during high T alteration of highly fractionated aluminous A-type granites,,” *Mineral. Petrol.,* vol. 72, pp. 259-280, 2001.

[323] Z. Maksimovic and G. Panto, “Minerals of the rare-earth elements in karstic bauxites: synchisite-(Nd), a new mineral from the Grebnik deposit.,” Athens, 1978.

[324] J. B. Dawson and R. W. Hinton, “Trace-element content and partitioning in calcite, dolomite and apatite in carbonatite, Phalaborwa, South Africa,” *Mineral Magazine,* vol. 67, no. 55, pp. 921-930, 2003.

[325] U. Kempe and J. Gotze, “Cathodoluminescence (CL) behaviour and crystal chemistry of apatite from rare- metal deposits.,” *Mineral Magazine,* vol. 66, pp. 151-172, 2002.

[326] R. Ismail, C. L. Ciobanu, N. J. Cook, G. S. Teale, D. Giles, A. S. Mumm and B. Wade, “Rare earths and other trace elements in minerals from skarn assembleges, Hillside iron oxide-copper-gold deposit, Yorke Peninsula, South Australia,” *Lithos,* vol. 184, pp. 456-477, 2014.

[327] K. M. Halpin, The characteristics and origin of the Hoidas Lake REE deposit, MSc Dissertation : University of Saskatchewan, Canada, 2010.

[328] Y. Kon, K. Hoshino, K. Sanematsu, S. Morita, M. Tsunematsu, N. Okamoto, N. Yano, M. Tanaka and T. Takagi, “Geochemical Characteristics of Apatite in Heavy REE-rich Deep-Sea Mud from Minami-Torishima Area, Southeastern Japan,” *Resour. Geol.,* vol. 64, no. 1, p. 47, 2014.

[329] X. Zhang, Surface Chemistry aspects of fluorite and bastnaesite flotation systems, Univeristy of Utah, United States: PhD Thesis, 2014.

[330] J. A. Kim, G. Dodbiba, T. Fujita and N. Fujii, “Characteristics Analysis of a Bastnaesite Rare Earth Mineral for recovery of Cerium.,” *IMPC XXV International Mineral Processing Congress, Brisbane, Australia,* pp. 2927-2932.

[331] J. Luo and X. Chen, “Research into the recovery of high-grade rare-earth concentrate from Baotou complex iron ore, China,” *Miner. Process. Ext. Metall.,* pp. 663-673, 1984.

[332] C. Li, “Solubility and electrokinetic behaviour of synthetic bastnaesite.,” *Masters Thesis, University of California, Berkeley, USA,* 1982.

[333] Pradip, “The surface properties and flotation of rare-earth minerals,” *PhD Thesis, University of California, Berkeley, USA,* 1981.